CORRELATED ACTIVITY AND CORTICOTHALAMIC CELL FUNCTION IN THE EARLY

MOUSE VISUAL SYSTEM

Daniel J Denman

A DISSERTATION

in

Neuroscience

Presented to the Faculties of the University of Pennsylvania

in

Partial Fulfillment of the Requirements for the

Degree of Doctor of Philosophy

2014

Supervisor of Dissertation

_____

Diego Contreras, MD, PhD

Professor of Neuroscience

Graduate Group Chairperson

_____

Joshua I. Gold, PhD, Associate Professor of Neuroscience

Dissertation Committee:

Farran Briggs, Assistant Professor of Physiology, Dartmouth College

Javier Medina, Assistant Professor of Psychology, University of Pennsylvania

Nicole Rust, Assistant Professor of Psychology, University of Pennsylvania

Larry Palmer, Professor of Neuroscience, University of Pennsylvania

ABSTRACT

CORRELATED ACTIVITY AND CORTICOTHALAMIC CELL FUNCTION IN THE EARLY

MOUSE VISUAL SYSTEM

Daniel Denman

Diego Contreras

Vision has long been the model for understanding cortical function. Great progress has been made in understanding the transformations that occur within some primary visual cortex (V1) layers, like the emergence of orientation selectivity in layer 4. Less is known about other V1 circuit elements, like the shaping of V1 input via corticothalamic projections, or the population structure of the cortico-cortical output in layer 2/3. Here, we use the mouse early visual system to investigate the structure and function of circuit elements in V1. We use two approaches: comparative physiology and optogenetics. We measured the structure of pairwise correlations in the output layer 2/3 using extracellular recordings. We find that despite a lack of organization in mouse V1 seen in other species, the specificity of connections preserves a correlation structure on multiple timescales. To investigate the role of corticogeniculate projections, we utilize a transgenic mouse line to specifically and reversibly manipulate these projections with millisecond precision. We find that activity of these cells results a mix of inhibition and excitation in the thalamus, is not spatiotemporally specific, and can affect correlated activity. Finally, we classify mouse thalamic cells according to stimuli used for cell classification in primates and cats, finding some, but not complete, homology to the processing streams of primate thalamus and further highlighting fundamentals of mammalian visual system organization.

TABLE OF CONTENTS

LIST OF ILLUSTRATIONS

CHAPTER 1: INTRODUCTION

In the following work, we utilize the emerging model system of mouse vision to address several questions relating to output neurons from primary visual cortex (V1): layer 2/3 cortico-cortical neurons and corticogeniculate layer 6 cells. First, we address the independence of individual unit responses in layer 2/3 and the relationship to the underlying structure by measuring pairwise correlation on multiple time scales. We assess the functional role of a cell class in layer 6, the corticogeniculate population, and what effect these cells might have on the thalamus and V1 during visual responses. Below, we explain our motivation for exploring these questions, and why we chose to do so using the mouse early visual system.

Cortical structure and function

The cerebral cortex is widely held as the seat of cognition, from simple sensory (Hubel and Wiesel, 1968) and motor (Chouinard, 2006) processing, to complex decision-making (Heekeren et al., 2008) and executive activity (Kimberg and Farah, 1993; Brown and Bowman, 2002; Alvarez and Emory, 2006). Interest in the structure and function of the cerebral cortex dates to the birth of modern neuroscience (Ramon y Cajal, 1890; Penfield and Jasper, 1954). Recognition of the cortex as cognitive center predates this, at least to Thomas Willis in 1664, possibly to Erisistratus c.a. 260 BCE (Gross, 1999)

The painstaking work of early anatomists led to the description of a regular, repeatable organization across broad cortical areas, a layered structure with six, or eight (Ramon y Cajal, 1890), described layers. Contemporary consensus is a cortex with six primary layers (Mountcastle, 1997; Thomson and Lamy, 2007), with the first layer, layer 1, containing mostly dendrites and axons from long-range inputs, and very few cell bodies. The primary thalamic input comes in layer 4, which in turn projects superficially to layers 2 and 3. These superficial layers send cortico-cortical outputs to other cortical areas, as well as locally to layer 5, where many subcortical projection neurons are present. Layer 6 contains a mix of cells, with local cortico-

cortical neurons as well as subcortical projection neurons (Briggs, 2010; Thomson, 2010), with

subcortical targets different than those of layer 5. These layer 6 neurons are of particular interest

in this thesis, and are discussed in more detail below.

Although the structure varies slightly across cortical areas (Herculano-Houzel et al.,

2008; 2013), it is remarkably similar across humans, other primates, and all mammals. A

canonical operation across many cortical areas has been the target of speculation (Mountcastle,

1997; Douglas and Martin, 2007), though this has not yet been thoroughly demonstrated.

Primary visual cortex

Primary visual cortex (V1) is one of the most extensively investigated cortical areas

(Hubel and Wiesel, 1959; 1962; Priebe and Ferster, 2012), serving as a model system for

understanding cerebral cortex. This area, alternatively called granular cortex or Brodmann area

17, has an appearance distinct from many other parts of cortex due to the high density and small

size of the cell bodies in thalamorecipient layer 4. V1 receives a strong thalamic projection from

the dorsal lateral geniculate nucleus (dLGN) to this granular layer 4, and also to some cells within

layer 6. The extensive study of V1 has led to remarkable insight into the transformation of visual

activity within V1. The best and most cited example occurs within layer 4, at the synapse between

arriving thalamic input and L4 stellate cells: the appearance of orientation selective responses. In

the LGN, the best stimulus effectively engages its receptive field center, which is either ON- or

OFF-. The majority of dLGN cells respond equally to elongated stimuli of any orientation.

However, V1 cells that receive direct input from these center-surround cells (either dLGN center-

surround in cat, or layer 4Cβ center surround in some primates) are exquisitely tuned to the

orientation of elongated stimuli. This emergence of orientation selectivity is a consequence of

elongated receptive fields; these elongated receptive fields result from convergence of center-

surround receptive fields offset in space but aligned along the axis of elongation (Reid and

Alonso, 1995). This transformation of orientation insensitive center-surround into orientation

selective responses across one synapse through selective convergence results in so-called

'simple cells'. Simple cells have separable, elongated receptive field subregions that match their orientation selectivity. A second selective convergence from layer 4 to layer 2/3, of cells with matching orientation preference but non-matching phase, may generate the phase-invariant orientation tuning in layer 2/3 (Alonso and Martinez, 1998). These phase-invariant cells are still orientation selective, but do display separable subregions and are called 'complex' cells.

This difference in phase sensitivity between layers 4 and 2/3 is also an example of the structure, or organization, of single cell response properties in primary visual cortex. In this case, the response property of phase sensitivity is organized across layers, with a systematic change from phase sensitive simple cells in layer 4 to the complex cells of layer 2/3, with layer 5 resembling the phase insensitivity in 2/3 and layer 6 a mix of simple and complex cells (Martinez et al., 2005; Hirsch and Martinez, 2006). Here the response properties change systematically through the depth. In most species, response properties are also organized across the dimension orthogonal to the depth: visual space, orientation preference, and ocular dominance all vary systematically across the cortical surface. Exceptions to this organization exist, like the lack of organization in orientation preference in mouse V1, a feature we explore in Chapter 2.

This emergence and organization of phase-invariant orientation selectivity is an example of the great detail at which some V1 processing is understood. Yet much remains to be learned about the function and structure of V1 (Olshausen and Field, 2006). Locally in V1, the role of interneurons in shaping the cortical transformation has drawn great recent interest (Sohya et al., 2007; Cardin et al., 2009; Zariwala et al., 2010; Kerlin et al., 2010; Adesnik et al., 2012; Atallah et al., 2012; Cardin, 2012). Transformations, if any, across other cortical layers have not been well described, and may require often-neglected stimulus parameters like color (Horwitz et al., 2007; Horwitz and Hass, 2012) or behavioral context (Cohen and Maunsell, 2009; Niell and Stryker, 2010; Polack et al., 2013). Most relevantly, we lack a full understanding of the various V1 outputs and what effects these outputs might have on their targets. In addition, network and circuit-level questions like the correlated activity within V1 are an active area of research, including but not limited to, chapter 2 of this thesis.

Correlated activity, pairs, and populations

For much of modern neuroscience, recording techniques have limited the experimenter to either recording from one isolated cell (like with single high impedance electrodes or intracellular recording with glass pipettes), or to the aggregate activity of an unknown, often uncontrollable number of cells (like with field potentials or fMRI). Both of these approaches have been fruitful, and promise to continue to be, especially as they are advanced (Long et al., 2011) and become better understood (Buzsáki et al., 2012; Einevoll et al., 2013). In this work, we have taken advantage of multi-tetrode recording to record the simultaneous activity of small populations of isolated single units, and analyze the correlation between these units at various timescales using various established techniques (Perkel et al., 1967a; Zohary et al., 1994), focusing on pairwise correlations. Correlations can and do occur beyond pairs of neurons (Schnitzer and Meister, 2003; Shlens et al., 2006); the frequency of these types of correlations in the early visual system is not yet clear, nor are any functional consequences.

What can be gained from considering pairwise correlated activity? The interpretation of pairwise correlations depends heavily on the stimulus conditions and the timescale of correlation measured. In the case of stimulus-corrected pairwise cross-correlograms (CCGs) on the scale of milliseconds (Perkel et al., 1967b; Gerstein et al., 1985), correlations can reflect the functional connectivity within the network (Aertsen and Gerstein, 1985; Ostojic et al., 2009). When both cells in a pair of neurons receive common excitatory input, these cells display a sharp CCG peak that straddles the zero line. Monosynaptic excitatory connections generate their own signature, a sharp peak offset from zero by approximately the synaptic latency (~2 milliseconds). Inferring functional connectivity from this form of correlation is useful for comparing said functional connectivity to other physiological measurements, usually other single cell physiological measurements.

Short time scale correlations could be more than an experimental tool for inferring connectivity: coincident spikes on this timescale can drive nonlinearities in the responses in

4

readout neurons. In some cases, this type of correlated activity might carry additional stimulus information (Bohte, 2004), including the visual system (Dan et al., 1998; Shlens et al., 2006). While synchronous activity could be used to encode information, it is not clear if this approach is actually used in any neural system, a possibility explored in more detail in the Discussion.

Pairs of neurons can be correlated on other timescales, like correlated fluctuations in spike count over the period of a stimulus presentation, often seconds long. When these correlated fluctuations are a result of changing stimulus parameters they are called 'signal correlations'. When these fluctuations are independent of stimulus parameters, they are termed 'noise correlations'. Under some decoding regimes, noise correlations can reduce the effectiveness of pooling (Zohary et al., 1994) and reduce the amount of stimulus information in the response (Abbott and Dayan, 1999; Nirenberg and Latham, 2003). The most commonly assumed neural readout regimes, like pooling models (Tolhurst et al., 1983) and variants of this (e.g., Law and Gold, 2009), are sensitive to this form of correlation. Because of the prevalence of these models, noise correlations have been the most extensively considered and measured form of pairwise correlation (Tolhurst et al., 1983; Kruger and Aiple, 1988; Kohn and Smith, 2005; Smith and Kohn, 2008; Cohen and Kohn, 2011).

The effect of correlations of any timescale on decoding of neural information depends on the identity and connectivity of correlated cells (Panzeri et al., 2003). It is therefore important to measure the structure of correlations on all timescales, and understand the mechanisms that generate them. In primate V1, the structure of correlations, both fast synchrony and noise correlations, follows the organization of somatic organization preference. On the short time scale, pairs of cells with similar orientation preferences are more likely to receive common input. This true also on the longer timescale: nearby pairs of cells, and pairs of cells with similar orientation preference, have higher noise correlation (Smith and Kohn, 2008). It is not clear if this organization of correlations is a trivial result of the single cell orientation topography (i.e, organization into orientation pinwheels), or if organization of pairwise correlations might be a reason for pinwheels to exist. To resolve this, we measure the structure of correlation in the

5

absence of this orientation pinwheel organization in mouse visual cortex. We discuss the structure of mouse visual cortex below, and the results of our measurement of correlation in mouse V1 are presented in Chapter 2.

Mouse as a tool for visual cortical neuroscience

The mouse, while not a traditional model system used to study vision, is a useful system for investigating these questions for several reasons. First and foremost, the gross organization of the cortex resembles that of humans, as noted by Ramon y Cajal (in Pasik and Pasik, 2002). But the primary reason is the ready availability of transgenic tools that allow access to specific cell types. Several groups have embarked on large-scale generation of transgenic mouse lines, like the GENSAT project's collection of GFP- or Cre recombinase-expressing lines (Gong et al., 2003; 2007) and the Allen Institute for Brain Science's Cre-dependent tool mouse lines (Madisen et al., 2012). GFP-expressing lines offer the ability to visualize specific populations of cells for targeted recordings, for example PV+ interneurons (Sohya et al., 2007). Cre recombinase lines restrict the expression of this enzyme to a subset of cells. When combined with Cre-dependent transgene expression, either through viral introduction (Atasoy et al., 2008; Cardin et al., 2010b) or crossing with another transgenic line (Madisen et al., 2009; 2012), genetically encoded tools like algal and bacterial opsins (Bernstein and Boyden, 2011; Fenno et al., 2011), $Ca2+$ indicators (Zhao et al., 2011), or voltage indicators (Jin et al., 2012) are only expressed in that subset of Cre-expressign cells. This type of cell type specificity *in vivo* is not yet possible in other model systems.

The size and structure of the mouse brain also provides the opportunity for more complete sampling, relative to other model systems. Mice are lissencephalic, with a smooth cortical surface that lacks gyri or sulci. Because of this flat cortex, all cortical areas are accessible from a cranial window and vertical penetrations are possible in all areas. With the layered structure of cortex parallel to the skull, it is often possible to ensure an even, layer-specific imaging plane. Successive imaging planes can sample across the depth to nearly 800 μm, which because of the small size of mouse cortex allows for imaging to cortical layer 5, and even deeper

imaging can be obtained with microprisms (Chia and Levene, 2009). The small size is also an advantage in the rostral-caudal and medial-lateral planes. Because the total cortical volume is small (~1.8 cm^2, (Badea et al., 2007)), and the 25% of the cortex related to visual processing is even more manageable (~3mm by 3mm), simultaneous imaging and recording across visual areas is feasible (Glickfeld et al., 2013). The ganglion cell population of the mouse retina is better understood than any other species (Masland, 2012; Siegert et al., 2012), opening the possibility of understanding the inputs to central visual areas, and how those inputs might be transformed. Finally, mammalian high-throughput behavior is only possible with rodents (Meier et al., 2011; Scott et al., 2013), and our ability to exploit behavioral repertoire of mice is growing (Carandini and Churchland, 2013). The mouse as a model system for vision is not without downsides (Movshon, 2013), both experimental (e.g., small size) and biological (see below, e.g., poor spatial resolution and lack of directed eye movements), but other advantages make it a viable model.

What is known about mouse dLGN and V1 has grown rapidly in the last several years. Mouse retina has previously been the subject of intense characterization (Sun et al., 2002; Wässle et al. 2009; reviewed in Masland, 2012). The retinal outputs have been fully classified (Masland, 2012), and through combinatorial genetics individual ganglion cell classes can be isolated (Siegert et al., 2012). Much less is known about subsequent visual processing in mice. Anatomical evidence shows a lack of structure in mouse dLGN, but strikingly similar single cell morphology to other species (Krahe et al., 2011). *In vitro* work has shown the synaptic structure of mouse dLGN recapitulates that of cats. More specifically, the mouse dLGN has a triadic synaptic structure at retinal inputs, where the retinal bouton, the relay dendrite, and a neurotransmitter-releasing interneuron dendrite meet to form the so-called 'triad'. In the relay cell, directly stimulating the optic chiasm generates excitation from the retinal bouton followed by strong inhibition from the interneuron (Blitz and Regehr, 2005). This triadic synapse sequence was first elucidated in slices of cat dLGN, but the pharmacological details have been worked out in mouse slices. This and other slice work in mouse dLGN has advanced understanding of dLGN function (Chen and Regehr, 2000; Blitz and Regehr, 2003; Chen and Regehr, 2003; Acuna-

Goycolea et al., 2008; Wijesinghe et al., 2013), even in the absence of information about the responses of mouse dLGN to visual stimulation.

Pioneering physiological work by Drager (1975), established that mouse primary visual cortex shares some canonical features of the better-described feline and primate visual systems: retinotopy, orientation selectivity, and simple and complex receptive fields. Behavioral assessments showed mice to be capable of using visual information (Prusky et al., 2000). But because visual projections to superior colliculus had received the most attention (Drager and Hubel, 1975; Dunlop et al., 1996; Drescher et al., 1997), the neural basis of this behavior was questioned. Importantly, ablation of V1 revealed that this behavior was cortically mediated (Prusky and Douglas, 2004). Few other studies investigated canonical thalamocortical vision in mice.

The emergence of transgenic tools rekindled interest in mouse visual response properties. From this more recent wave, a new consensus has formed: poor spatial resolution, lack of orientation pinwheels, but good orientation tuning, temporal properties, receptive field structure, layer-like organization and parallel cortical processing streams (Gao et al., 2010). Measurement of receptive fields in the dLGN (Grubb and Thompson, 2003; 2004; Piscopo et al., 2013) and visual cortex (Niell and Stryker, 2008; Gao et al., 2010) have yielded V1 receptive fields about one order of magnitude larger than that seen in cats and primates, in the range of 5-15⁰ in diameter. This poor spatial resolution is confirmed by preferred spatial frequency of drifting gratings, at < 0.1 cycles/⁰. In spite of this, orientation tuning can be very sharp in mouse V1 (Niell and Stryker, 2008; Gao et al., 2010; Zariwala et al., 2010). Mouse V1 has simple and complex receptive fields, with more simple receptive fields in the middle layers, corresponding a thalamorecipient layer. Like other species, response properties in V1 indicate parallel but separate processing streams (Gao et al., 2010).

Given these similarities, one striking difference between mouse V1 and other species is the lack of orientation pinwheels (Ohki et al., 2006; Ohki and Reid, 2007). In cats and primates, cell somas with similar orientation preference cluster together, forming a smoothly varying

organization of orientation selectivity that resembles several pinwheels, visible at macrocellular (Bartfeld and Grinvald, 1992) and single cell (Ohki et al., 2006) resolution. This orientation map is superimposed onto other maps, like the retinotopic map. Mice have a retinotopic map, but lack any somatic organization in orientation, a feature we exploit in our studies of the structure of correlation in mouse layer 2/3.

The usefulness of comparative biology in visual neurophysiology

Visual neurophysiology as a field has been dominated by work in cats and non-human primates, in cats because of the excellent spatial resolution, front-facing eyes, and availability of experimental animals, and in non-human primates because of the homology to human primates. Mice share a more recent common ancestor to primates (in the *Euarchontoglires* clade) than cats and primates (in the *Boreoeutheria* magnorder) (Kriegs et al., 2006). Homologies in visual system organization between mice and primates represent traits either preserved from the common cat-primate ancestor or that arose before the divergence of primates and mice. Any of these homologies represent a fundamental feature of visual system organization preserved across evolutionary time. The visual receptive field first described in the invertebrate *limulus* (Ratliff and Hartline, 1959) bears a great resemblance to retinal and dLGN receptive field, and this homology across evolutionary distance cemented the receptive fields as a basic concept in visual system organization. This is an example of how the comparative approach, performing measurements of known quantities in one system in a new species can reveal factors important to basic function and preserved across species. We take this approach in making measurements of pairwise correlation structure in mouse layer 2/3 (Chapter 2) and dLGN response properties known in cats and monkeys in mice (Chapter 5).

Optogenetics

Beyond the power of comparative biology, using mouse dLGN allowed us to dig in to the growing optogenetics toolkit. Optogenetics, the manipulation of membrane potential in

mammalian cells using expression of bacterial or algal opsins and exogenously applied light is a rapidly spreading technique. It offers some significant advantages over other methods for manipulating neural activity: the opsins are genetically encoded, allowing for cell-type specific expression due to viral tropism (Nathanson et al., 2009), or other combinatorial expression systems such as the FLEX system (Atasoy et al., 2008). These opsins allow for single millisecond precision in spike generation, and can achieve similar timescale hyperpolarization (Chow et al., 2010). Continuing engineering of these proteins has improved the temporal resolution, increased sensitivity to allow for transcranial stimulation (JAWS, Boyden laboratory, MIT), and generated new tools like step-function opsins (Diester et al., 2011). In the early use of these tools, much focus has been on activating cells, perhaps due to the historical difficulty in achieving specific stimulation. Here, we utlize Channelrhodpsin-2 (ChR2) to stimulate a specific cell type, but in support of more extensive loss of function experiments using Archaerhodopsin-3 (Arch) to hyperpolarize during visual stimulation.

These opsins can be powerful tools for understanding the function of cell types in both physiology (Cardin et al., 2009; Adesnik et al., 2012), behavior (Gerits et al., 2012; Jazayeri et al., 2012), and disease (Gradinaru et al., 2009; Kravitz et al., 2010) through loss-of-function experiments, and for elucidating mechanisms of cell type action through gain-of-function activation in specific and varied experimental contexts.

The function of corticogeniculate-projecting cells

Anatomical tracings by Ramon y Cajal led him to comment on the number and density of fibers from cortex to thalamus, saying of them "An infinite number of fibers, coursing together with the previous ones, enter the [thalamic] nucleus under study and generate a fine and dense plexus" (in Pasik and Pasik, 2002). Indeed later anatomical studies led to the oft-quoted estimate of corticothalamic fibers outnumbering thalamocortical fibers by and order of magnitude (Sherman and Guillery, 1996), and corticothalamic inputs have been estimated at 30% of the total number of inputs to a dLGN relay cell (Erişir et al., 1997). Corticothalamic (CT) axons originate in

the deeper layers of V1, in both layers 5 and 6. However, the corticothalamic fibers of layer 5 do no project to primary sensory nuclei like the dLGN, but rather to secondary thalamic nuclei like pulvinar (Jones 2007). Corticothalamic axons originating in layer 6 project to both primary and secondary nuclei (Briggs, 2010; Thomson, 2010; Tombol,1984). Here, we focus on the corticothalamic axons in layer 6 projecting from primary sensory cortex to primary sensory thalamic nuclei, and will refer to these axons as 'corticogeniculate'.

Corticogeniculate (CG) axons follow the optic radiation back from cortex to dLGN, leave an axon collateral in the perigeniculate or reticular nucleus, and continue into dLGN to form synapses directly onto relay cells and interneurons. The synapses of CG axons onto relay cells are found at distal dendritic areas; CG axons excite relay cells via type 1 metabotropic glutamate receptors (mGluR1s) (McCormick and Krosigk, 1992; Rivadulla et al., 2002) and contain an NMDA component (Scharfman et al., 1990) at synapses that depress strongly during repeated stimulation (Jurgens et al., 2012). In addition, these axons bifurcate before exiting V1, sending an axon collateral up to layer 4. This local cortical projection targets all cell types in layer 4, including the excitatory stellate cells and local interneurons. Electron microscopy suggests a slight bias toward inhibitory cells in layer 4 (McGuire et al., 1984) and a net inhibitory effect. This net inhibition is supported by recordings in dLGN following stimulation of cortex (Widen and Amjone Marsan 1960; Olsen et al., 2012).

Given this synaptic arrangement, with direct excitation and two sources of disynaptic inhibition, CG projections are in position to provide general influence on dLGN responses. Indeed, corticothalamic projections have been shown to have both generally facilitative and suppressive effects on dLGN visual responses, though the effects are generally weak. Eliminating cortical activity increases responses to drifting gratings (Andolina, 2007, 2013, Baker and Malpeli, 1978); alternatively, other groups have concluded that eliminating cortical activity decreases responses to drifting gratings (Vastola, 1967; Hull, 1968; Przybyszewski et al., 2000; Rivadulla et al., 2002). Still others have observed *both* increases and decreases under their experimental

11

conditions (Kalil and Chase, 1970; Kayama et al., 1984; Molotchnikoff et al., 1986; McClurkin et al., 1991).

While most of these studies used drifting sinusoidal gratings (McClurkin et al., 1991; Przybyszewski et al., 2000; Rivadulla et al., 2002; Andolina et al., 2007), others used bars (Vastola, 1967; Hull, 1968; Kalil and Chase, 1970), and the size of stimuli ranged across studies. As a result, these spatial disparities have been invoked to explain the disparities in results: misaligned RFs providing suppression and aligned RFs facilitation. Direct evidence supporting this hypothesis has been obtained with paired recordings of single CG axons and single dLGN cells (Tsumoto et al., 1978). Further evidence comes from the effect of cortical activity on elements of dLGN single unit non-classical RFs. (Murphy and Sillito, 1987, 1988; Murphy et al., 1999; see Sillito and Jones, 2002). Another approach has been to focus on the temporal structure of dLGN responses and how CT projections alter this structure (Funke et al., 1996; Worgotter et al., 1998). Some consensus about CT feedback has emerged: a weak modulatory effect, not affecting spatiotemporal properties, that has divergent effects through depolarization to change firing mode. Even so, papers continue to appear that challenge this model (Andolina et al., 2013).

Here, we use the GN220 Nstr1-Cre line, created and distributed by the GENSAT project (Gong et al., 2007) to characterize specific and general effects of a genetically specified corticogeniculate cell population. This line, referred to hereafter as the Ntsr1-Cre line, restricts expression of Cre recombinase to a limited number of cells in cortical layer 6. The morphology of cells expressing Cre recombinase suggests that the Ntsr1-Cre line is comprised of a population of two cell types, both corticogeniculate. Both cell morphologies include a corticothalamic axon that targets the thalamic primary sensory nucleus that project to that cortical volume (Olsen et al., 2012). One cell type has dendrites that ramify locally in layer 6 as well as extend to layer 4; the other also has dendrites in layers 6 and 4, as well as a long apical dendrite that extends to and ramifies in layer 1. These types have been called type I and type II, and their function in visual processing remains controversial. By hyperpolarizing these cells using Arch, we explore the effect of these cells on V1 (Chapter 3) and dLGN responses (Chapter 4). Because our method differed

12

from previous approaches in specificity and in species, we attempted to use the simplest stimuli possible and to comprehensively characterize the effect of Ntsr1-CG cells. Briefly, we find similar results to some of those reported previously: both facilitative and suppressive effects of Ntsr1-CG projections that do not alter spatiotemporal properties, though we do not see evidence for changes in thalamic firing mode.

CHAPTER 2: THE STRUCTURE OF PAIRWISE CORRELATION IN MOUSE PRIMARY VISUAL CORTEX REVEALS FUNCTIONAL ORGANIZATION IN THE ABSENCE OF AN ORIENTATION MAP

Abstract

Neural responses to sensory stimuli are not independent. Pairwise correlation can reduce coding efficiency, occur independent of stimulus representation, or serve as an additional channel of information, depending on timescale of correlation and method of decoding. Any role for correlation depends on its magnitude and structure. In sensory areas with maps, like the orientation map in primary visual cortex (V1), correlation is strongly related to the underlying functional architecture, but it is unclear whether this correlation structure is an essential feature of the system or arises from the arrangement of cells in the map. We assessed the relationship between functional architecture and pairwise correlation by measuring both synchrony and correlated spike count variability in mouse V1. We observed significant pairwise synchrony, which was organized by distance and relative orientation preference between cells. We also observed non-zero correlated variability in both the anesthetized (0.16) and awake states (0.18). Correlated variability was associated with common excitatory input, but not direct excitatory connections. Our results indicate that the structure of pairwise correlation on any timescale is maintained in the absence of an underlying anatomical structure, and may be an organizing principle of mammalian visual system preserved by non-random connectivity within local networks.

Introduction

Throughout sensory systems, neurons are organized by response preference, so that like-responding neurons are close to each other, creating a functional map [e.g., orientation pinwheels in primary visual cortex (V1)]. Despite the ubiquity of maps, their role is unclear. For example, although rodent V1 lacks an orientation map (Ohki et al., 2005), single-cell orientation selectivity is not grossly different than in species with an orientation architecture (Niell and Stryker, 2008; Gao et al., 2010). In addition, correlations of spike output within a population of responding neurons are also organized by the underlying functional architecture. In V1, pairwise correlated activity depends on the pair's relative orientation preference (Kohn and Smith, 2005; Smith and Kohn, 2008), relative distance (Kruger and Aiple, 1988; Gawne and Richmond, 1991; Smith and Kohn, 2008), and among distant cells it is only observed between cells with similar orientation preference (Ts'o et al., 1986).

Correlations reflect the functional connectivity within a network (Perkel et al., 1967a). In addition, correlations can affect representation of information by a network in diverse ways, including influencing pooling (Zohary et al., 1994; Abbott and Dayan, 1999; Romo et al., 2003) and enhancing post- synaptic integration (Alonso et al., 1996; Cardin et al., 2010a). Any role for these correlations in sensory coding depends on the magnitude of correlation and the structure of correlation relative to space and stimulus parameters (Abbott and Dayan, 1999; Deneve et al., 1999; Pouget et al., 1999). In the presence of an orientation map, nearby neighbors often share selectivity for space and orientation, making the local structure of pairwise correlation difficult to determine.

To elucidate the local structure of pairwise correlation in V1, we utilize layer 2/3 of mouse V1, where distance between a pair of cells is independent of relative orientation selectivity. The structure of functional connectivity could reflect disordered functional architecture with random connectivity (Jia et al., 2010; Hofer et al., 2011; Hansel and van Vreeswijk, 2012). However, we hypothesized that synaptic specificity of inputs to (Yoshimura et al., 2005; Yoshimura and

16

Callaway, 2005) and within (Ko et al., 2012) layer 2/3 networks would result in a structure of pairwise correlations between neurons that is dependent on orientation and distance even in the absence of functional architecture.

We measured pairwise correlation on two timescales: a longer timescale of mean spike count on a trial-to-trial basis (r_{sc}) and a short timescale of synchrony within tens of milliseconds. We found that pairwise synchrony is dependent on the distance and the difference in orientation preference between the cells in each pair. Both visually evoked and spontaneous r_{sc} are also organized by pair distance and orientation preference. Our results show that, in mouse V1, specific synaptic connectivity maintains the structure of pairwise correlation despite the absence of a map.

Materials and Methods

Animal Preparation and Surgery

All procedures were done within the guidelines of the National Institutes of Health and were approved by the University of Pennsylvania Institutional Animal Care and Use Committee. Adult C57/B6 mice (8– 24 weeks) were initially sedated with a mixture of xylazine (10 mg/kg) and fentanyl (10 μg/kg); anesthesia was induced with a high concentration of isoflurane (5%) and maintained with continuous inhaled isoflurane (0.1–1%). Additional doses of fentanyl (5μg/kg) were administered every approximately 2 h to maintain anesthetic plane. The depth of anesthesia was monitored by heart rate (maintained between 300 and 600 beats/min), pupil dilation, pinch reflex, and fol- lowing the opening of the craniotomy by the level of synchronous activity in the local field potential (LFP). After placement in a stereotactic apparatus, eye moisture was maintained by application of a transparent lubricant and body temperature was maintained at 37℃ by rectal monitoring and a heating pad (FHC In c., Bowdoin, ME, USA). A 2-by-2 mm craniotomy was opened over V1. To minimize damage during electrode penetration, the dura was resected across the majority of the craniotomy using a dura hook and the exposed surface was coated with a layer of silicon oil. Following surgery, the entire stereotactic apparatus was rotated 60° to position the contralateral eye in front of t he display screen.

For separate set of animals (n = 3), a survival surgery was performed at least 1 week prior to a single recording session. During this surgery, two fixation bolts were permanently implanted and a V1 craniotomy was performed. The exposed V1 was covered with silicon oil and the opening resealed. On the day of recording, the mouse was head-fixed on a passive treadmill using the implanted bolts. The temporary seal over V1 was removed, mouse rotated 60° to position the contralateral eye, and tetrodes lowered as described above. The mouse was allowed to run freely and transitioned between passive and active behavioral states.

Electrophysiology

Following surgery, an array of four to six tetrodes (Thomas Recording GmbH, Giessen, Germany) arranged either linearly or concentrically was inserted into V1 perpendicularly relative to the cortical surface. In both configurations, the tip-to-tip space between neighboring tetrodes was 254 μm. Individual tetrodes were 100 μm in diameter with a central contact at the tip approximately 40 μm below three concentrically arranged contacts around the shaft approximately 20 μm from each other. Signals were preamplified by the tetrode drive and amplified, individually filtered, and acquired at 30 kHz using a Cheetah 32 acquisition system (Neuralynx, Boseman, MT, USA). High-frequency spiking activity was isolated at each contact by filtering between 600 and 6000 Hz. A single channel from each tetrode was duplicated and filtered 0.1–375 Hz to record an LFP. Each tetrode was individually inserted to an initial depth of 100–160 μm. Following a rest period of at least 30 min, each tetrode was lowered through the cortex in 2-μm steps until at least one strong unit was present; in this dataset, all tetrodes were stopped before reaching approximately 350 μm below the cortical surface, the putative boundary of layers 3 and 4.

Visual Stimuli

All visual stimuli were generated using the ViSaGe stimulus generation hardware (Cambridge Research Systems, Cambridge, UK) and a custom software package utilizing the accompanying MATLAB (Math- works, Natick, MA, USA) toolbox. Stimuli were displayed on a 19-in cathode ray tube monitor configured to refresh at 100 Hz. This monitor was gamma-corrected using a luminometer and ViSaGe configuration software and placed 30 cm from the eye contralateral to the craniotomy. Full-screen stimuli covered approximately 70° of visual field. After tetrode insertion, the screen was set to a background of 50% luminance. Stimuli consisted of drifting sinusoidal gratings. To drive responses from as many cells as possible, all stimuli were 100% contrast and 0.04–0.06 cycles/°, in line with previous reports in mouse visual cortex (Niell and

Stryker 2008; Gao et al. 2010; Niell and Stryker 2010). The 70°stimuli were sufficiently large, as the visual space recorded by our most distantly spaced electrodes is approximately 30°, given the median size of a mouse V1 receptive field (Gao et al., 2010) of all cell pairs recorded up to 500 μm are at least partially overlapping (Bonin et al., 2011).

Spike Clustering and Data Analysis

Spike waveforms from each tetrode were clustered into individual units offline using a mixture of algorithmic and manual sorting (Spike- Sort3D, Neuralynx). Waveforms were initially sorted using KlustaKwik and subsequently manually refined (e.g., Fig. 1A,B). All clusters with spikes in the 0–1-ms bin of the interspike interval histogram were strictly rejected. To assess the quality of separation of the identified single units, we measured isolation distance and the L-ratio for each cluster (Fig. 1C), which indicate the distance of the center of the cluster from the noise and the quality of the moat around the cluster, respectively (Schmitzer-Torbert et al., 2005). An example set of clustered data in Figure 1A–C shows the isolation of 6 single units from one tetrode, with isolation distances >10 and L-ratios <0.4.

All analysis of single-cell and pairwise spikes was done using Igor Pro 6.0 (Wavemetrics, Lake Oswego, OR, USA) at 1-ms resolution. Orientation tuning was quantified using the average number of spikes over the duration of stimulus presentation. The orientation tuning curves, across the range 0–360°, were fit with the von Mises funct ion (Swindale, 1998):

$$f(\theta) = b_0 + b_1 e^{K(\cos(\theta - \mu) - 1)} + b_2 e^{K(\cos(\theta - \mu + \pi) - 1)}$$

where b_0 is an offset for the baseline firing rate, b_1 and b_2 independently determine the size of each peak, K is the width parameter, and μ the preferred orientation. The maximum value of this fit was used as the cell's preferred orientation, and the half width at half height indicates the bandwidth of orientation selectivity. The difference in preferred orientation (Δθ) is the difference

20

between the maxima for a pair of cells. Orientation selectivity index (OSI) was calculated, from

raw responses, as the difference between responses at preferred and orthogonal orientations as

follows:

$$OSI \ = \ \frac{R_{preferred} - R_{ortho}}{R_{preferred} + R_{ortho}}$$

where $R_{preferred}$ is the response at the preferred orientation, as deter- mined by the circular

Gaussian fit, and R_{ortho} is the response at the orientation 90° from $R_{preferred}$. All reported p-

values were calculated using the Wilcoxon rank-sum test.

Correlation Measures

Correlation between pairs of cells was measured on two timescales: trial-to-trial variation in spike

count (r_{SC}) and synchrony within 10 ms. Correlated variability was defined as the shared

variation, either increase or decrease, in the number of spikes fired over a given time window.

The time window used here was the duration of stimulus presentation, which was 2 s. To

calculate the r_{SC} for a given pair, the response of each cell was assigned a z-score for each trial:

$$z = \frac{x - \mu}{\sigma}$$

where x is the rate on a given trial, μ the average rate for all trials, and σ the variance. The

Pearson correlation was computed as the product of z-scores between a pair summed across all

trials:

$$r_{sc} \ = \ \frac{1}{n-1} \sum_{i=1}^{n} \left[\left(\frac{X_i - \bar{X}}{\sigma_X} \right) \left(\frac{Y_i - \bar{Y}}{\sigma_Y} \right) \right]$$

where n is the number of trials, X_i and Y_i the rates for each cell on a given trial, X and Y the

sample means for each cell, and σ_X and σ_Y the sample variance for each cell.

Synchrony was calculated as a peak in a cross-correlogram (CCG) occurring within 10

ms of the zero line. To produce CCGs, we followed Perkel et al. (1967a) to compute raw cross

21

correlation; to account for differences in firing across the population, each CCG was divided into the geometric mean of the firing rates of the pair of cells. CCGs were further corrected by the jitter-correction method (Smith and Kohn, 2008; Harrison and Geman, 2009)) using a 50-ms jitter window. Choosing this window size destroys all correlations <50 ms in the correction term, but preserves correlation on all longer timescales. Subtraction of this correction term isolates only the correlation in the raw CCG that occurs on the <50 ms timescale. The presence of a synchronous peak was assessed using a threshold set 2 standard deviations (SD) above the mean level of correlation. Mean correlation was here defined as the mean of the corrected CCG from 100 to 200 ms. The magnitude of synchrony was determined as the area between the threshold and the CCG ±10 ms from the zero line. The correction method used did not affect the presence or the size of synchronous peak (see Fig. 3C,D). All measurements reported here are based on jitter-corrected CCGs.

To statistically justify the separation of CCG shapes into classes, we measured several parameters from each CCG: width, peak lag, and symmetry. Width was measured at the crossing of the significance threshold. Peak lag was the difference between zero and the time at which the peak occurred. CCG symmetry was measured as follows:

$$symmetry = \frac{P_0}{P_{max}}$$

where P_0 is the magnitude of the peak at time zero and P_{max} the magnitude of the peak. This measure was taken over ±100 ms, and all values below the significance threshold were treated as baseline (i.e. given a CCG magnitude of zero).

Results

Our goal was to quantify visually driven and spontaneous pair- wise correlations of neurons in the supragranular layers 2 and 3 (L2/3) of mouse V1 as a function of their relative distance and their similarity of orientation preference. We recorded single neurons from L2/3 of V1 of anesthetized mice (n = 38) using six independently positioned tetrodes. To minimize sampling bias, the position of the tetrodes in L2/3 was not readjusted once a set of cells was detected within the first 370 μm from the pial surface. Individual units were identified using an offline, partially automated clustering procedure (see Materials and Methods; Fig. 1A–C). Each tetrode sampled up to seven single neurons simultaneously. To maximally drive spiking activity from each population of simultaneously recorded neurons, we used full screen, 100% contrast, drifting sinusoidal gratings optimized in spatial and temporal frequencies for mouse V1 (0.06 cycles/°, 2Hz; Niell and Stryker 2008; Gao et al. 2010). The example cell in Figure 1D responded to repeated presentations of an optimally oriented drifting grating with a nonmodulated increase in the firing rate (mean = 7.2 Hz). The visual response was robust and consistent across trials, as shown by the raster plot (consecutive trials from top to bottom); this cell showed characteristic strong adaptation during the course of the grating as illustrated by the decrease in frequency in the peristimulus time histogram (PSTH, in light gray). Our population consisted almost exclusively of nonmodulating cells with an F_1/F_0 ratio compatible with a classification as complex cells (Supplementary Fig. 1).

We plotted the mean firing rate as a function of stimulus orientation (n = 20 presentations of each orientation) and used a circular Gaussian fit to generate the orientation tuning curve (Fig. 1E). This cell had a preferred orientation of 223°and a n OSI of 0.72. We included in our database all cells which fired a minimum of 400 spikes over the 20 min required for the stimulus block, resulting in a total of 648 cells and 4160 simultaneously recorded pairs. Across the population, the mean evoked firing rate was 6.4 ± 7.0 Hz (mean ± SD), spontaneous firing rate was 0.29 ± 0.34 Hz, and the mean half height at half width of orientation tuning curves was 23°± 8.3°. The OSI distribution was clearly bimodal with a large number of cells highly selective for stimulus

orientation (>0.8 OSI) and a large number with weak selectivity (<0.4 OSI). However, there were only 3 untuned cells in our database with OSIs <0.2 (Fig. 1F, left panel). The response properties of the cells in our database were consistent with recent quantitative descriptions of mouse V1 (Niell and Stryker 2008; Gao et al. 2010).

Quantification of Correlation

☐ We quantified correlated firing for each pair of simultaneously recorded cells on two timescales, according to previously established methods (Perkel et al. 1967; Smith and Kohn 2008): (1) synchrony, which measures the pairwise correlation of spike times within ±10 ms, and (2) correlated variability (also called noise correlation, or r_{sc}), which measures the trial-to-trial correlation of spike counts over the duration of each trial (2 s). All measurements of correlation were made from responses to 2 Hz drifting gratings of varying orientation, sufficient to elicit a response from many cells on each trial. Correlations induced by the temporal frequency of these stimuli are broader than the synchrony measured.

We quantified synchrony from the pairwise CCGs (bin = 1 ms) normalized by the geometric mean firing rate and corrected using the subtraction of a 50-ms jitter-correction term to remove stimulus-induced correlation (see Materials and Methods). The "magnitude" of synchrony was the area of the central peak (±10 ms) of the CCG exceeding 2SD above base- line noise (Fig. 2A, the dotted line indicates 2SD; see Materials and Methods). The "probability" of synchrony was the ratio of the number of pairs with a significant peak over all recorded pairs. We further subdivided the population of significant CCGs based on the position of the peak with respect to the zero line. A positive peak entirely displaced from the zero line was classified as "offset" synchrony (Fig. 2A, left; n = 90/4160).

This shape is not sufficient to demonstrate a direct connection, but is the most likely

24

explanation for such a shape (Perkel et al. 1967; T'so et al. 1986; Ostojic et al. 2009). A positive peak straddling the zero line was classified as "zero spanning," and is consistent with a shared source of excitatory input (Fig. 2A, right; n = 234/4160; Perkel et al. 1967). Most zero-spanning peaks were not centered over the zero line (164/234 zero-spanning peaks). The remainder of zero-spanning peaks were centered on zero (70/234). This ad hoc classification of CCGs as offset or zero spanning was supported by the difference in the distribution of peak widths (Fig. 2B), showing statistically different means (Fig. 2E; $P < 0.005$). The distribution of peak lags, defined as the time of peak relative to zero, was complementary: zero-spanning CCGs were centered on zero (Fig. 2C, right), while offset CCGs had a bimodal distribution with centers at 5 and –5 ms (Fig. 2C, left). The absolute peak lag was significantly larger for offset CCGs than zero-spanning CCGs (Fig. 2E, center; $P < 0.005$). To formalize the difference between the two CCG classes, we measured peak symmetry relative to zero (see Materials and Methods). This value is 1 for peaks exactly centered on the zero line and 0 for peaks fully shifted from the zero line. All offset CCGs showed high asymmetry (Fig. 2D, left). Zero-spanning CCGs (Fig. 2D, right) had a bimodal distribution of symmetries, with a population of highly symmetrical CCGs (symmetry >0.4; mean: 0.79 ± 0.02) and a population of asymmetrical, yet zero-spanning, CCGs (symmetry <0.4; mean: 0.26 ± 0.005). The subset of symmetrical zero-spanning CCGs was similar to the full population of zero-spanning CCGs in all measurements made subsequently (Supplementary Fig. 2), and so all zero-spanning CCGs were grouped to maximize statistical power.

We tested several factors that could affect measurements of CCG magnitude. We compared the CCG magnitude measured using the jitter-correction method (Smith and Kohn 2008) with two other forms of stimulus correlation removal: shift correction and shuffle correction (Fig. 3A,B). The method removal of stimulus correlation did not significantly reduce the size of the zero-spanning CCGs or offset CCGs (Fig. 3B–F). Further, to account for correlations during any onset transient, we removed the first 250 ms of each response after correcting each CCG (Fig.

3C,D). The removal of this onset transient reduced the peak of some pairs slightly (Fig. 3D), but the reduction in CCG magnitude was not significant and smaller than the percentage of spikes removed.

We included pairs recorded on the same tetrode, despite the inability to detect near synchronous spikes for such pairs due to acquisition enforced dead times; because of this, we removed the zero-lag bin from all CCGs from pairs on the same electrode. Peaks from the cells recorded on the same tetrode reflected both forms of synchrony (e.g., Fig. 4A). Removing the zero-lag bin affected the classification of CCGs as offset or zero spanning in only 1 of 90 offset CCGs.

We quantified trial-to-trial correlated variability, or r_{SC}, as the Pearson correlation coefficient of standardized mean firing rates across the duration of a trial. This measure is equal to 1 when the covariance between a pair is perfect and 0 when a pair of cells does not covary.

Synchrony as a Function of Orientation Preference

We first examined the dependence of synchrony on the difference in orientation preference, regardless of the distance between neurons in each pair. The difference in orientation preference ($\Delta\theta$, range = 0–90°) was measured as the difference bet ween preferred orientation of the 2 cells in each pair, esti- mated from the Gaussian fits to the orientation tuning curves (as illustrated in Fig. 1). Figure 4A illustrates 3 cells that were isolated on the same tetrode (indicated in black) and therefore, within an approximate radius of approximately 200µm (Buzsáki et al., 2012). We chose to illustrate a group of cells re- corded from the same tetrode to emphasize the fact that neurons in close proximity may show very different orientation preferences (Ohki et al. 2005). Cells 1 and 2 differed only by 18° in their optimal orientation (cell 1: 255° and cell 2: 273°), but diverged by 53° and 35°, respectively, from cell 3 (128°). Cros s-correlation revealed zero-spanning synchrony

26

with a magnitude that was dependent on the similarity of orientation preference despite the proximity of the neurons. The strongest synchrony was observed within the pair with the most similar orientation preference (CCG peak = 0.016, cells 1 and 2), while the pair with largest difference in orientation preference showed no significant synchrony (cells 1 and 3), and the intermediate orientation preference difference showed weaker synchrony (CCG peak = 0.002, cells 2 and 3). This example is inconsistent with the synchrony observed between neighboring neurons at pinwheel singularities in cat visual cortex, where the magnitude of synchrony of nearby neighbors is unaffected by difference in orientation preference (Das and Gilbert, 1999).

We obtained population measures of the relationship between synchrony and orientation tuning separately for zero-spanning (Fig. 4B) and offset CCGs (Fig. 4C). For zero-spanning synchrony, the probability (gray) and magnitude (black) of synchrony were dependent on $\Delta\theta$ and were fit by exponential decay functions (x^2_{prob} ¼ 4 10^{-4}; x^2_{mag} ¼ 4 10^{-5}; Fig. 4B). The probability of zero-spanning synchrony was higher for cell pairs whose preferred orientations differed by <30° than for cell pairs with less similar orientation tuning (Fig. 4B). As a function of $\Delta\theta$, the magnitude of zero-spanning synchrony decreased more slowly (τ_{mag} = 126.2°) than the probability (τ_{prob} = 19.9°; Fig. 4B). To determine a criterion $\Delta\theta$ value for magnitude zero-spanning synchrony, we compared each 10° $\Delta\theta$ bin to the first bin (0°– 10°); the first significantly different bin was 40–50° (P = 0.03), and all subsequent bins were significantly different (P < 0.05). We conclude that zero-spanning synchrony is both strongest and most likely within pairs with $\Delta\theta$ < 40°, reflecting the specificity of L4 projections to L2/3.

For offset synchrony, probability and magnitude were also dependent on $\Delta\theta$ and were fit by exponential decay functions (x^2_{prob} ¼ 7:5 10^{-5} ; x^2_{mag} ¼ 8:8 10^{-5} ; Fig. 4C). The magnitude of offset synchrony decayed similar to probability (τ_{mag} = 15.6° and τ_{prob} = 9.3°). The probability of offset synchrony was small and relatively flat for $\Delta\theta$ greater than 30° (Fig. 4C). The criterion $\Delta\theta$ value for offset synchrony was 10–20° (P = 0.003), and all subsequent bins were significantly

different (P < 0.05); the exponential decay saturated >40°. We conclude that the strength of offset synchrony is strongest within pairs with Δθ < 40°, consistent with in vitro measurements of synaptic connections between neighboring cells of known orientation preference (Ko et al. 2011).

The dependence of synchrony on firing rate could affect this measurement (la Rocha et al., 2007), as dissimilarly tuned cells are less likely to fire spikes on the same trial. However, across Δθ, rate-matched pairs yielded exponential fits similar to the full dataset (data not shown), indicating that the effect of stimulus selectivity on synchrony is not dependent on rate.

Synchrony as a Function of Distance

We next considered how the distance between a pair of cells affects synchrony independent of their difference in orientation preference. We found that the distance between a pair of cells, as measured by electrode spacing, significantly affected the probability and magnitude of both types of synchrony. The example in Figure 5A shows three neurons recorded from three tetrodes spanning 508 μm. The orientation preference of these cells was very similar, differing by only 4–8° (cell 1: 221°, cell 2: 217°, and cell 3: 225°). Despite the considerable distance between cells 1 and 3, they had a significant zero-spanning CCG peak (magnitude = 0.012). One closer pair had a larger synchrony magnitude in spite of having similar Δθ (cells 1 and 2: 0.026), demonstrating the effect of distance on the magnitude of zero-spanning synchrony, while another closely spaced pair had weaker synchrony (cells 2 and 3: 0.001).

For the population, the decay of probability and magnitude of zero-spanning synchrony as a function of distance were well fit by an exponential decay (x^2_{prob} ¼ 5:7 10^{-3} ; x^2_{mag} ¼ 1:4 10^{-5}; Fig. 5B). Probability decayed slightly faster than magnitude but on the same order of magnitude (τ_{prob} = 491.0 μm; τ_{mag} = 662.8 μm). Magnitude dropped significantly at the 508-μm distance (Fig. 5B; P = 0.01). The probability of offset synchrony fell exponentially with distance

28

(χ^2 = 2.2 × 10^{-6}; Fig. 5C) much faster (τ_{prob} = 162.9 µm) than zero-spanning synchrony. The

magnitude of offset synchrony decayed quickly (χ^2_{mag} ¼ 5:4 10^{-6}; τ_{mag} = 72.7 µm), though

the few observations of offset synchrony at distances >508 µm were not significantly smaller than

those at smaller distances (P > 0.05). Our measurements constrain the spatial extent of the

functional networks described by zero-spanning and offset synchrony. The spread of zero-

spanning synchrony suggested a wider feedforward network, approximately 1 mm in diameter,

compared with a more constrained functional network of offset synchrony, <400 µm in diameter.

Width of Synchrony as a Function of Distance☐and Orientation Preference☐

The width of the synchronous peak can affect the measurement of synchrony strength and may

be regulated by distinct mechanisms in V1 (Kohn and Smith 2005). Within the allow- able window

of ±10 ms, we measured the width of the synchronous peak at the point of crossing the 2SD

significance threshold. Offset synchrony peaks were significantly narrower (4.8 ± 2.77 ms) than

zero-spanning synchrony (8.7 ± 3.29 ms; P < 0.005, Wilcoxon rank test, Fig. 2B). Narrower offset

synchrony peaks are compatible with the underlying hypothesis that this form of synchrony arises

from a single source, while zero-spanning peaks can arise from multiple sources. For both types

of synchrony peak, peak width was positively correlated with CCG magnitude, though weakly

(Fig. 6A; slope of the linear fit, zero-spanning: 0.48 × 10^{-3} ± 0.28 × 10^{-3}; offset: 0.67 × 10^{-3} ±

0.45 × 10^{-3}). There was no trend in peak width, either offset or zero-spanning, over difference in

preferred orientation (Fig. 6B). Zero-spanning synchrony was narrower for nearby cells (<500

µm), even though these nearby pairs had higher synchrony magnitude (Fig. 5B), but still not as

narrow as offset synchrony (Fig. 6C). Across the distances measured, the width of offset

synchrony peaks was un- changed (Fig. 6C).

Synchrony as a Function of Both Orientation Preference and Distance

Finally, we measured the codependence of both forms of synchrony on distance and Δθ, a measurement that is straightforward here because distance and orientation preference are independent across the topography of mouse visual cortex (i. e., there are no orientation pinwheels). Across a network of approximately 1 mm, zero-spanning synchrony is more likely and of larger amplitude for neurons with similar orientation preference (Fig. 7A–C). The probability and magnitude of zero-spanning synchrony decreased as a function of distance across all Δθ. Notably, probability and magnitude appeared to have the same structure over distance and Δθ, reflecting the stimulus specificity of the common input presumably originating in L4 and responsible for the orientation selectivity of L2/3 neurons.

In contrast, the probability of offset synchrony was nearly independent of Δθ for nearby cells (<500μm; Fig. 7D). However, the magnitude of offset synchrony between neighbors was highly dependent on Δθ, falling for Δθ > 20°. Thus, within smaller networks (<500 μm), connectivity is wide- spread but the strength of connectivity is Δθ specific. For further separated pairs (>500 μm), the probability of connection was lower and limited to pairs with Δθ < 30°; observations of offset synchronous pairs separated by >500 μm and with Δθ > 30° were rare and always of very small magnitude (Fig. 7E). Thus, our measurements show that the mechanisms that generate zero-spanning, but not offset, synchrony between nearby cells (within approximately 200 μm) show specificity to the orientation preference within the pair. For longer-range connections, both forms of synchrony show specificity for the orientation preference within the pair.

To fully characterize the structure of functional connectivity, we created a measure of connectivity strength by multiplying the probability of observing synchrony by the magnitude of the synchrony observed at each distance and Δθ (Fig. 7C,F). We call this metric functional connectivity "power". For zero-spanning synchrony, connection power showed a similar

parametric dependence on distance and Δθ as probability and magnitude alone. That is, the strongest zero-spanning power was for nearby and similarly tuned cells, decreasing with both distance and Δθ (Fig. 7C).

The power of offset synchrony had a similar parametric dependence as the power of zero-spanning synchrony, again showing the strongest functional connectivity for nearby and similarly tuned cells, decreasing with both distance and Δθ (Fig. 7F). Unlike zero-spanning power, the structure of the power of offset synchrony was however created by the combination of complementary dependencies: the effect of Δθ at distances >500 μm was conferred by the probability (Fig. 7D), while the effect of Δθ at local distances was conferred by the magnitude (Fig. 7E). These plots demonstrate that functional connectivity can be organized in the absence of a functional architecture. In addition, the powers of functional connectivity of zero-spanning and offset synchrony show matching organization: highest for nearby cells with the similar orientation preference, lowest for distant pairs of the orthogonal orientation preference. Our data show functional connectivity that reflects the synaptic specificity of input to and within layer 2/3, in agreement with predictions based on in vitro measurements (Yoshimura et al., 2005; Ko et al., 2012).

Correlated Variability

The correlated fluctuation of trial-to-trial response magnitude, or correlated variability (r_{SC}), can have repercussions for how populations of neurons represent sensory responses from both the encoding and decoding perspectives (Johnson 1980; Zohary et al. 1994; Panzeri et al. 1999; Pouget et al. 2003; Averbeck and Lee 2006; Averbeck et al. 2006; Cohen and Kohn 2011). Under our conditions, we observed an evoked r_{SC} across our population of 0.16 ± 0.003 (mean ± SD; Fig. 8A, left, gray histogram, mean indicated by gray arrow). This value is similar to that measured in anesthetized macaque V1 over a comparable scale (Gawne and Richmond 1993;

Reich et al. 2001; Kohn and Smith 2005; Smith and Kohn 2008) and cat V1 (Das and Gilbert, 1999). We quantified a "spontaneous" r_{SC} using the periods between presentations of visual stimuli. To account for adaptation effects from the preceding stimulus, we calculated a spontaneous r_{SC} from periods subsequent to stimuli of the same orientation, and averaged across all orientations. Ac- counting for adaptation effects reduced spontaneous r_{SC} primarily for nearby pairs (data not shown). The r_{SC} calculated from epochs of spontaneous activity (0.15 ± 0.005; Fig. 8A, black histogram, mean indicated by black arrow) was not significantly higher than evoked r_{SC} ($P = 0.13$). Spontaneous r_{SC} was highly correlated with evoked r_{SC} (linear fit slope = 0.82 ± 0.02, $R^2 = 0.47$, Fig. 8A, right).

Correlated Variability as a Function of Distance⬜and Orientation Preference⬜

At our spatial scale, we observed a dependence of evoked r_{SC} on distance, well fit by an exponential decay function ($\chi^2 = 0.004$, т = 209.9 µm; Fig. 8B, left panel). It is important to note that although the area of cortex over which we measured correlation (approximately 1mm) is more limited than in studies of other species, the span of visual space covered by our recordings is actually slightly larger (approximately 60°of v isual space; Kalatsky and Stryker 2003). The decay in evoked r_{SC} with distance (т = 209.9 µm; Fig. 8B, left) was most similar to the decay in offset magnitude (т = 162.9 µm; Fig. 5C). The fit parameters used to fit the magnitude of offset synchrony fit the decay of evoked r_{SC} with $\chi^2 = 3 \times 10^{-4}$, consistent with a conclusion that trial-to-trial correlated variability is at least partially mediated by connectivity within L2/3.

We further investigated correlated variability by examining the relationship between Δθ and r_{SC}. In the presence of functional architecture, evoked r_{SC} depends on orientation tuning similarity (Smith and Kohn 2008). While we did observe an initial decay of evoked r_{SC} with

32

increasing Δθ, evoked r_{SC} in- creased at larger Δθ leading to a slightly U-shaped dependence

(Fig. 8C, left). Still, this dependence was fit with an exponential decay (τ = 11.7°, $\chi^2 = 2 \times 10^{-4}$).

Finally, we were able to measure the codependence of evoked r_{SC} on distance and Δθ

(Fig. 8D, left), as we did for synchrony (Fig. 7). At short distances, evoked r_{SC} depended on Δθ,

while at distances >500 μm, r_{SC} was independent of Δθ. The two-dimensional relationship of

evoked r_{SC} closely matched that of synchrony power. We further explore the relationship between

evoked r_{SC} and functional connectivity below (Fig. 10). The structure of evoked r_{SC} demonstrates

that correlation can be organized in the absence of functional architecture.

Correlated Variability of Spontaneous Activity

The correlated variability of spontaneous activity could have different spatial properties than that

of evoked activity. Similar to evoked r_{SC}, we observed a dependence of spontaneous r_{SC} on the

distance between the pair (Ch'ng, 2010) (τ = 235.3 μm, $\chi^2 = 0.013$; Fig. 8B, right). Δθ had a weak

effect on the measured spontaneous r_{SC} (τ = 3.0°, $\chi^2 = 3 \times 10^{-4}$; Fig. 8C, right). A stronger

dependence of spontaneous r_{SC} on Δθ was apparent for nearby pairs (Fig. 8D, right), as has

been previously observed in rodents (Ch'ng and Reid 2010). The relatively flat spatial and

orientation tuning structure of spontaneous r_{SC} (Fig. 8D, right) suggests that the source of input

responsible for these correlations operates nonspecifically over a distance >1 mm in mouse V1,

distinct from the sources of synchrony.

Correlated Variability as a Function of Network State

It has been argued that the conditions that give rise to correlated variability of the magnitude

33

observed here are not physiologically relevant (Ecker et al., 2010), namely that correlated

variability is aberrantly increased by several factors, including clustering error and anesthetic-

induced network state. To assess the role of network state on correlated variability, we quantified

network synchronization using the spectral content of LFP recordings. The level of gamma

activity either immediately preceding or during evoked activity did not affect the value of r_{SC}

observed (Supplementary Fig. 3). To more directly assess the role of anesthesia on r_{SC}, we

measured r_{SC} in awake, head-fixed mice under the same visual stimulus paradigm. Under these

conditions, spontaneous and evoked firing rates were higher than under anesthesia (spontaneous

mean: 2.8 ± 2.12 Hz; evoked mean: 8.082 ± 7.52 Hz; Fig. 9A), but cells showed similar

orientation tuning (Fig. 9B). As such, these conditions eliminate two of the proposed confounding

factors in measuring r_{SC}: anesthetic-induced synchronization and dampened firing rates. Despite

this, evoked r_{SC} was very similar in the anesthetized and awake states (anesthetized: 0.16 ±

0.002, awake: 0.18 ± 0.03, P = 0.34; Fig. 9C). In contrast, spontaneous r_{SC} (0.03 + 0.01) was

much lower in the awake state than that observed in the anesthetized state (anesthetized: 0.36 ±

0.004, P < 0.01; Fig. 9C), likely due to the lack of a slow oscillation in the LFP. In summary,

measurements of correlation in the awake state were not different than those measured under

our anesthetic regime.

The Relationship Between Correlated Variability and Synchrony

To investigate the origin of correlated variability, and to directly assess the relationship between

the two timescales of correlation measured here, we sought to determine if correlated variability

was predictive of either the probability or the magnitude of synchrony between pairs. To do this,

we classified each of the 4160 pairs based on their value of evoked and spontaneous r_{SC}. We

sorted each pair into one of three classes: High, moderate, or low r_{SC} according to the distribution

of r_{SC} values (Fig. 10A). The thresholds for high (evoked $r_{SC} > 0.36$; spontaneous $r_{SC} > 0.31$; Fig. 10A,B, light gray) and low (evoked $r_{SC} < -0.04$; spontaneous $r_{SC} < -0.02$; Fig. 10A,B, black) classes were set one SD above and below the mean, respectively. The probability (Fig. 10C, left) and magnitude (right) of zero-spanning synchrony within each r_{SC} class were highest for pairs with high evoked r_{SC}. In contrast, the probability and magnitude of zero-spanning synchrony were highest for pairs close to the mean value of spontaneous r_{SC} (Fig. 10C, right), indicating a dissociation of the source of spontaneous r_{SC} from both evoked r_{SC} and zero-spanning synchrony. We observed even probability of offset synchrony across evoked r_{SC} classes, with higher CCG magnitude for pairs with midlevel r_{SC} (Fig. 10D), suggesting the mechanisms that generate offset synchrony have relatively less impact in determining the correlation of spike count variability.

Discussion

We measured the pairwise correlation of spike output in mouse V1 in response to visual stimulation on two timescales: synchronous spikes within ±10 ms and covariations in the mean evoked firing rate. Each has implications for information processing, depending on the neural implementation of de- coding. We measured synchrony using pairwise CCGs and found that both the magnitude and probability of positive CCGs were a function of the difference in orientation tuning and distance between the two neurons in the pair, a functional structure despite the absence of columns.

We measured pairwise correlated variability (r_{SC}) of mean trial spike counts using Pearson's correlation coefficient. We found a small but significant value of r_{SC} (0.16 ± 0.01), similar to most of the studies in the literature. This magnitude was not due to anesthesia, as it was not significantly different in awake, actively moving mice. We found that r_{SC} depended on inter- neuronal distance and on the difference of orientation preference. Our results revealed a structure of neuronal correlations independent of a functional architecture.

Synchrony and Functional Connectivity

Cross-correlation techniques were originally developed to demonstrate functional connectivity between pairs of neurons (Perkel et al. 1967). We observed two types of positive CCG. The most common (234 of 4160 pairs; 5.6%) was a central peak straddling the zero line. We classified these as zero-spanning input because this shape could encompass complex synaptic arrangements, including common excitatory input and direct connections. The second type of CCG (90 of 4160; 2.2%) showed the entire positive peak offset from the zero line by a few milliseconds, compatible with monosynaptic latency. While this shape is not sufficient to establish connec- tivity, which can only be demonstrated with dual simultaneous intracellular recordings

(Thomson and Lamy 2007) or electron microscopy (Bock et al. 2011), we consider this evidence of a direct excitatory connection (Perkel et al. 1967; Ostojic et al. 2009).

At the short distances recorded by a single tetrode, the probability and magnitude of zero-spanning synchrony decreased as a function of relative orientation preference (Δθ) (Fig. 7). As in columnar organization, L2/3 visual responses were dominated by orientation-specific L4 input, in agreement with specific connectivity between L4 and subnetworks of L2/3 pyramidal cells demonstrated in rodent visual cortex in vitro (Yoshimura and Callaway 2005). In contrast, the probability of offset synchrony at short distances was not dependent on Δθ, consistent with diffuse L2/3 pyramidal cell axons in the local vicinity (Malach et al. 1993; Bosking et al. 1997; Van Hooser et al. 2006). As opposed to apparent local promiscuity, distant functional connectivity (>500 μm) was highly dependent on orientation tuning as in cat (Ts'o et al. 1986; Gilbert and Wiesel 1989; Bringuier et al. 1999), ferret (Tucker and Katz 2003), and macaque (Smith and Kohn 2008) V1. Our measurements suggest that common input is strongest within a 500-μm radius, matching the width of a receptive field, while strong offset synchrony spanned a shorter distance (Fig. 5B,C). In- stances of offset synchrony that span longer distances linked excitatory cells with similar orientation preference over approximately 30° of visual space.

To provide a more complete picture of functional connectivity, we generated a metric that combines probability and magnitude, called connection "power." Like postsynaptic potentials (Ko et al. 2011), functional connectivity "power" de- pended on orientation and distance, for both zero-spanning and offset synchrony. Our results identify a functional role for specific synaptic connections: the organization of synchronous spike generation in local networks.

Observations of networks of synchronous cells are critical for large-scale models of V1 (McLaughlin et al. 2003; Seriès et al. 2004). Our observation of structured functional connectivity does not support models based on local random connectivity, either vertical or horizontal (Hansel and van Vreeswijk 2012).

Structure of r_{SC} and Synchrony

Columnar organization determines that nearby neurons share tuning properties and similar noise sources. As a result, there is significant correlation between tuning properties and trial-to-trial variability. In mouse V1, however, such arrangement is not trivial. Our data show that synchrony "power" decays exponentially along both the orientation and distance dimensions. We suggest that synaptic specificity within the apparent orientation domain disorganization preserves the structure of functional connectivity. Correlated variability is also weakly organized in the orientation domain (Fig. 8C); this structure may be partially inherited from contributions of functional connectivity (Fig. 10). Regardless of origin, our data indicate that the structures of correlated variability and synchrony represent an organizing principle of mammalian visual systems.

Along the distance domain, the decrement in synchrony in mouse V1 matched that in macaque V1 (Smith and Kohn 2008), when interneuronal distance is considered in terms of visual space. In mouse, correlation extended over less physical brain distance but more visual space, by a factor of 30 (30 vs. approximately 1'). This difference can be partially accounted for by the difference in receptive field diameter. As in macaque, synchrony in mouse V1 required some receptive field overlap, though less: we observed synchrony at all levels of overlap, whereas monkey required >50% overlap. Synchrony in cat V1 does not strictly require overlap (Ts'o et al. 1986), but it is dependent on the amount of overlap.

Spike Count Variability and Coding

Small pairwise correlations in variability limit the effectiveness of increasing the signal-to-noise ratio by pooling over many neurons (Zohary et al. 1994; Bair et al. 2001; Reich et al. 2001). Therefore, determining accurately the magnitude and structure of correlated variability is essential

to constrain coding models based on pooled firing rates (Abbott and Dayan 1999). Although some estimate near-zero correlated variability in V1 (Ecker et al. 2010, but see Cohen and Kohn 2011), our results agree with a small, nonuniform level of evoked correlated variability independent of firing rate and anesthetic state (Fig. 9).

Correlated variability of spontaneous activity was weakly de- pendent on distance (Fig. 8), consistent with other studies in rodent V1 (Ch'Ng and Reid 2010). The weakness of correlation observed in rodents, together with the lack of correlation from macaque V1 (Smith and Kohn 2008), suggests a source of variability during spontaneous activity that is uniform over V1. Only at the local level (pairs separated by <500 μm) was spontaneous correlated variability organized by difference in preferred orientation, reflecting the preferred orientation specificity of synchrony (Fig. 7) and synaptic connections (Ko et al. 2011).

Our results showed a significant dependence of evoked correlated variability on distance and a weaker dependence on orientation preference. We suggest that the sources of evoked correlated variability are organized by the functional architecture. We were able to correlate high evoked correlated variability with the presence of zero-spanning synchrony, but not offset synchrony (Fig. 10), suggesting that correlated variability is partially mediated by shared sources of synaptic excitatory input, but not local excitatory connectivity.

Synchrony and Coding

Regardless of the underlying functional connectivity, synchronous spikes are critical for driving postsynaptic cells in noisy synaptic environments in vivo. Synchronized input more effectively drives a postsynaptic neuron than nonsynchronized increases in firing rate (Bruno and Sakmann 2006). Enhanced effectiveness of synchronized spikes derives from supralinear summation of short interspike interval post-synaptic potentials (PSPs). In L4 of cat V1 in vivo, supralinear

summation of visually evoked excitatoty PSPs depends on the delay between excitation and inhibition within a window of 0–20 ms (Cardin et al. 2010a); elsewhere in sensory systems, sensitivity to coincidence requires intervals of <10 ms (Alonso et al. 1996; Roy and Alloway 2001; Kumbhani et al. 2007). Supralinear summation in vitro depends on Na^+ and Ca^{2+} dendritic conductances with a 0- to 30-ms effective summation interval (Nettleton and Spain 2000) and can overcome the strong synaptic depression in cortical cells (Bannister and Thomson 2006). Given firing rates of mouse V1 cells to artificial stimuli (<10 Hz), and other visual systems to natural stimuli (Vinje and Gallant 2000; Haider et al. 2010), summation within these intervals requires heterosynaptic summation through synchrony.

It has been proposed that representation of information in neuronal networks depends on synchrony. While pairwise analysis in the retina adds <10% to the information that can be extracted from independent responses (Nirenberg et al. 2001; Schneidman et al. 2003), higher-order correlations increase information by as much as 20% (Pillow et al. 2008). In the lateral geniculate nucleus, up to 20% additional information can be extracted from pairwise correlations (Dan et al. 1998). In V1, synchrony between pairs of cells can be used to better discriminate gratings with fine, but not course, orientation differences (Samonds et al. 2003, 2004), supporting a role for synchrony. It is not known if correlated spikes in the millisecond timescale are used by the brain to decode population activity, but these, and theoretical results (reviewed in Harris 2005), underscore the need for simultaneous recordings of multiple neurons and the identification of higher statistical dependencies (Nirenberg and Latham 2003; Schneidman et al. 2006; Pillow et al. 2008).

Our data show that about 8% of neuronal pairs fired synchronous spikes within a window of ±10 ms. This synchrony depends on distance and orientation preference. Because of stimulus limitations, clustering resolution, and low spike rates, our measurements represent a lower bound on the amount of synchrony among cortical cells and reinforce the notion that, to understand neural coding, neuronal responses should not be treated independently.

Figures
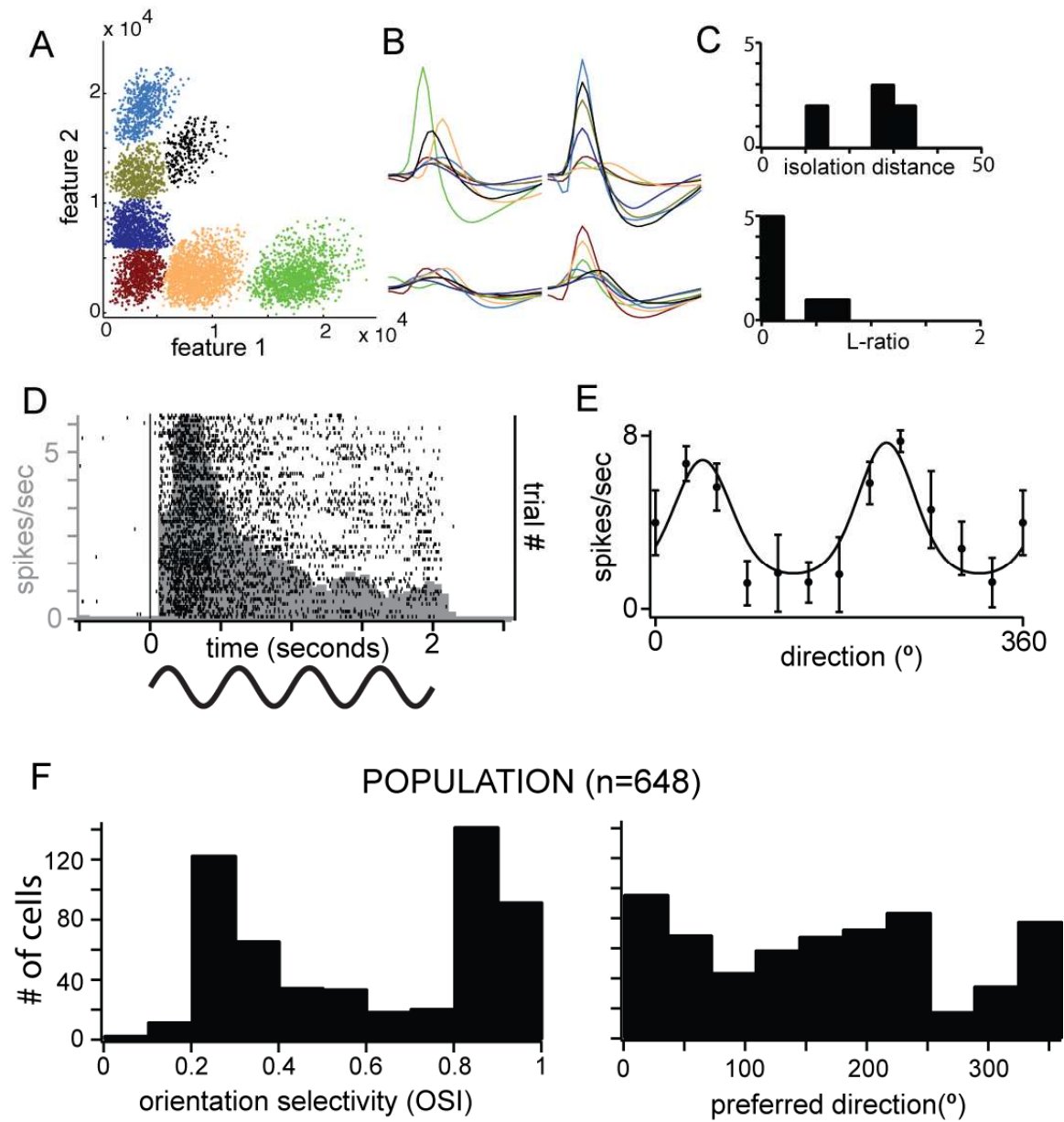
Figure 2.1. Characterization of simultaneously recorded small population in mouse V1.
(A and B) Example for the separation of spiking activity on a single tetrode into single-cell

clusters. (A) Spikes from the tetrode, plotted in feature space, and color-coded by cluster

assignment. Features 1 and 2 correspond to the waveform peak values on 2 contacts, shown in

the top row of B. Nonclustered spikes have been removed. (B) Average waveform values on each

contact for each cluster shown in A. (C) Spike cluster metrics, isolation distance, and L-ratio, from

the example data. (D and E) Representative response from a single cell in L2/3 of mouse V1. (D)

Peristimulus time histogram and (E) orientation tuning. (F) Orientation tuning parameters across

the population of recorded neurons. In this and all subsequent figures, error bars are standard

error of the mean.
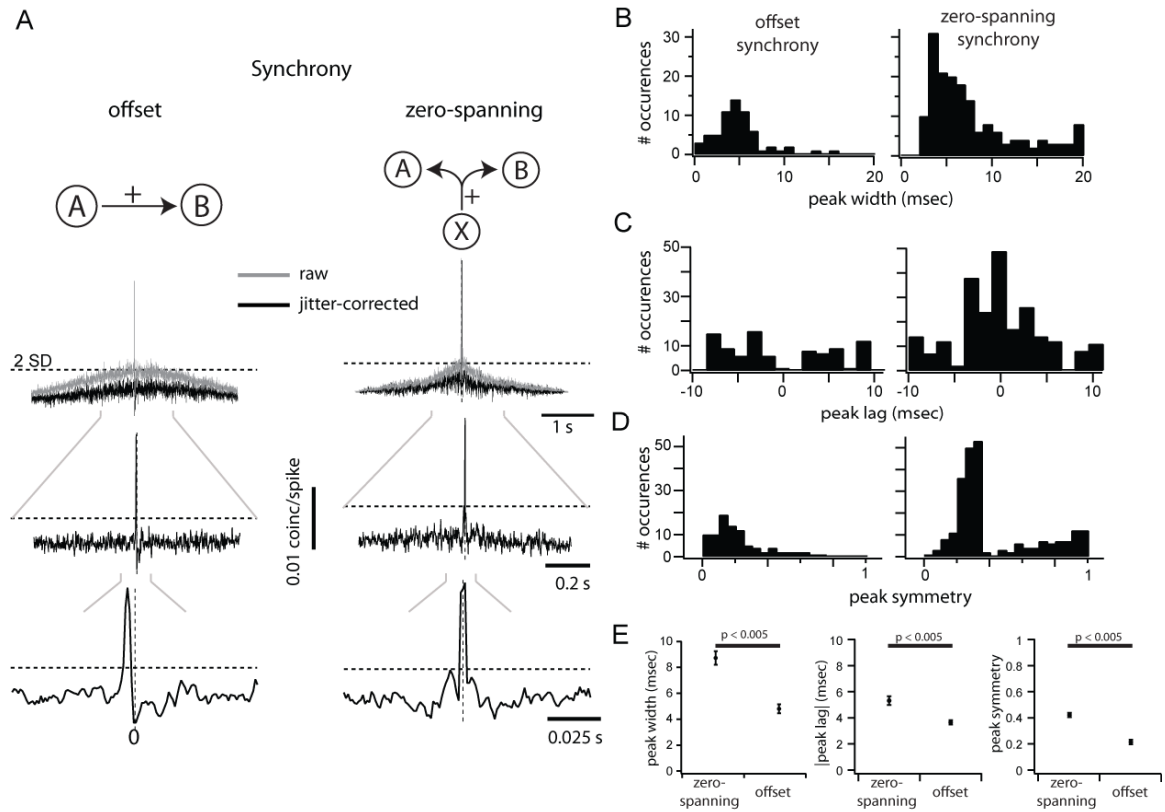
Figure 2.2. Quantification of pairwise correlation.
(A) Measuring and classifying synchrony from CCGs. Raw CCGs (gray) were corrected using a

50-ms jitter-correction term. A threshold (dashed lines) was set 2SD above mean in the 100- to

200-ms range of each CCG. Any peak above this threshold within 10 ms of zero was classified as

positive; positive peaks were classified as either offset if the entire peak was offset from zero (A,

left) or zero-spanning otherwise (A, right). (B) The distributions of peak widths for each CCG

class, where peak width is measured at the crossing of the significance threshold. (C) The

distributions of peak lag for each class of CCG, where peak lag is measured as the time of peak

relative to time zero. (D) The distributions of peak symmetry for each class of CCG, where peak

symmetry is measured as the magnitude of peak at time zero relative to the peak magnitude. (E)

Comparison of the mean peak width, absolute peak lag, and peak symmetry between CCG

classes.
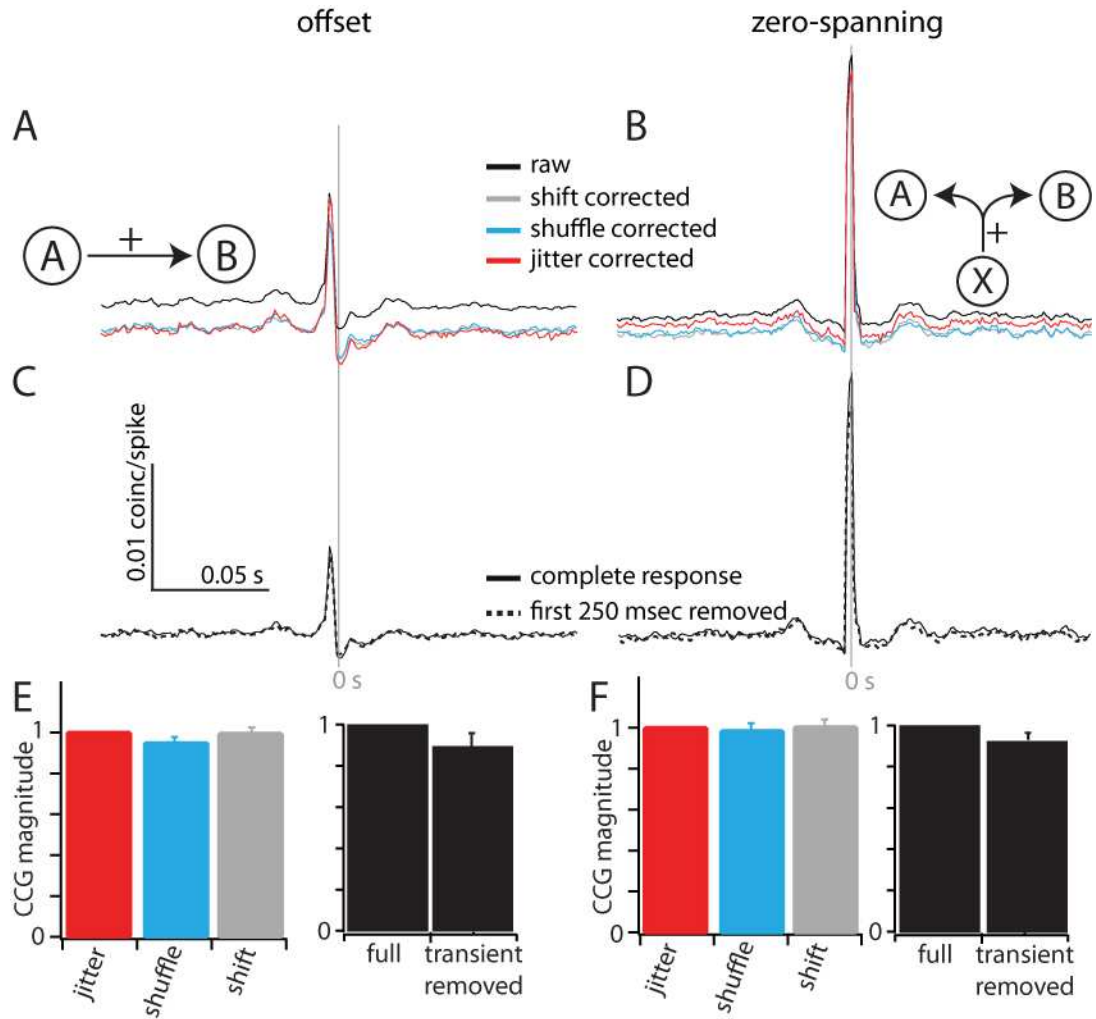
Figure 2.3. Examination of factors contributing to the measurement of synchrony magnitude. (A and B) Correction of raw correlograms using 3 correction techniques: Shift (gray line), shuffle (blue line), and jitter (red line), for offset (A) and zero-spanning (B) CCGs. (C and D) Removing onset transient did not affect CCG magnitude for offset (C) or zero-spanning (D) CCGs. (E and F) Population measures of each factor on CCG magnitude. For the correction method, each CCG is normalized to the magnitude of the jitter-corrected CCG (left). For transient removal, the transient-removed CCG is normalized to the height of the full-response CCG (right).
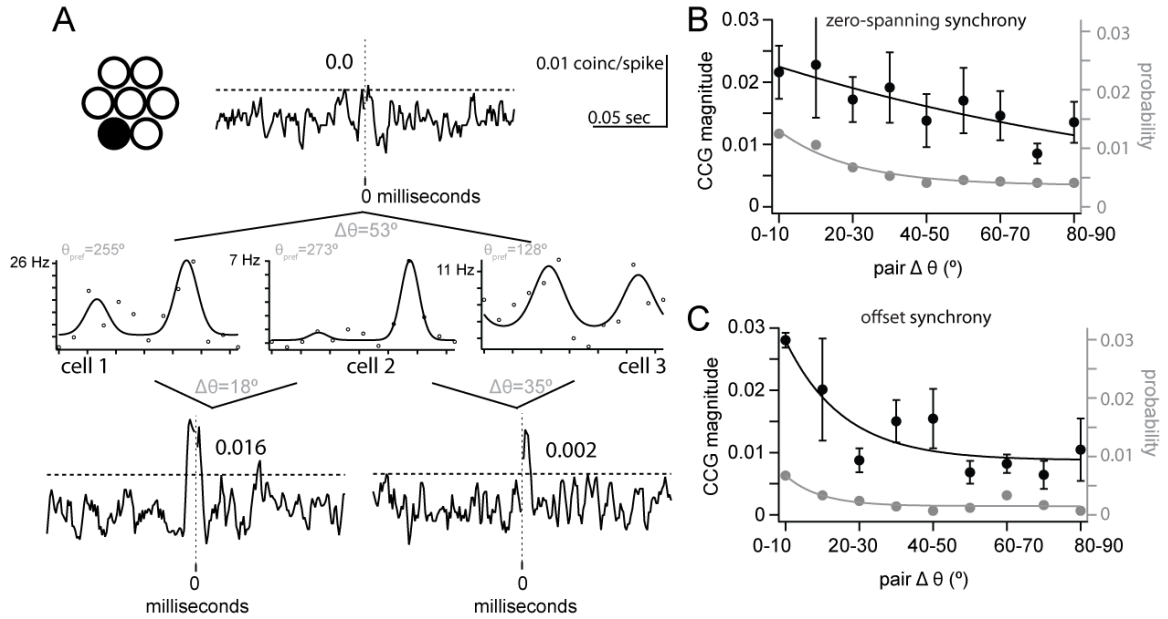
Figure 2.4. Synchrony is dependent on difference in the orientation preference.
(A) Example trio of simultaneously recorded pairs. The pair with the most divergent orientation

preferences showed no synchrony (top), while the magnitude of synchrony between the

remaining pairs was largest for the aligned pair (bottom). (B) The magnitude and probability of

zero-spanning synchrony depended exponentially on difference in the orientation preference. (C)

The magnitude and probability of offset synchrony depended exponentially on difference in the

orientation preference.
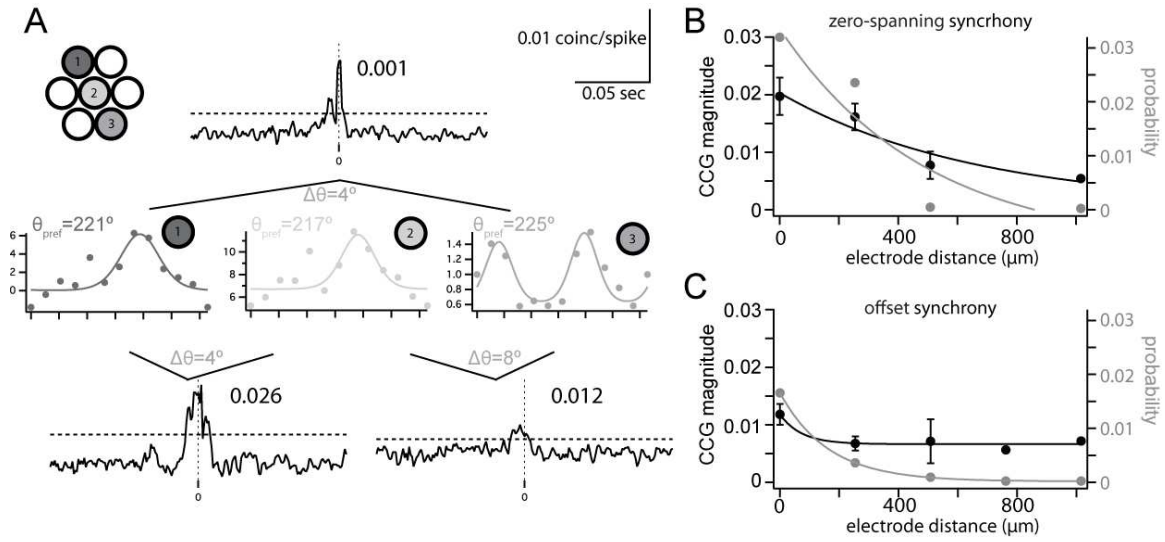
Figure 2.5. Synchrony is dependent on distance between a pair of cells.
(A) Example trio of simultaneously recorded pairs. The pair with the largest electrode separation

showed weak synchrony (top), while the closer pairs showed stronger synchrony. (B) The

magnitude and probability of zero-spanning synchrony depended exponentially on pair distance.

(C) The magnitude and probability of offset synchrony depended exponentially on pair distance.
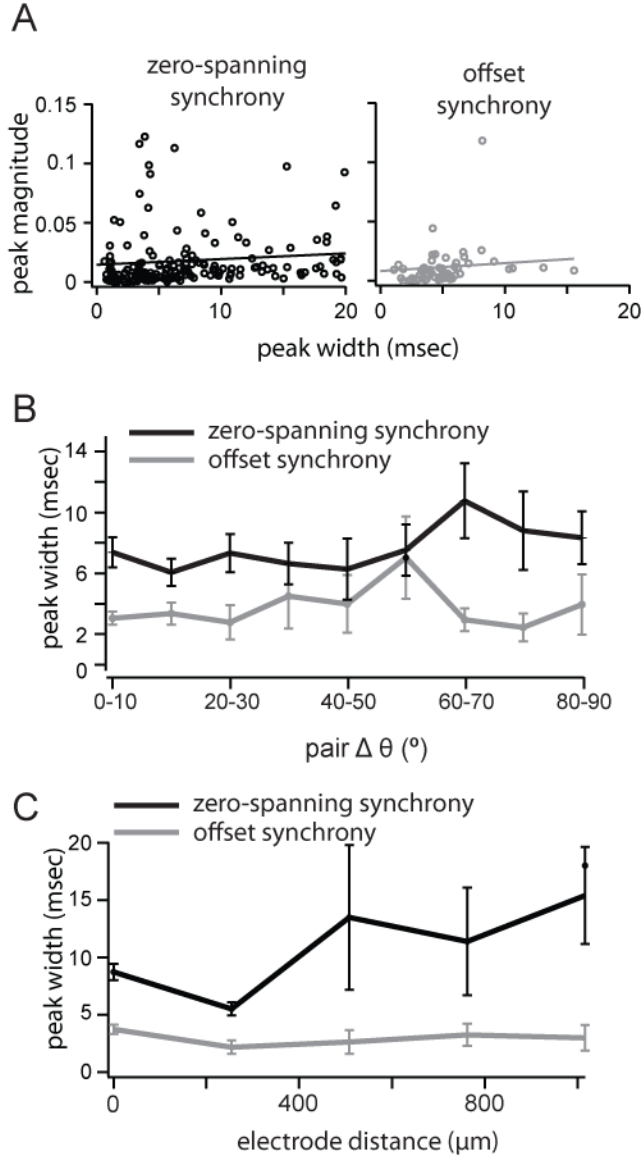
Figure 2.6. Offset synchrony width is narrower than zero-spanning synchrony.
(A) Cross-correlation magnitude measured as a function of peak width for zero-spanning (black, left) and direct synchrony (gray, right). (B) Width of CCG peaks, measured at the threshold crossing, as a function of distance between cells for offset (gray trace) and zero-spanning synchrony (black trace). (C) The width of CCG peaks as a function difference in preferred orientation for offset (gray trace) and zero-spanning synchrony (black trace).
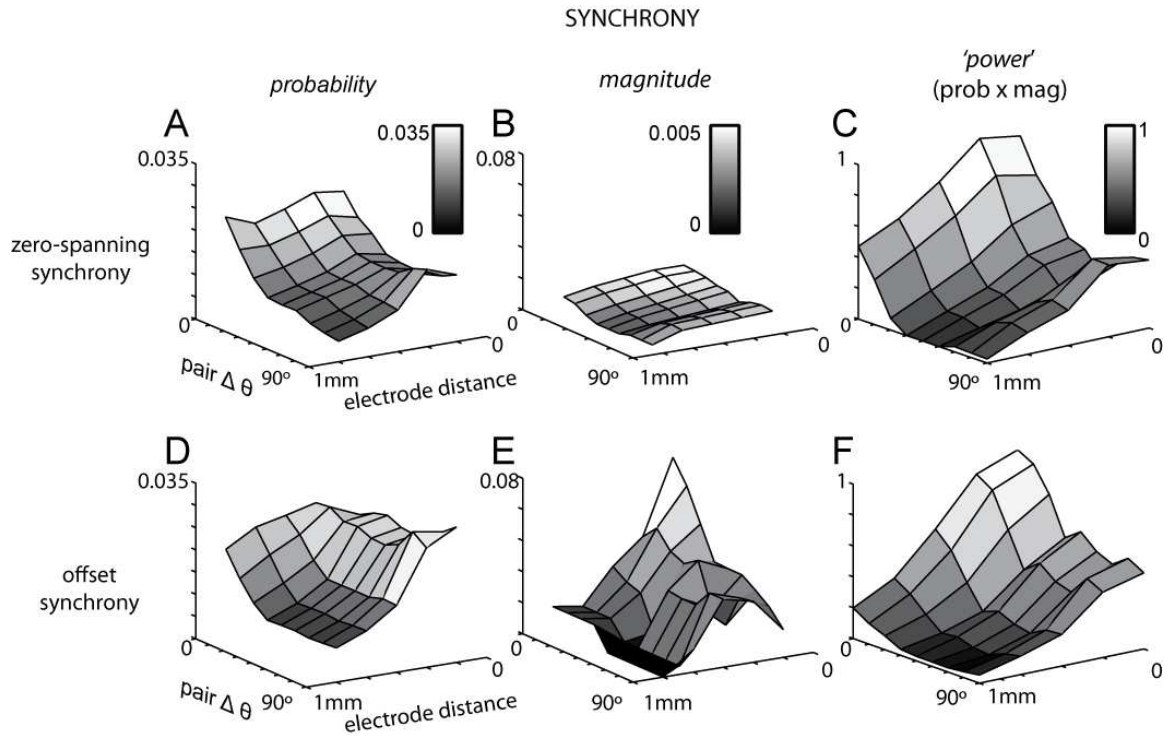
Figure 2.7. The structure of synchrony across distance and orientation preference.
(A–C) Zero-spanning synchrony depends on distance and Δθ. Probability (A), magnitude (B), and

synchrony power (C) decayed exponentially from nearby, closely aligned pairs. (D–F) Offset

synchrony depends on distance and Δθ. The probability of direct synchrony (D) was independent

of Δθ for nearby pairs, but dependent on Δθ at greater distances. Magnitude (E) was dependent

on Δθ at all distances, and synchrony power (F) decayed exponentially from nearby, closely

aligned pairs.
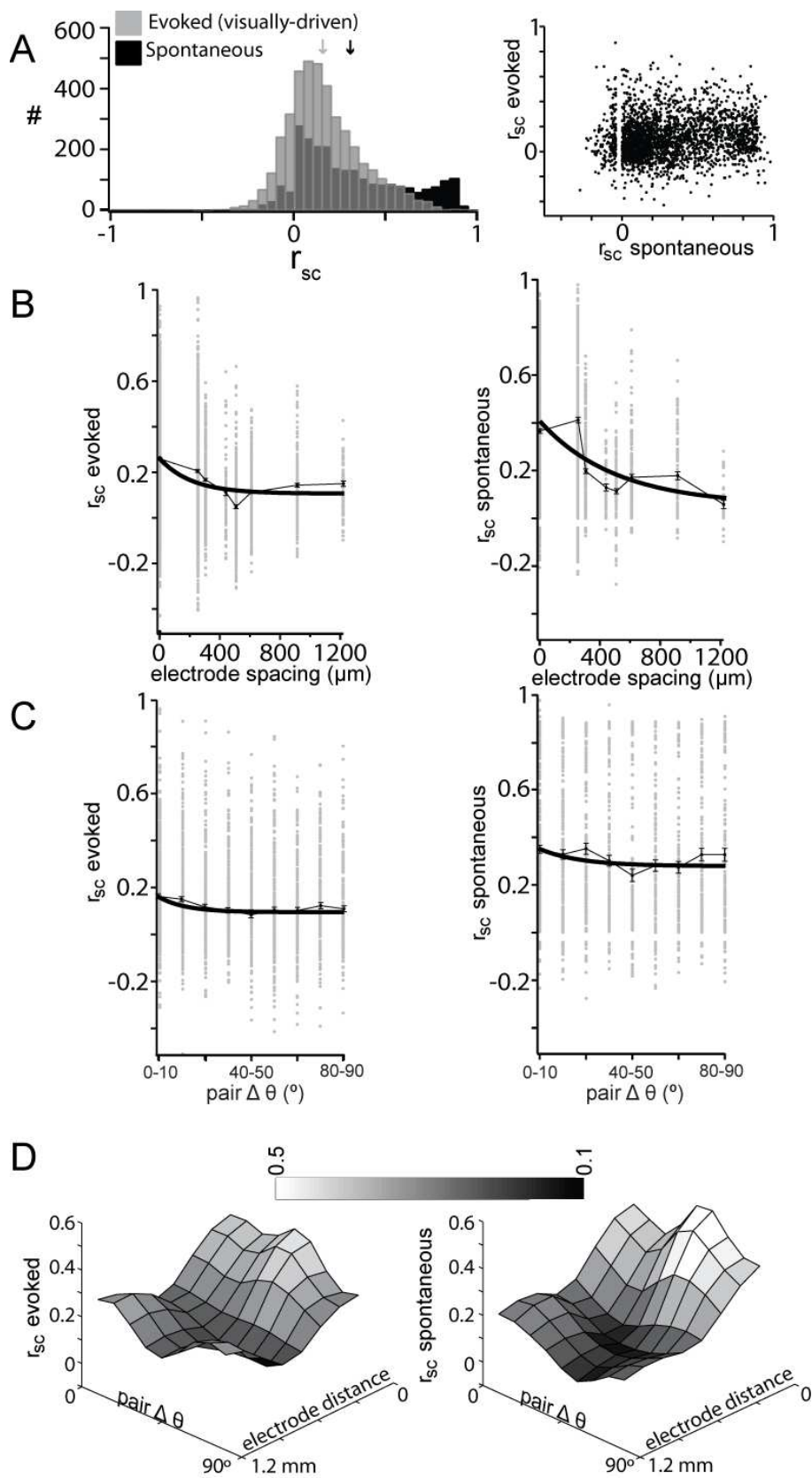
Figure 2.8. The structure of correlated variability across distance and orientation preference.
(A) Distributions of evoked (gray) and spontaneous (black) r_{SC} were nonzero (left). Evoked r_{SC} was positively correlated with spontaneous r_{SC} (right). (B) Evoked and spontaneous, r_{SC}, decayed with distance between a pair of cells. (C) Evoked and spontaneous, r_{SC}, was dependent on the difference in orientation preference between a pair of cells. (D) Spontaneous and evoked, r_{SC}, have a stronger dependence on $\Delta\theta$ at smaller distances.
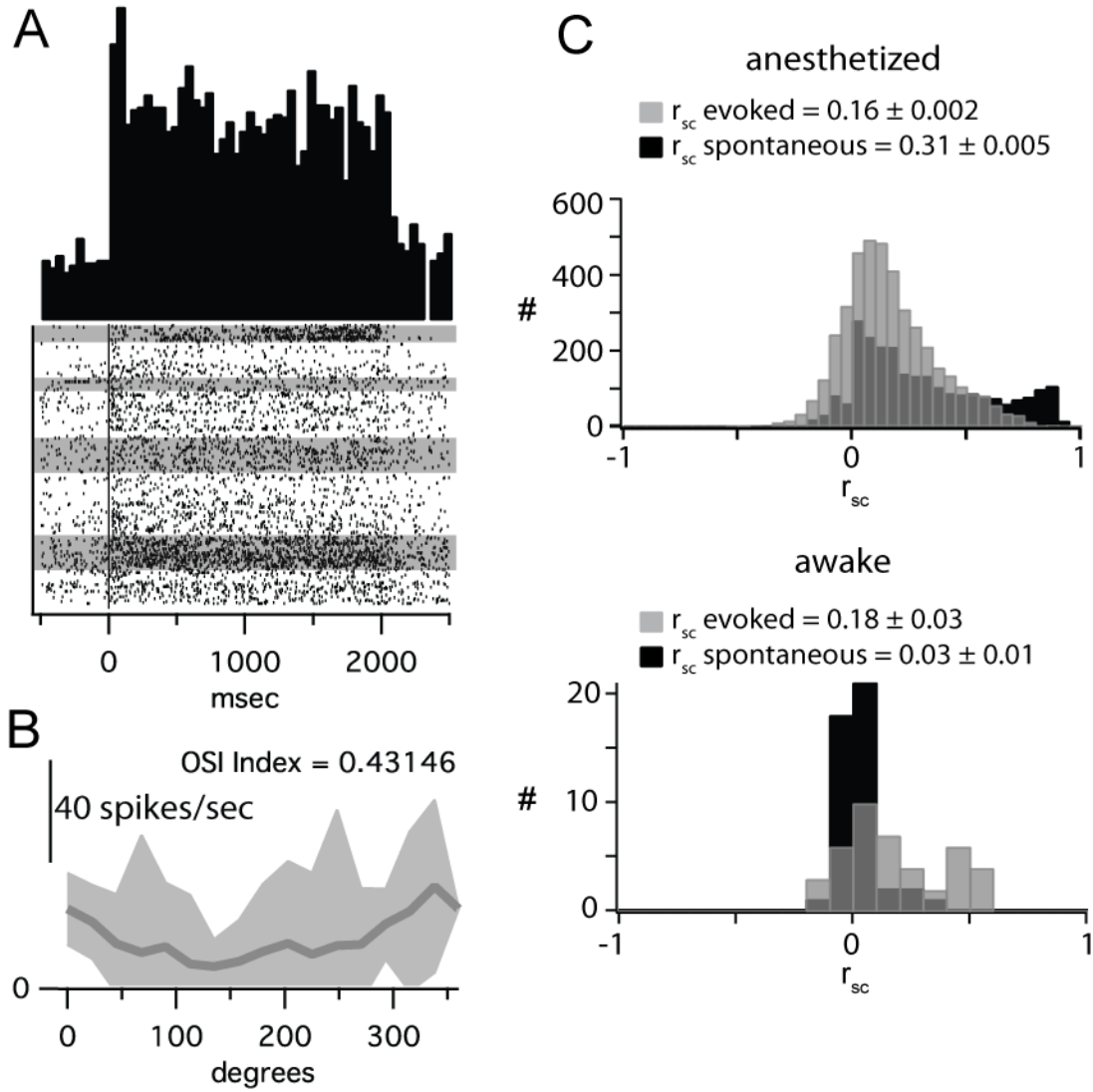
Figure 2.9. r_SC is not affected by anesthetic state.
(A) PSTH and spike rasters from a single unit recorded from V1 of an awake, head-fixed mouse.

Gray shading of spike rasters indicates epochs of locomotion. (B) Orientation tuning of cell in A.

(C) The distributions of evoked r_SC were the same in anesthetized (top) and awake (bottom)

states, while that of spontaneous r_SC were higher in the anesthetized (top) than awake (bottom)

states.
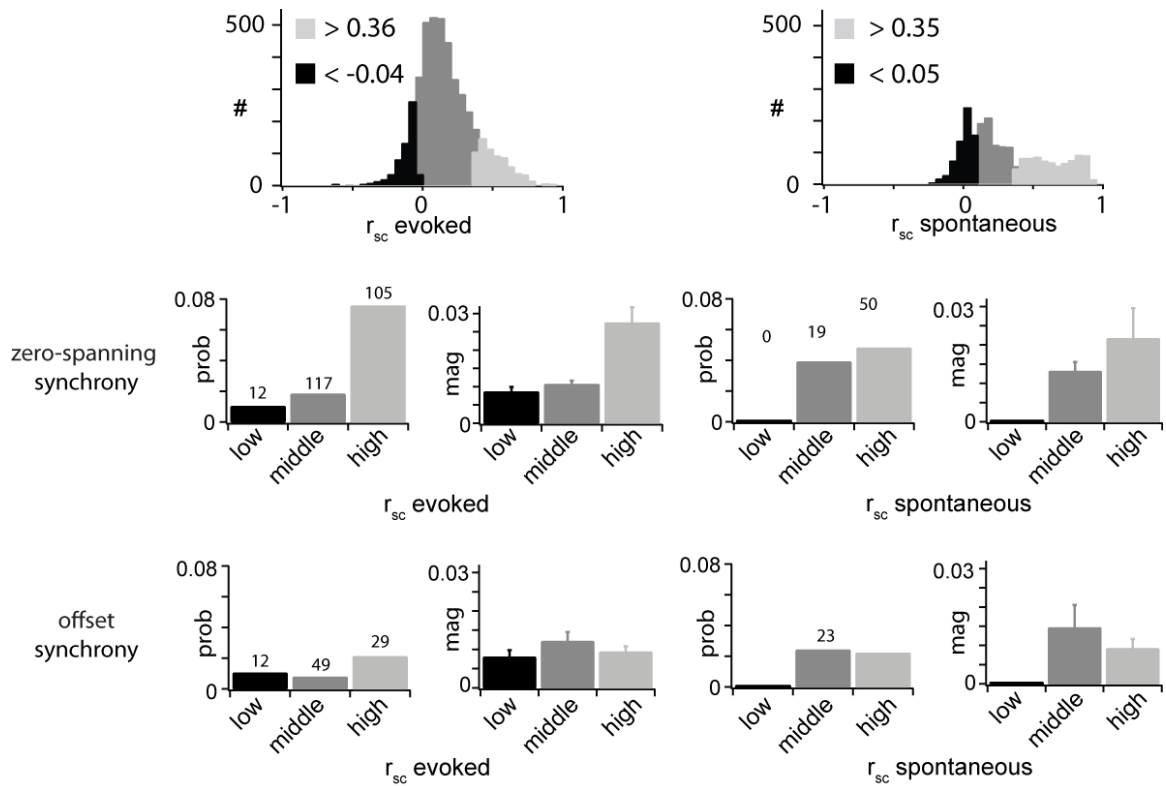
Figure 2.10. r_{SC} is correlated with zero spanning, but not offset synchrony.
 (A and B) Each pair was classified as high, mid, or low r_{SC}, for both evoked (A) and spontaneous

(B) correlated variabilities, based on the total distribution of r_{SC} values (top). (C) Pairs with high

evoked r_{SC} had a higher probability of having zero-spanning synchrony. Pairs with high evoked

r_{SC} had a larger magnitude of zero-spanning synchrony. (D) Level of r_{SC}, either spontaneous or

evoked, did not affect either the probability or magnitude of offset synchrony.
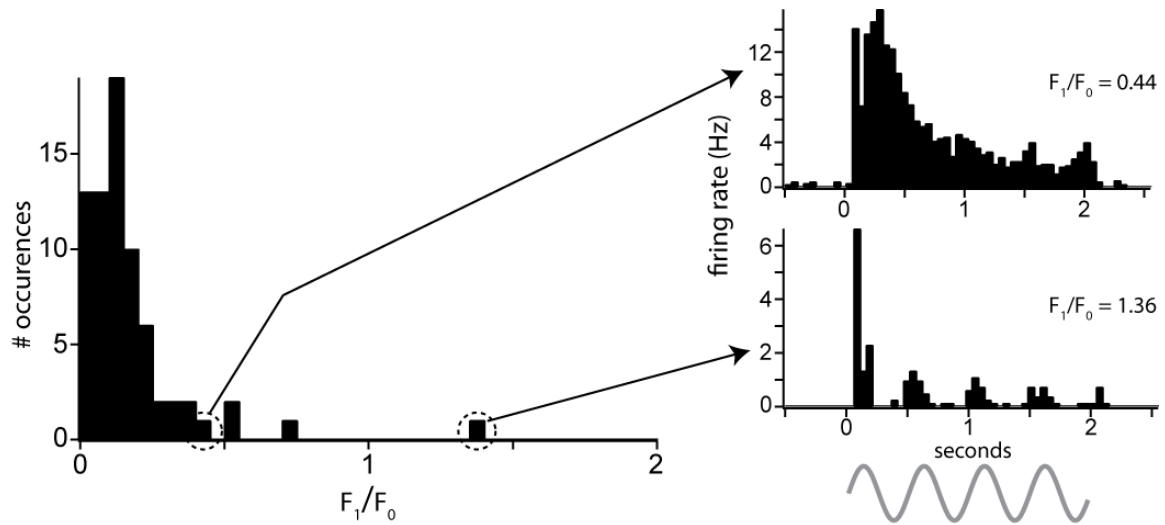
Figure 2.11. Distribution of simple and complex cells in the population of layer 2/3 neurons.
The distribution of F1/F0 values from a representative set of simultaneously recorded layer

neurons responding to a drifting sinusoidal grating. One cell [bottom right] had an F1/F0 ratio

greater than one, indicating a simple-like modulating response at the temporal frequency of the

grating. All other cells had a complex cell-like non-modulating response to the drifting grating [top

right]. Recording depth: 325 μm from the surface of the cortex.
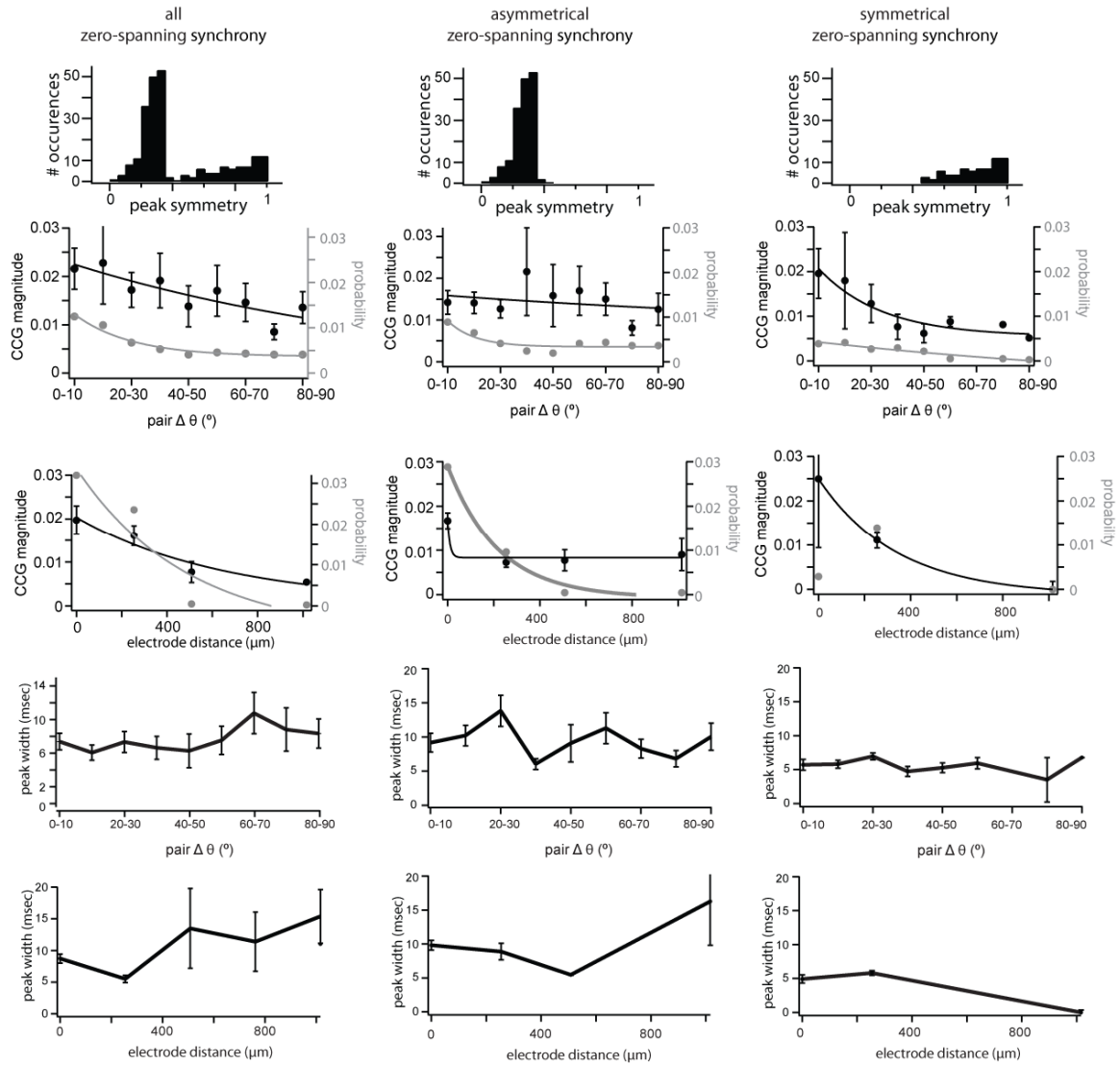
Figure 2.12. Stimulus-induced correlations do not affect measured synchrony.
A, The method of correction for correlation induced by the drifting of the stimulus does not affect

the size or shape of synchronous peak for either direct or feedforward synchrony. Raw

correlograms [black traces] are corrected using a trial-shift correction method [grey traces], trial

shuffle method [blue traces], or spike train jittering method [red traces]. *B,C,* removing the first

250 milliseconds of each response, to eliminate correlations during the onset transient, reduced

but did not eliminate either form of correlation.
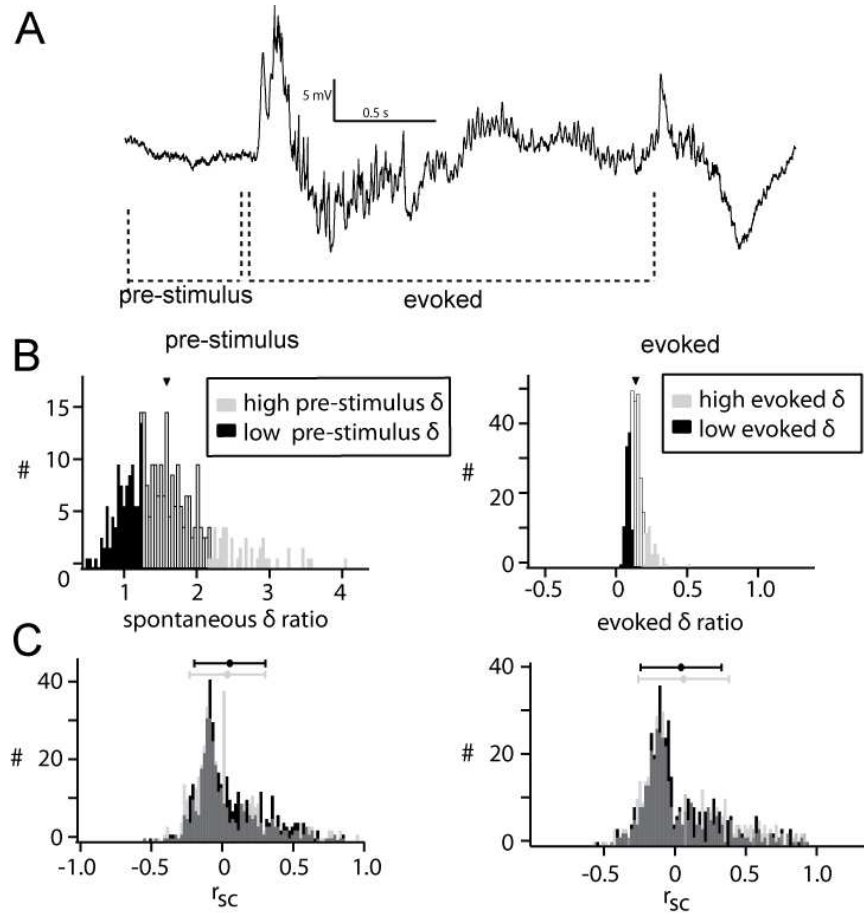
Figure 2.13. Network oscillations do not affect magnitude of correlated variability.
A, Network state preceding and during each stimulus presentation was determined based on the spectral content of simultaneously recorded local field potentials (LFPs) by appling a fast Fourier transform (FFT) to LFP segments (0.5 s). *B,* The ratio between 20-70 Hz and 1-7 Hz bands (gamma [γ] ratio) was to describe the state of the network. The spontaneous state of the network was classified, according to the distribution of gamma ratios, as "high" (values above 1SD, light gray, mean indicated by arrow head) and "low" (values below 1SD, black). *C,* Correlated variability was not different between the two state extremes, nor was the r_{sc} for either state different that the r_{sc} measured across all states.

55

CHAPTER 3: SPECIFIC CORTICAL LAYER 6 THALAMIC PROJECTIONS MODIFY THE BALANCE OF INHIBITION AND EXCITATION IN MOUSE DORSAL LATERAL GENICUALTE NUCLEUS

Abstract

Understanding the role of corticothalamic projections in shaping visual response properties in the thalamus has been a longstanding challenge in visual neuroscience. Here, we take advantage of the cell-type specificity of a transgenic mouse line, the GN220-Ntsr1 Cre line, to selectively manipulate the activity of a layer 6 corticogeniculate (CG) population while recording visual responses in the dorsal lateral geniculate nucleus (dLGN). We manipulate Ntsr1 cell activity primarily by hyperpolarizing using archaerhodopsin-3, but also investigate the effect of stimulating these cells with channelrhodopsin-2. We find that removing Ntsr1 projections resulted in both increases and decreases in visually-evoked spike count, even in simultaneously recorded cells. The effect is contrast dependent, and the sign is consistent over the full range of contrasts. Tuning properties suggest wide convergence of Ntsr1 cells with similar spatial and temporal frequency tuning onto single dLGN cells. We do not find evidence that Ntsr1-CG cells sharpen spatial tuning properties or improve temporal fidelity. Finally, pairwise analysis shows that Ntsr1 cells can affect retinal transfer, in a way consistent with and predicted by the effects on single cells.

Introduction

In most sensory modalities, primary sensory thalamus is the locus of transfer from the sensory periphery to cortex (Jones, 2007). Reciprocal projections from primary sensory cortex to thalamus are in a position to shape this transfer. Corticothalamic (CT) axons make excitatory synaptic connections with thalamic relay cells, thalamic interneurons, and inhibitory, thalamus-projecting neurons in the reticular nucleus (RE) (Bourassa and Deschenes, 1995; Zhang and Deschenes, 1997). CT projections form distal synapses onto relay cells that utilize metabotropic glutatate receptors (McCormick and von Krosigk, 1992) and inhibitory synapses on RE and local interneurons (REF). Thus, CT projections are position to provide a mix of excitation and inhibition to relay cells, with potentially divergent effects on thalamic spiking activity. Indeed, many studies have concluded that the cortical influence on thalamus is facilitatory (Przybyszewski et al, 2000), suppressive (Andolina et al., 2007), or both (Kalil and Chase, 1970; Molotchnikoff and Lachapelle, 1977; McClurkin et al., 1994), while still others see minimal effects on responses (Richard et al., 1975; Baker and Malpeli, 1977),

Reciprocal CT projections originate in cortical layer 6 (L6), from thalamorecipient neurons that have an apical dendrite extending to cortical layer 4 (L4) and a bifurcating axon that terminates in both L4 and the thalamus (Tombol, 1984; Zhang and Deschenes, 1997; Zarrinpar and Callaway, 2006; Briggs, 2010; Thomson, 2010). In L6, CT cells are intermixed with claustrum-projecting, pulvinar-projecting, cortical-projecting and local cortical neurons (Zarrinpar and Callaway, 2006) reviewed in (Briggs, 2010; Thomson, 2010). Specifically accessing the sensory thalamus-projecting population of CT cells, here called corticogeniculate (CG) cells, is challenging. Because of this anatomy, techniques for manipulating CG activity have usually included all cortical activity (Vastola, 1967; Hull, 1968; Baker and Malpeli, 1977; Sillito et al., 1994; de Labra et al., 2007). Using these techniques in the visual system, investigations of the effect of CG axons on thalamic activity have yielded potential roles for CG projections in gain control (Przybyszewski et al, 2000), responsiveness to high-velocity stimuli (Gulyas et al., 1990),

sharpening of dLGN receptive fields (Marrocco and McClurkin, 1985; Andolina et al., 2013) and in increasing reliability and precision of spike timing (Worgotter et al., 1998; Andolina et al., 2007).

Transgenic approaches allow for manipulation of genetically-specified populations of neurons and have facilitated investigation of the role of layer 6 CG neurons (Olsen et al., 2012). The bidirectional modification of CG cell activity with millisecond resolution, via optogenetics, could yield new insight into the function of CG feedback. Here, we utilize the Gn220 Ntsr1-Cre line to investigate the effect of these cells on dLGN responses. Ntsr1-Cre corticogeniculate cells (Ntsr1-CG) are comprised of layer 6 pyramidal cells with two morphologies, both of which project to dLGN (Gong et al., 2007; Gong et al., 2012). We find that removing only Ntsr1-CG projections was capable of driving both increases and decreases in visually-evoked spike count, even in simultaneously recorded cells. The effect is contrast dependent and consistent over the full range of contrasts. Tuning properties suggest wide convergence of Ntsr1-CG cells with similar spatial and temporal frequency tuning onto single dLGN cells. We do not find evidence that Ntsr1-CG cells sharpen spatial tuning properties or improve temporal fidelity. Finally, pairwise analysis shows that Ntsr1-CG cells can affect retinal transfer, in a way consistent with and predicted by the effects on single cells.

Materials and Methods

All procedures were approved by the University of Pennsylvania Institutional Animal Care and Use Committee using adult GN220 Ntsr1-Cre mice originally generated by the GENSAT project (Gong et al., 2007).

Expression of opsins

To achieve specific expression of microbial opsins in Ntsr1-CG cells, we used an adeno-associated viral (AAV) delivery system and the FLEX switch (Atasoy et al., 2008) to limit expression to Cre+ cells (Cardin et al., 2010b). Briefly, animals were anesthetized with 2% inhaled isoflurane and placed in the stereotactic apparatus. A burrhole craniotomy was made over primary visual cortex (V1). A Hamilton syringe with a 33-gauge beveled opening needle controlled by a Quintessential Stereotactic Injector (Stoelting Co., IL, USA) was inserted into V1 to a tip-depth of 900 μm. Following a 10 minute rest period, 300-1000 μL of AAV (serotype: 2/9, prepared by the University of Pennsylvania Vector Core) was injected at a rate of 30 μL/min. Following another 10 minutes rest period, the syringe was retracted, burrhole filled with bone wax, and skin sutured. At least two weeks elapsed before acute recording to allow for maximal opsin expression.

Acute Experiment Preparation

All data were collected during acute recording sessions. Animals were anesthetized with 2% inhaled isoflurane and placed in the stereotactic apparatus. Temperature was maintained at 37⁰C via feedback to a heating pad from a rectal thermometer and eye moisture maintained via transparent lubricant. A cranial window was opened over dLGN and visual cortex. An array of independently positionable tetrodes (Thomas Recording GmbH, Germany) was lowered into

cortex above dLGN and a laser-coupled optical fiber positioned on the cortical surface above V1. Each tetrode was lowered individually; placement in dLGN was assessed by strong multi-unit spike modulation to a spatially uniform flashed stimulus. Because layer 6 cortical activity can be sensitive to many anesthetic regimes (Angel and LeBeau, 1992; Briggs and Usrey, 2008), once tetrodes were positioned isoflurane concentration was lowered (~1.2%) and continuously adjusted based on the synchrony of the local field potential activity. This ensured a cortical state with relatively little slow oscillation in order to facilitate L6 responsiveness.

Stimulation and Acquisition

Spike data were acquired at 30.303 kHz, filtered between 600-6000 Hz, and a threshold was manually set on each channel. Crossing of this threshold triggered acquisition of the spike waveform on all four tetrode channels.

Visual stimuli were generated using the ViSaGe stimulus generation hardware (Cambridge Research Systems (CRS), Cambridge, UK) and a custom software package utilizing the CRS-provided MATLAB toolbox. Stimuli were presented on a 19-inch cathode ray tube monitor configured to refresh at 100 Hz with 600 X 800 resolution. The monitor was placed 30 cm from the eye and the position in the animal's visual field was adjusted in an attempt to maximize the evoked activity from a single recording site. Drifting grating stimuli subtended a total of ~70º of visual space and were presented with at least 1 second of mean luminance between each stimulus. Ternary noise stimuli contained 12 x 16 square pixels with an edge length of 3.3 degrees. Each frame was independent of the previous, and frames changed at a rate of 50Hz. The spatially-uniform flicker stimulus was designed following (Reinagel and Reid, 2002; Kumbhani et al., 2007), modified here to draw the contrast value randomly from an even distribution. The stimulus was updated at 50 Hz and a 5 second sample was repeated 100 times for each condition.

Laser illumination was performed using either a 200W, 532 nm solid state laser (for Arch activation) or 100W, 473 nM laser (for ChR2 activation) (OptoEngine LLC, Midvale, UT) coupled to a bare 200 μm, 0.62NA optical fiber. We chose a higher NA aperture fiber in order to maximize the horizontal spread of our laser illumination to achieve maximal coverage of V1 during the optogenetic manipulation.

Analysis

Spike waveforms were clustered offline using a mixture of an initial algorithmic (KlustaKwik) sorting followed by manual refinement using SpikeSort 3D (Neuralynx, Bozeman, MT), as described previously (Denman and Contreras, 2013).

Spike counts were made over the period during which the stimulus (drifting grating, ternary noise, or flicker) was present on the display, plus 200 msec to include any offset transients. The Ntsr1-CG effect was measured as the normalized difference between control and laser (Arch or ChR2) activated conditions:

$$Nstr1 - CT\ effect\ = \frac{N_{laser} - N_{control}}{N_{control}}$$

where N_{laser} is the spike count during Ntsr1-CG cell manipulation and $N_{control}$ is spike count during control conditions.

Contrast response functions (CRFs) were measured using the F1 component as the measure of each dLGN unit's spiking response, or as normalized Ntsr1-CG effect (see above) as a function of contrast. CRFs were fit with a hyperbolic ratio function, as in Contreras and Palmer, 2003:

$$f(C) = R_0 + R_{max} * \left(\frac{C^n}{(C_{50}{}^n + C^n)} \right)$$

where R_0 is an offset, R_{max} is the amplitude, C_{50} is the inflection point, and n controls the slope of the fit.

The orientation tuning curves, across the range 0-360°, were fit with the von Mises function (Swindale, 1998):

$$f(\theta) = b_0 + b_1 e^{K(\cos(\theta - \mu) - 1)} + b_2 e^{K(\cos(\theta - \mu + \pi) - 1)}$$

where b_0 is an offset for the baseline firing rate, b_1 and b_2 independently determine the size of each peak, K is the width parameter, and μ the preferred orientation. Orientation selectivity index (OSI) was calculated, from raw responses, as the difference between responses at preferred and orthogonal orientations as follows:

$$OSI = \frac{R_{preferred} - R_{ortho}}{R_{preferred} + R_{ortho}}$$

where $R_{preferred}$ is the response at the preferred orientation, as determined by the circular Gaussian fit, and R_{ortho} is the response at the orientation 90° from $R_{preferred}$.

Spatial and temporal frequency tuning curves were generated from spike counts, and both fit with the same function, from Gao et al., 2010:

$$f(x) = B + A e^{\frac{-1}{2s^2} * log\left(\frac{x + O}{p + O}\right)^2}$$

where B is an offset for the baseline firing rate, A is the amplitude, s is the standard deviation, O is the log offset, and p the preferred spatial or temporal frequency.

Spatial receptive fields were fit with a two-dimensional Gaussian function:

$$f(x, y) = A e^{\left[\frac{-1}{2(1 - cor^2)} \left(\left(\frac{x - x_0}{xWidth}\right)^2 + \left(\frac{y - y_0}{yWidth}\right)^2 - \frac{2 * cor * (x - x_0)(y - y_0)}{xWidth * yWidth} \right) \right]}$$

with a center point chosen based on the pixel with maximal absolute deviation and the fit performed on the frame included this pixel. Frames computed at 10 msec intervals ($\Delta\tau = 10$ msec). Although the receptive fields were mostly symmetrical, we allowed the x and y parameters to be independent to get the best possible fits.

Flicker analysis was performed following Kumbhani et al. (2007). Briefly, histograms of the unit response to flicker stimulus were generated at 100 µsec resolution. Individual events were identified by smoothing thes histograms with a 10 msec box filter, threshholding, and finding the center of each excursion above the threshold. These event times were used to extract peri-event responses from raw non-smoothed histograms; peri-event responses were fit with a Gaussian function to parameterize event height and width. Event Fano factor was measured as the mean of squared variance in spike count divided mean spike count. Event reliability was measured by taking the average inner product of each trial, after each trial was converted to a binarized vector the length of the noise sequence, with 1 representing a spike in that bin and 0 no spike in that bin. Finally, mutual information in each cell's response about the stimulus sequence was estimated by considering the total number of possible contrast sequences, given the number of contrasts we used and a random generation and the reduction in uncertainty given the cell's response.

Results

We investigated the role of corticogeniculate projections in dLGN neuron visual responses using the GN220 Ntsr1-Cre transgenic mouse created by the GENSAT project (Gong et al., 2007). To gain fast, reversible inactivation of corticogeniculate neurons, we introduced GFP-Archaerhosopsin-3 (Arch) using a FLEX expression system (Atasoy et al., 2008; Chow et al., 2010) via intracranial injection of an adeno-associated virus (AAV) (Cardin et al., 2010b). In a subset of experiments, we also introduced a FLEXed mCherry-Channelrhodopsin-2 (ChR2) to specifically activate Ntsr1-CG cells (see Materials and Methods). Expression of opsins was limited to corticothalamic neurons (Fig. 1A), which we will refer from here on as Ntsr1 cells. Expression of Arch following viral injections was extensive, covering all of V1; somatic expression was restricted to the lower layers of V1 and robust expression of Arch can be seen in axonal terminals in LGN and reticular nucleus (RE, Fig. 1A). Ntsr1 cells were limited to layer 6 (Fig 1A); neurites expressing the fluorescent reporter extended to layer 4 and densely ramified, and a subset also extended to, and ramified in, layer 1 (Fig 1A). We also observed axonal projections from Nstr1 cells to the lateral dorsal nucleus (LD) and lateral posterior nucleus (LP) of the thalamus. In target structures, as well as cortical layer 4, the density of neurites was such that gaps in fluorescence that shape somas were observable.

To record visually-evoked spiking activity from small populations of neurons in dorsal lateral geniculate nucleus (dLGN) and primary visual cortex (V1), we used arrays of independently movable tetrodes. To control the Arch proton pump, we coupled a green (532 nm) laser into an optical fiber positioned on the cortical surface; output wattage from the fiber tip was measured to be 50mW/mm2. In recordings of small groups of cells in L6, spontaneous activity of a subset of units (28%) was hyperpolarized by 532-nm light illuminating V1, while other nearby units were not directly affected (Fig. 1B). Hyperpolarization of Ntsr1 cells effectively eliminated visually-evoked activity, even at preferred orientations (Fig 1C, control in gray, during illumination

with green laser in green). We first investigated the effect of Nstr1 cell projections on LGN spike counts evoked with drifting sinusoidal gratings.

Effect of Ntsr1 corticogeniculate cell activity on dLGN spike count.

V1 has been shown to both enhance (Tsumoto et al., 1978; McClurkin et al., 1994, Przybyszewski et al., 2000), suppress (Tsumoto et al., 1978; McClurkin et al., 1994; Andolina et al., 2007, 2013), or have little effect on dLGN visually evoked activity (Richard et al., 1975; Baker and Malpeli, 1977). We assessed the effect of specifically removing Ntsr1 cell input on the dLGN spike output evoked by a highly effective stimulus: high contrast drifting sinusoidal gratings with spatial and temporal frequencies optimized to drive mouse dLGN units (0.08 cyc/deg, 3 deg/s). On half of the trials, randomly interleaved, corticogeniculate Ntsr1 cells were hyperpolarized by illuminating the cortex with a green laser that activates Arch. We will refer to responses during laser illumination as "+Arch". Single dLGN units responded in both conditions with a temporally modulated firing output at the frequency of the grating. We quantified visual responses by the mean firing rate (the DC component) and the amplitude of the fundamental harmonic (the F1 component).

Removing corticogeniculate input resulted in a range of effects on single dLGN unit visual responses (Fig. 2). The single LGN unit in Fig 2A (average tetrode waveforms shown above) showed robust output to the drifting grating (represented above rasters), both during control conditions (black rasters, black PSTH below) and +Arch (green rasters, green PSTH below). This cell exemplifies the group of dLGN units that showed no changes in visual response in the absence of Ntsr1 input (DC: 14.3±2.2 Hz, 12.4±2.0 Hz +Arch; F1: 13.6 Hz, 12.3 Hz +Arch). In contrast, the unit in Fig. 2B is an example of cell that showed an increase in response in the absence of Ntsr1 corticogeniculate input, in this case, a 42% increase in response (DC: 4.5 Hz control; 6.4 Hz +Arch). Finally, the single dLGN unit in Fig. 2C showed a 15% decrease in visual

response in absence of Ntsr1 input (DC: 4.9 Hz in control; 3.7 Hz +Arch; F1: 4.1 Hz in control; 3.5 Hz +Arch). We plotted the DC (Fig. 2D, 0-10 spks/sec range expanded at right) and F1 (Fig. 2E, 0-5 spks/sec expanded at right) of the response of all LGN units before and during hyperpolarization of Ntsr1 cells (+ Arch). The main effect of removing Ntsr1 input in spike output was a modest change in response magnitude with a tendency for an increase in the visual response (DC) compared to control. The change in response DC (ΔDC) was larger than that of response F1 (ΔF1, Fig. 2H).

To summarize effect of removing Ntsr1 cell input, we calculated the ratio between the response DC in control conditions and +Arch for each unit. The distribution of response ratios (Fig. 2F) had a mean of 1.24 ±0.05 and a median of 1.09. The distribution shows that the visual response of 38% (n = 46/122) of LGN units had no contribution from Ntsr1 corticogeniculate cells, since removing their input had no effect (0.9 < response ratio < 1.1, Fig. 2F, vertical lines). In contrast, in 21% (n=26/122) of LGN units Ntsr1 input increased visual responses, since removing that input decreased response DC (minimum = 0.28). Finally, in 41% of LGN units Ntsr1 input suppressed visual responses, since its removal led to increased response DC (maximum = 3.86). Noticeably, a small population had ratios centered around 2, which shows that for some dLGN units cortical input reduces by half the visual response in control conditions.

The distribution of response ratio could be biased by very low or very high firing rates of dLGN units during control visual responses. Cells with high control firing rates could show small response ratios even for important effects of removing Ntsr1 input. Conversely, cells with low control firing rates could show very large response ratios for even for small effects of Arch. To verify whether such bias was present in our data, we plotted the numerator against the response ratio for all cells. The control firing rate (Fig. 2G, numerator) showed the same shape as the response ratio distribution, indicating that our distribution was not biased by the firing rates of the individual dLGN neurons.

Cortical input to the dLGN targets both interneurons and relay cells. In an attempt to determine whether the effect of removing Ntsr1 on each target is different, we separated our LGN single unit population in two classes according to spike shape (Fig. 2H). Units with narrow spikes, such as the example in Fig. 2C were classified as fast-spiking (FS; 18/122), and are presumably interneurons (McCormick and Pape, 1990). The remainder of units (104/122) were classified as regular-spiking (RS), and are presumably relay neurons. Of our population of FS units, 33% showed reduced visual response in the absence of Ntsr1. Conversely, of all units that were suppressed (n=29/137), 12% were classified as FS units (Fig 2E). Units with the highest evoked firing rates behaved like the example cell in Fig. 2B, showing modest suppression by Ntsr1-CG cells; evoked firing rate was otherwise not predictive of the type or magnitude of the effect (Fig 2I). In sum, Ntsr1 cell projections can either modestly suppress or enhance both RS and FS dLGN unit responses.

Contrast dependence of Ntsr1 dLGN effects

It has been proposed that corticothalamic projections control the gain of dLGN responses (Przybyszewski et al., 2000), and that Ntsr1 cells mediate gain control in V1 (Olsen et al., 2012). Thus, we hypothesized that dLGN sensitivity to increasing stimulus contrast should be affected by Ntsr1 activity. We first verified that the contrast response functions (CRF) of our population of Ntsr1 cells were similar to those described in mouse V1 (Gao et al., 2010, data not shown). We then measured the effect of removing Ntsr1 input on the CRFs of dLGN units using response F1 (Fig. 3). The effect of removing Ntsr1 input on the CRFs of dLGN units was mixed (Fig. 3). As before (Fig 2), we used the change in response magnitude to the highest contrast in order to separate our population in three groups: cells with either (i) a larger than 10% increase (Fig. 3E, red, n = 24/109), (ii) a larger than 10% decrease (Fig. 3E, blue, n=32/109) or (iii) a smaller than 10% change (Fig. 3E, black, 53/109) in the F1 response.

The example in Figure 3A is representative of those neurons in which removing Ntsr1 input increased the response to maximum contrast by more than 10%. The increase in response magnitude was contrast dependent, i.e., it became larger at increasing stimulus contrast. The example cell in Fig. 3B is representative of those neurons in which Ntsr1 had not effect along the entire range of stimulus contrast. Finally, the cell shown in Fig 3C showed the opposite effect, removing Ntsr1 input led to a decrease in visual response. Here again, the change in response magnitude was contrast dependent and occurred along the entire range of contrasts used. To compare across we calculated the difference for each cell between the control CRF and +Arch. We averaged separately the difference CRF for all cells with an increase, an absence, or a decrease in response (Fig. 3A-C, right column) according to the 10% criteria described above. The comparison of the three averages (Fig. 3D) showed that both the increase and decrease in response magnitude was contrast dependent and spanned the contrast range used. Therefore, Ntsr1 input can control response gain in subpopulation of neurons, either upwards or downwards.

To evaluate whether the dynamic range of the CRF changed in absence of Ntsr1 input we calculated the contrast at which the response F1 reached the 50% of its maximum. We found this more valuable for comparison across cells than the C50 from the hyperbolic ratio fits, because most often mouse dLGN CRFs do not saturate. Despite the changes in response magnitude, the value of contrast at 50% did not change after removal of Ntsr1 input. This was shown by the complete overlap of the two distributions (Fig. 3F, +Arch in green) and by plotting the values of individual cells in a scatter plot, which mostly aligned along the main diagonal (Fig. 3G).

In summary, we observed a stereotyped change in the CRF consistent with a gain change (Fig 3A-C), such that Ntsr1-CG effects scale multiplicatively with contrast (Olsen et al., 2012). This multiplicative scaling could indicate that Ntsr1-CG cells implement gain control in dLGN; alternatively, Ntsr1-CG effects could follow global V1 gain changes (Carandini et al., 1997; Carandini and Heeger 2011; Priebe and Ferster, 2012), possibilities we cannot distinguish here.

69

Convergence of Ntsr1 cell projections onto dLGN cells: effect on response selectivity.

If similarly tuned Ntsr1 neurons project to a given dLGN cell, the effects of removing Ntsr1 input on dLGN spike output should depend on these parameters. To test this, we independently varied the orientation, spatial frequency, and temporal frequency of the drifting gratings while interleaving trials with and without Ntsr1 cell hyperpolarization (Fig. 4).

We measured orientation tuning in 47 dLGN units (n=4 mice) and found that most cells were untuned (mean OSI: 0.26 +/- 0.02; n=34/47, OSI < 0.3) or weakly tuned for orientation (n=13/47, 0.3 < OSI <0.6;), consistent with recent reports in mouse dLGN (Piscopo et al., 2013). Removing Ntsr1 input did not significantly alter OSI (+Arch mean OSI: 0.28+/-0.02, p=0.18, Wilcoxon Signed test), for both the untuned and biased groups (p>0.05, Wilcoxon Signed test). We examined orientation-specific effects as we did with contrast, dividing cells into 3 groups based on the amplitude of the effect of removing Ntsr1 input at the maximal stimulus (Fig. 4A, top row). 23 cells showed no change (Fig. 4A, black), 9 cells showed an increased in response to orientation that caused maximal response (Fig. 4A, red) and 13 cells showed a decrease (Fig. 4A, blue). The example cell in Fig. 4B showed a remarkable increase in response to two orientations +Arch (OSI control = 0.08; OSI +Arch = 0.63), and exemplifies the 2/45 for which orientation selective responses are suppressed by Ntsr1 input in control conditions. The two other groups are exemplified by a cell (Fig. 4A, 3rd row) that showed a small orientation preference in control conditions and no change +Arch (OSI = 0.51, OSI +Arch = 0.53) and a cell in which its orientation bias was reduced in the absence of Ntsr1 input (OSI = 0.42, OSI +Arch = 0.31). The average of all cells in each category (Fig. 4A, bottom row) showed no statistically significant effect of Ntsr1 input. This is consistent with the hypothesis that dLGN units receive input from Ntsr1 cells with a wide distribution of orientation preferences, suggesting a high level of convergence of Ntsr1 cells onto single dLGN cells.

We measured the effect of removing Ntsr1 input on the spatial frequency properties of dLGN neurons (Fig. 4B). We found that 28 cells showed an increase in peak spatial frequency (Fig. 4B, red) such the example cell in Fig. 4B in which the response to 0.02 c/º increased by 1.9 spikes/sec. 15 cells showed a decrease in peak spatial frequency (blue), such as the cell in Fig. 4B (4th row) which decreased by 3.9 spks/s at the peak spatial frequency of 0.04 cyc/deg. 66 cells showed no change (black), the example illustrated (Fig. 4B, 3rd row) is a band-pass neuron with a peak spatial frequency of 0.1 c/deg. We found spatial Ntsr1 effect to be greatest at the lowest spatial frequencies, though some effect were observed across spatial frequency.

Ntsr1 input also showed diverse effects on the temporal frequency tuning of dLGN neurons (Fig. 4C). As with orientation and spatial frequency, we classified our cells in three groups according to a set change in maximal response caused by Arch (Fig. 4C, top row). 13 cells show an increase in peak temporal frequency (red), 4 cells a decrease (blue) and 10 cells showed no change in peak temporal frequency +Arch (black). We illustrate these three groups by example cells in which the peak temporal frequency increased (Fig. 4C, 2nd row, from 0.5 to 1.5 spks/s at the peak temporal frequency of 14 cycles/s), decreased (Fig. 4C, 4th row; from 7.6 to 5.0 spks/s at the peak temporal frequency of 8 cyc/s), or was not changed by removing Ntsr1 input (Fig. 4C, 3rd row, peak temporal frequency was 4 cyc/s). Even though the average of all cells in each group showed no significant effect at any particular temporal frequency, it is noticeable that we observed maximal effect of NTsr1 input in 4/25 cells that showed strong release from inhibition at high (>10Hz) temporal frequencies, which is consistent with a role for Ntsr1 cells suppressing dLGN activity at high temporal frequencies (Gulyas et al., 1990).

In conclusion, Ntsr1 cell suppression or facilitation occurs in the lower range of cortical spatial frequency tuning and is consistent across orientation and temporal frequency. These results are consistent with a convergence of Ntsr1 input with diverse tuning properties.

Ntsr1 cells do not sharpen dLGN receptive field properties

Large drifting gratings could conceal spatially or temporally specific effects of corticogeniculate input. To investigate this possibility, we mapped receptive fields (RFs) of dLGN units using reverse correlation to dense ternary noise. This stimulus provided the means to test the hypothesis that spatially distinct regions of Ntsr1-CG feedback provide opposite sign effects in dLGN. According to this hypothesis aligned areas enhance response and misaligned areas suppress dLGN responses (Tsumoto et al, 1978; Marrocco and McLurkin, 1985). Ternary noise also allowed us to test the hypothesis that Ntsr1 input ensures temporal organization among populations of visually responding dLGN neurons (Kalil and Chase 1970; McClurkin et al., 1994; Sillito et al., 1994; Worgotter et al., 1998).

RF area.

Ternary noise yielded approximately circular ON-center and OFF-center dLGN RFs with weak surrounds (Fig 5A). To quantify spatial effects, we fit the reverse-correlated RF at the peak of the response with a two-dimensional Gaussian (Fig. 5B; see Methods). This provides an estimate of the size of the receptive field center. Neither the RF area (Fig. 5C) nor the X and Y measures of the RF (Fig. 5D) were significantly altered by Ntsr1 cell hyperpolarization (X: p=0.30; Y: p=0.38, Wilcoxon rank tests)

RF response magnitude.

The lack of change in receptive field size belies changes in the strength of both bright and dark center responses in the absence of Ntsr1 input. We were able to measure both increases and reductions in firing rate to center stimuli of opposing contrast because the dense ternary noise generated sufficient background firing. The example cell in Fig. 5F was a OFF-

72

center cell, removal of Ntsr1 input reduced both responses to center stimuli, i.e., the excitation

produced by dark stimuli (Fig. 5F, left column, red represents a 10% increase in firing rate over

background firing), as well as the inhibition produced by bright stimuli (Fig. 5F, right column, deep

blue represents a 10% reduction in firing rate with respect to background). In this and all cells the

magnitude of the response was measured at the time of the peak (in the example peak = 100

ms). To quantify the effect of removing Ntsr1 input we measured the change in response

magnitude at each non-noise pixel of the RF center (Fig. 5G; see Methods). We found a

significant reduction in the response to both contrasts (ON: 41%, p=0.002, Kolmogorov-Smirnov;

OFF: 38%; p = 0.001; Fig 5G, mean represented by dotted lines). Across the population (Fig.

5H,J), 26/32 cells showed reductions in the center response to both contrasts (p<0.05,

Kolmogorov-Smirnov test), 4/32 showed a change in only the OFF response, and 2/32 showed

no change in either response contrast. Thus, changes in both ON and OFF response magnitude

combine to yield changes in dLGN cell responsiveness with no change in receptive field size.

When non-noise surround pixels were observed (10/37), we also measured changes in

the strength of the surround by considering pixels in ON- or OFF- responses that were opposite

sign to the center. We averaged the effect of removing Ntsr1 input and found that the strength of

surround reduction correlated with the strength of center reduction, for both ON- and OFF-

responses (Fig 5K). Surround reductions were not significantly different from those triggered from

the center (p=0.96, K-S test). We do not see evidence that dLGN surrounds are more affected by

Ntsr1 projections than dLGN receptive field centers. Thus, since the surround and the inhibitory

center are supposedly mediated by interneurons, our results suggest that Ntsr1 input modulates

relay and interneurons similarly.

RF time course.

The impulse response measured at the RF center was not modified by removing Ntsr1 cell input (Fig. 6A). This was an ON-center cell with an excitatory peak at 88 ms and an inhibitory peak to dark stimuli in the center at 140 ms. From each impulse response (n=35) we measured the time of the peak (Fig. 6B), the amplitude of the peak (Fig. 6C) and the area under the rectified impulse response curve (Fig. 6D). None of these parameters showed differences between control and +Arch (Fig. 6B-D, middle and right columns).

We measured the temporal profile of the response at several locations based on the shape estimate of each RF. At the pixel with maximum response in the RF center (Fig. 6E, pixel 1, solid lines in impulse responses) and at points in the RF surround (Fig. 6E, pixel 2, dotted lines), we saw minimal change in the amplitude or time course of the impulse response after removal of Ntsr1 input. To ensure we weren't missing any temporal effects by measuring impulse responses from individual pixels we computed space-time receptive fields across several one-dimensional slices of the receptive field. The example cell in Fig 6F showed a reduction in the magnitude of the response to dark stimuli in the RF center, which was obvious in 2D RF plots and the impulse response with no change in time course of the response. The space-time RF for this cell (Fig. 6G) revealed that both the dark and bright responses were reduced in magnitude as shown in the color-coded difference plot (Fig. 6G, right), but there was no change in the temporal dynamics of the response.

In summary, Ntsr1 input modulates response magnitude without changing the spatiotemporal properties of the RF of dLGN neurons. Furthermore, center and surround response magnitude were equally affected by Ntsr1 input, inconsistent with the notion that spatial arrangement controls the sign of the corticothalamic effect (Tsumoto et al., 1978).

Ntsr1 cells do not change the temporal fidelity of LGN responses

74

Changes in the temporal distribution of dLGN spikes have been attributed to corticothalamic projections (Kalil and Chase, 1970; McClurkin et al., 1994; Worgotter et al., 1998). Although we did not observe any temporal effects during noise stimulation in the impulse response, we sought to isolate any temporal redistribution of spike output caused by Ntsr1-CG cells from spatial effects. To accomplish this, we used a spatially uniform frozen-noise flicker stimulus (Reinagel and Reid, 2000) and analyzed the fidelity of the response (Kumbhani et al., 2007). Repeated presentations of the same sequence of contrasts (Fig. 7A, top row) generated reliable events under control and +Arch conditions responses (Fig. 7A, +Arch in green). We used a threshold to isolate events from the PSTH and each event was fit with a Gaussian. Three events and their Gaussian fits are illustrated in the example cell in Fig. 7B. From the Gaussian fits to all events and all cells, we calculated the peak time, the width and the height of the event peak. For the population (n=27 cells, 713 events, median 19 events/cell), neither the time of the peak of the event (Fig 7C; Δ peak time: 1.6 ± 0.6 msec, p = 0.31, one sample t-test) nor the duration (Fig. 7D, control: 18.9, +Arch = 19.4; p=0.10, Kolomogrov-Smirnov test) were changed by Ntsr1 removal. To generate a null expectation for difference in event structure between control and+ Arch, we compared the first and second half of all the control trials (Fig. 7C-E, gray). A subset of events showed a change in event structure without a change in spike count – a shortening and widening or a heightening accompanied with a narrowing (Fig 7E). Despite these small changes in event precision, we did not observe a change in event variability (measured with Fano factor; Fig 7H, control: 5.1 ± 0.57, +Arch = 4.6 ± 0.48; p=0.92 K-S test), reliability (Fig7I, control: 2.3 ± 0.34, +Arch = 2.3 ± 0.35; p=0.98, K-S test), or the mutual information regarding the stimulus encoded in the spike train (Fig 7J control: 2.34 ± 0.09, Arch = 2.38 ± 0.1; p=0.78 K-S test). Despite some changes in the distribution of spikes, we find that Ntsr1 input does not affect the temporal fidelity of dLGN stimulus information, for either the full responses or when considering only the first spike (data not shown).

Ntsr1-CG cells affect dLGN coordinated activity

The coincident activity of dLGN cells affects transmission of retinal input to V1 (Wang et al., 2010; Cardin et al., 2010a), can provide extra stimulus information (Dan et al., 1998; Reich et al., 2001), and may be influenced by cortical activity (Sillito et al., 1994; Sillito and Jones, 2002; Andolina et al., 2007). To test if Ntsr1 cells regulate the coordinated activity of pairs of dLGN cells, we calculated cross-correlograms (CCGs; n=392 pairs from 10 experiments) from the activity of pairs of dLGN units generated by drifting gratings of fixed orientation, spatial frequency, and temporal frequency while hyperpolarizing Ntsr1 cells on interleaved trials. In both control and +Arch conditions, CCGs show a robust modulation at the frequency of the drifting grating (Fig 8A, three example cells). The preferred phase of this modulation depends on the relative spatial locations of the dLGN cell receptive fields (Andolina et al., 2007; Stanley et al., 2012); this phase was not altered by elimination of Ntsr1 projections (Fig. 8B), consistent with a lack of changes in spatial properties in +Arch condition (Fig 5). As was expected from the effect on single dLGN units, the effect on CCGs was heterogeneous, with pairs exhibiting a range of increases and decreases in the percentage spikes at the center of the CCG (Fig. 8C). The change in synchronous spikes was not dependent on the phase of the modulation, as shown by the distribution of the differences in peak amplitude along the stimulus cycle (Fig. 8E, red dots); the distribution of changes in synchrony area was centered on zero (Fig. 8E, distribution at right). Changes in correlated spikes, i.e., those at the peak of the CCG regardless of the peak phase, were also variable and independent of phase (Fig 8F). Together, the CCG results indicate that the Ntsr1 modulation of coordinated activity of dLGN neurons is, at least within the range of our stimulus size, uniform in space.

To address a role of Ntsr1 projections in selectively synchronizing dLGN cells linked by stimulus features (Sillito et al., 1994)), we measured the Ntsr1 cell effect on dLGN unit pairwise synchrony while varying the orientation of a drifting gratings (n=45 CCGs from 4 experiments; Fig. 9). As described above, dLGN unit pair CCGs modulated at the temporal frequency of the

grating (Fig. 9A) and, as shown by the example cells in Fig. 9A,B, in this case the phase of the modulation shifted with the orientation of the grating (Stanley et al., 2012). Synchronous activity was not dependent on the orientation of the grating (Fig. 9B), inconsistent with a role for corticothalamic input in selectivity synchronizing dLGN cells only for stimuli with a linking spatial feature. Suppression of Ntsr1 input did not change the area under the center of the CCG at any phase (Fig. 9C), neither did it change the peak time regardless of CCG peak phase (Fig. 9D). In some CCGs (8/45) we also observed a gamma frequency entrainment between the cells; this gamma entrainment was also not stimulus specific (Fig. 9F), inconsistent with the interpretation of gamma entrainment as a feature-binding mechanism (Singer, 2001).

Driving Ntsr1 cells results decreased spike count

The preceding removal Ntsr1 cell function suggests both net inhibitory and net excitatory actions on dLGN relay cells. To directly assess this, we injected an AAV carrying ChR2 into GN220-Ntsr1 mice to record dLGN responses to direct Ntsr1 cell excitation; our injections yielded good coverage of the L6 Ntsr1 population (Fig. 10A). We then recorded thalamic activity during visual stimulation paired with synchronous activation of the transfected Ntsr1 population. Activation of Ntsr1 cells led to robust and reliable decreases in evoked spike count (Fig10 B,C, two example cells, PSTH during Chr2 in blue), regardless of the strength of visual stimulation measured by the contrast of the sinusoidal grating (Fig.10 D,E, for the same two example cells, Chr2 in blue). Anecdotally, synchronous Chr2 activation of Nstr1 cells sometimes caused an initial burst, or increase in spike count in dLGN units in the absence of a visual stimulus (see Fig 10B, indicated by an asterisk), followed by reduced spike count during visual stimulation. Overall, spike count was significantly reduced in 23/32 cells, by an average 63% whereas 1/32 showed a significant increase in spike count (Fig. 10F). The distribution of fold-change in spike count with Chr2 showed that most of the cells lied below 1 (Fig. 10G). In sum, we find that synchronous

activation of Ntsr1 cells elicits strong reduction in dLGN unit spike count, presumably through activation of reticular or local inhibitory input to dLGN relay cells.

Ntsr1 cells do not control thalamic firing mode

Given the net inhibition caused by activation the Ntsr1 population, we wondered if removing Ntsr1 corticogeniculate projections could alter burst frequency. A change in firing mode, or in the proportion of T-channel activity, could result in more visually-evoked spikes even if Ntsr1 cells were providing a net inhibition. Moreover, cortical activity has been shown to affect dLGN interspike interval (ISI) distribution (Worgotter et al., 1998). To measure dLGN firing mode, we constructed composite ISI plots to distinguish tonic and burst spikes. Composite ISIs were generated by plotting, for each spike, the subsequent ISI versus the previous ISI. Bursts, due to a low threshold spike (LTS), generate a characteristic set of three clusters: the first spike in each burst is preceded by a long (>100ms) and followed by a short ISI (<4ms) (Fig. 11A, zone #1); the spike at the end of each burst is preceded by a short (< 4ms) and followed by a long (>100 ms) ISI (Fig. 11A, zone #3). Within burst are characterized by both preceding and following short ISIs (<4 ms; Fig. 11A, zone#2). All other spikes are treated as tonic firing.

Three example cells in Fig. 11A illustrate critical points about spike firing patterns in mouse dLGN. First, the three cells recorded simultaneously responded to drifting gratings with either a large proportion of spike bursts (Fig. 11A, left ISI), predominant tonic firing (Fig. 11A, right ISI) or a combination of both (Fig. 11A, middle ISI). Second, the three cells largely preserve their distinction in firing pattern in response to a very different visual stimulus such as the flicker stimulus (Fig. 11D).

By interleaving control and Arch trials we were able to compare quantitatively the proportion of bursting with and without Ntsr1 input. In the examples cells in Fig. 11, the distribution of ISIs in the visual responses to gratings and the flicker stimuli were not modified in

78

the absence of Ntsr1 input (Fig. 11A and B, green dots). We summed the intervals falling within zones 1,2 and 3 to calculate the percent bursting within the entire visual response in each cell. The comparison of percent bursting in control and +Arch during the response to gratings (Fig. 11B) and the response to the flicker stimulus (Fig. 11E) was similar as the vast majority of neurons lie along the main diagonal of the scatter plots.

In conclusion, our observation of firing pattern and firing rate combined with the observed changes in visual responsiveness in the absence of Ntsr1 cells, indicates that Ntsr1 derived corticogeniculate projections drive a mix of inhibition and excitation, depending on the dLGN cell target and level of Ntsr1 cell activation. Therefore, even though activation of Ntsr1 projection with Chr2 generates almost exclusively inhibitory responses in dLGN, such is clearly not the influence exerted by Ntsr1 input during visual stimulation, since the removal of Ntsr1 cell activity does not lead to clear disinhibition, which would have presumably changed the firing pattern from bursting to tonic and changed the percentage of bursts in the visual response.

Discussion

We find Ntsr1-Cre corticogeniculate (Ntsr1-CG) projections capable of driving both increases and decreases in dLGN spike counts during visually-evoked activity, likely via a mix of indirect inhibition and direct excitation. Tuning properties suggest wide convergence of Ntsr1-CG cells with similar contrast, spatial, and temporal frequency tuning onto single dLGN cells. We do not find evidence that Ntsr1-CG cells sharpen spatial tuning properties or improve temporal fidelity. Finally, we found Ntsr1-CG cells can affect retinal transfer, in a way consistent and predicted by from the effects on single cells.

Anatomical correlates of Ntsr1 cell classification

Previous investigation of CT projections have relied on gross manipulations of cortical activity, whereas here we restrict our manipulation to a more specific cell type, the Ntsr1-CG population. Ntsr1-CG cells are a genetically defined class, as opposed to the many anatomically (Tombol, 1984) or physiologically defined (Briggs and Usrey, 2009) L6 cell classes. Based on the morphology of Nstr1-CT cells (Fig. 1, Fig. 10, Olsen et al., 2012) and distribution of subcortical targets, Ntsr1-CG cells represent a conglomerate of two layer 6 cell classes, the upper L6 dLGN-specific and lower L6 dLGN and lateral posterior nucleus (LP) projecting cells (Bourassa and Deschenes, 1995; Zhang and Deschenes, 1997). These morphological classes correlate with the 'type I' and 'type II', classification based on morphology and the pattern of local cortical input (Zarrinpar and Callaway, 2006). Ntsr1 cells are orientation selective and responses modulate strongly at the drifting grating frequency (Fig 1D), consistent with a simple receptive field structure.

Diversity of spike count effects

While some previous studies have reported a diversity of spike count effects from manipulations of corticothalamic projections (Molotchnikoff and Lachapelle, 1977; McClurkin et al.,1994), others have focused on increases or decreases. What could account for the diversity in spike count effects? One hypothesis, in the visual (Tsumoto et al., 1978; Marrocco and McClurkin, 1985) as well as other corticothalamic systems (Li and Ebner 2007, Temereanca and Simons, 2004) is the alignment of feedback. According to this hypothesis the effect of corticothalamic cells with spatially-aligned receptive field centers is excitatory, while corticothalamic cells centered in the dLGN cell surround provide a net inhibition. Here, we manipulated all Ntsr1 corticogeniculate projections, regardless of the spatial arrangement with the recorded cells in dLGN. Nevertheless, we did not observe any non-uniformities in Ntsr1 effect during noise stimulation, which would expected if corticothalamic projections in different spatial regions provided opposing effects. More direct testing of this hypothesis may require spatial control of the optogenetic manipulation, such that only center-aligned or only surround corticogeniculate cells are manipulated; such arbitrary spatiotemporal specificity is achievable by combining optogenetics with modified-DLP optical systems (Stirman et al., 2012).

Given the parallel population of relay cells in primate and cat dLGN it is possible that the diversity of Ntsr1-CG effect could be correlated with dLGN cell type. To date, only morphological evidence indicates a homology to X/Y-types (Krahe et al., 2011), with functional studies of single cells finding very little evidence for magno/parvo or X/Y type homology (Grubb and Thomson, 2003; Piscopo et al., 2013). Because of the lack of physiological identifier, we are unable to test if any of the observed variance can be attributed to separate, parallel channels in dLGN. However, evidence from other rodents suggests multiple populations (Sumimoto et al, 1969; Hale et al., 1979), so it remains a possibility that parallel mouse dLGN streams could be differently

affected by Ntsr1-CG projections, perhaps with release of inhibition to high velocity stimuli (Gulyas et al., 1990; Hawken et al, 1996; Fig 4).

Gain

We observed changes in spike count that scaled with the contrast of the visual stimulus (Fig. 3). Ntsr1-CG cells are visually responsive; their spike count increases with increasing stimulus contrast. Given this, the fact that the Ntsr1-CG effect was largest for stimuli that induce the largest Ntsr1-CG cell responses indicates that the Ntsr1-CG effects are a function of the Ntsr1-CG spike count. This could be interpreted as a gain control (Olsen et al., 2012); alternatively, it could be interpreted as a scaling of the Ntsr1 effect with the gain of system. That is, whatever the Ntsr1 cell effect, that effect will scale with total V1 activity. In this sense, Ntsr1 cells may not be implementing gain control in the thalamus (Saalman and Kastner, 2009), bur rather providing a change in spike count that itself is also gain controlled.

Regulation of retinal transfer, receptive field spatial extent, and temporal properties

Our cross–correlation data indicate that Ntsr1-CG cells can regulate transfer of retinal input both up and down. This is evident in the increases and decreases in spikes in the non-linear synchrony window. These spikes, occurring within 10 milliseconds of each other, are more effective at driving downstream cortical activity (Cardin et al., 2010a; Wang et al, 2010), and are up and down-regulated by Ntsr1 activity (Fig 8). The present data do not address under what condition, or toward what end, such regulation would occur, or if it does at all.

We do not find evidence that Ntsr1-CG cells sharpen spatial tuning properties or improve temporal fidelity, suggesting that cortical influences on these dLGN response features either use another channel or are species-specific. It is possible that surround effect require more effective

engagement of the surround than our stimuli provided. Our stimuli are limited by the size of the monitor, which may not always be large enough mouse receptive fields, especially given that the stimuli are tailored for only a subset of the many cells recorded using our mutlitetrode approach. Changes in neuromodulation caused by cortical manipulation of non-CT cells could account for increase in stimulus information reported in other studies (Goard and Dan, 2009; Worgotter et al, 1998; Andolina et al., 2007).

Putative Mechanisms

Consistent with the reduction in dLGN spiking generated by electrical stimulation V1 (Marocco et al., 1982; Ahlsén et al., 1985), transcranial magnetic stimulation of V1 (de Labra et al., 2007), as well as previous reports in the mouse visual system (Olsen et al., 2012), we found that synchronous activation of Ntsr1-CG cells elicits reduction in spike count, presumably through activation of RE or local inhibitory input to dLGN relay cells. However, Ntsr1-CG activity does not always result in net inhibition, as evidenced by our Arch experiments removing Ntsr1 activity. We propose that Ntsr1 effects are a balance of monosynaptic excitation and disynaptic inhibition that can be tipped toward either inhibition or excitation. Synchronous activation results in a large inhibition. These results highlight the usefulness of pairing gain- and loss-of-function experiments.

An alternative possible explanation for a decrease in thalamic spike count is change in firing mode, from burst to tonic, whereby a depolarization would reduce the number to burst spike evoked by an excitatory input (Guido and Weyand, 1995). According to this hypothesis, manipulating Ntsr1 projections should create changes in burst frequency or magnitude. We do not see evidence change in either burst frequency or magnitude in the absence of Ntsr1 cell activity (Fig 11).

Non-sensory functions of corticothalamic projections

Corticothalamic projections have been hypothesized to participate in several non-sensory functions such as spindles (Contreras and Steriade, 1996), seizures (McCormick and Contreras, 2001), and the sleep-wake transition (Steriade and Timofeev, 2003). Our data support the role of corticotgeniculate projections in absence seizures, as strong synchronous activity of Ntsr1 cells could deeply inhibit thalamic activity, though no visual stimuli we used are sufficient to tip the balance to strong thalamic inhibition in this way. The relatively subtle and bidirectional effects limit what role these cells might have in generating an oscillation, but they may be able to modify an ongoing oscillation. Ntsr1 cells did not specifically affect the oscillations we observed, pairwise gamma oscillations. We propose that the effects of Ntsr1 on oscillations are general and mixed, just as Ntsr1 sensory effects are general and mixed.

Figures
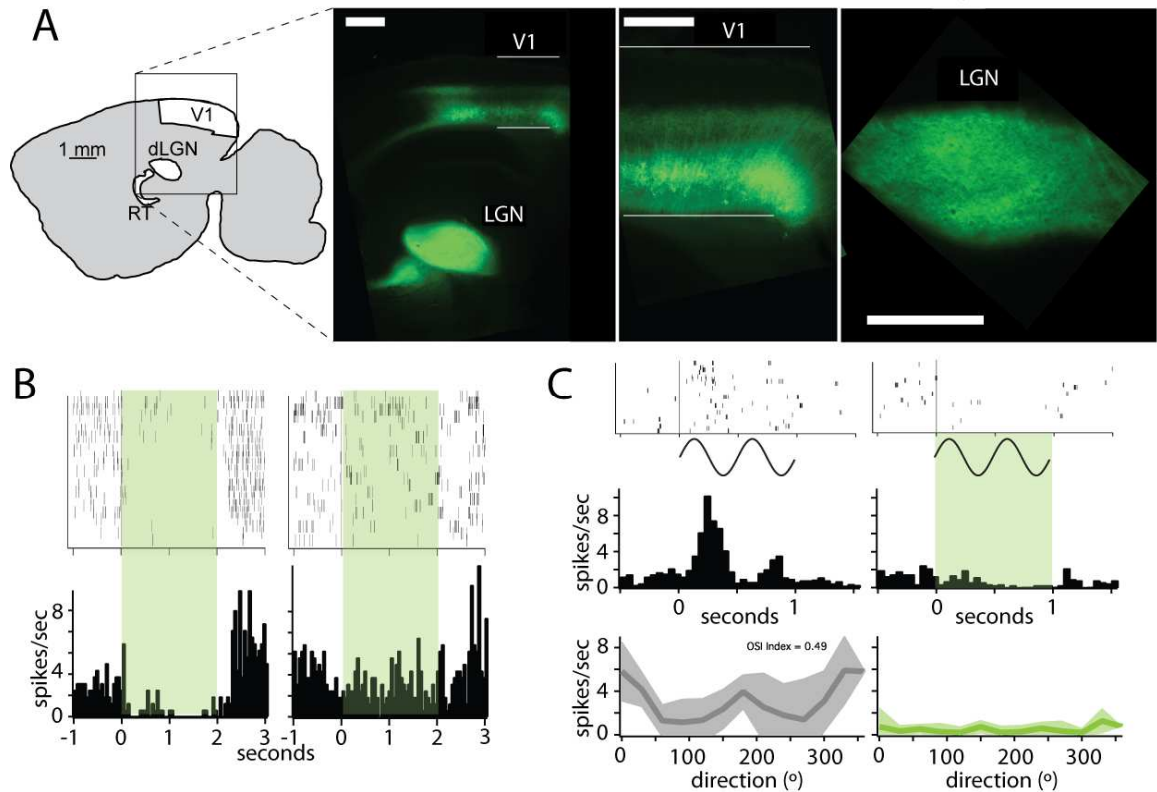
Figure 3.1 Optogenetic inactivation of L6 corticotgeniculate cells.
A, Expression of Arch-GFP carried by an AAV 2/9 vector in Ntsr1-Cre mice, injected directly into

V1. Expression shown is 4 weeks after injection. Paraformaldehyde fixed tissue, sagittal section;

scale bar 0.5 mm. B, Hyperpolarization of cells in layer 6. Optical fiber is placed directly in

primary visual cortex; array of tetrodes lowered to approximate L6 depth (example shown: 712

um). Spontaneous firing of a cell (left) is eliminated by activation Arch; spontaneous activity of

another cell recorded on the same tetrode (right) is unaffected by Arch. C, Hyperpolarization of a

layer 6 cell by green light during visual stimulation with a drifting grating. Two cycles of a drifting

grating evoke a modulation response (left).; enveloping activation of Arch eliminated the activity

evoked by the same stimulus (right).

85
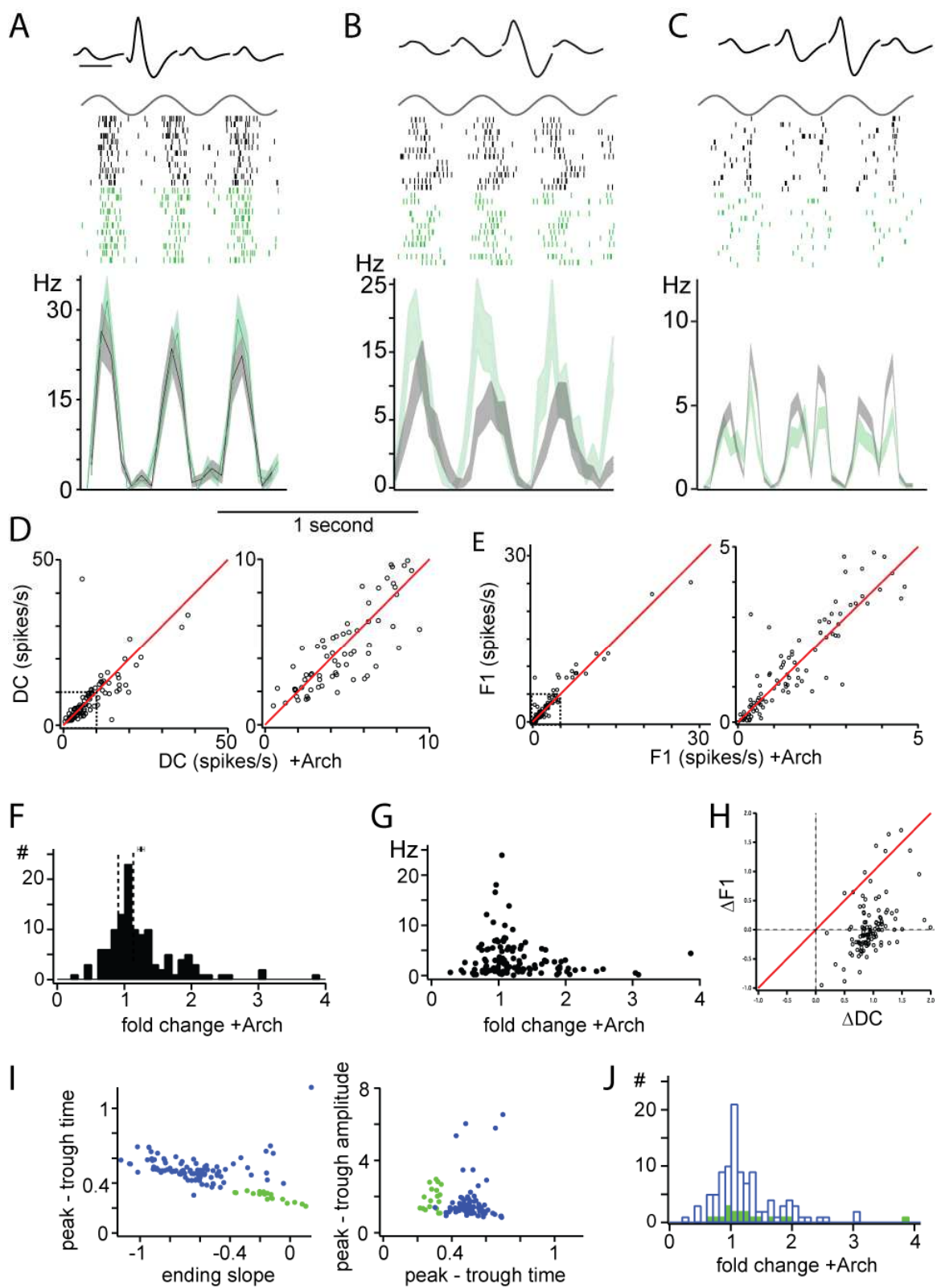
Figure 3.2 Effect of hyperpolarizing Ntsr1 cells on dLGN responses.
A-C, Examples of the effects of Ntsr1 hyperpolarization on three dLGN single units. For each

example, average waveform on each of four tetrode wires is shown above the temporal envelope

of the stimulus. Rasters of control (black) and +Arch (green) trials are separated for clarity, but

were presented interleaved. Peristimulus time histograms calculated with 33 msec bins for control

(black) and +Arch (green) are shown with S.E.M. for each bin shaded. D, Scatter plot (left) of the

effect of Ntsr1 hyperpolarization on the DC component of dLGN responses to gratings. Right plot

shows expansion of marked section in left plot. E, Scatter plot (left) of the effect of Ntsr1

hyperpolarization on the F1 component of dLGN responses to gratings. Right plot shows

expansion of marked section in left plot. F, Distribution of fold change in DC component with

Ntsr1 hyperpolarization. G Fold change in DC component is not dependent on high or low control

firing rate. H, Ntsr1 hyperpolarization effect on the DC component (bottom) correlated with the

magnitude of the effect on the F1 component (left). I, Separation of dLGN single unit waveforms

into RS (blue) and FS (green) according to peak-to-trough time, ending slope (left), and relative

peak-to-trough amplitude (right). J, The distribution of Ntsr1 hyperpolarization effects is the same

for putative RS and FS units.
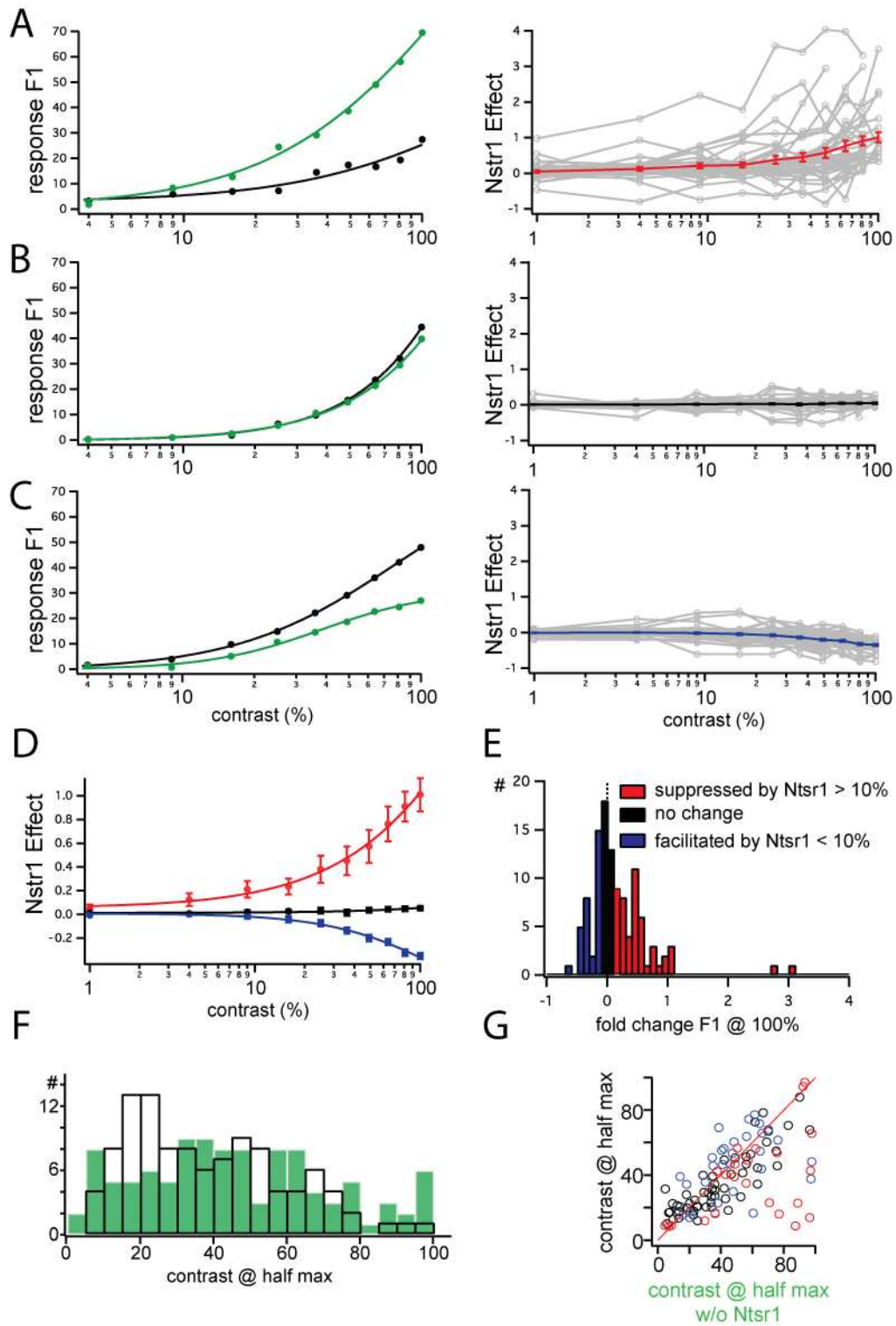
Figure 3.3 Contrast dependence of Ntsr1 cell effects on dLGN units.
A-C Examples and sorted populations of units suppressed (A), unchanged (B), or facilitated (B)

by Ntsr1 activity. For each group, an example unit with control (black) and +Arch (green) contrast

response function is shown at left; all group contrast response functions, and the within group

average, is shown at right. D, Within group average contrast response functions from A-C, plotted

together. E, Distribution of the fold change in the F1 component at 100% contrast. F, Distribution

of contrast @ half maximum response for control (open bars) and +Arch (green) conditions. G,

Scatter plot of data in F.
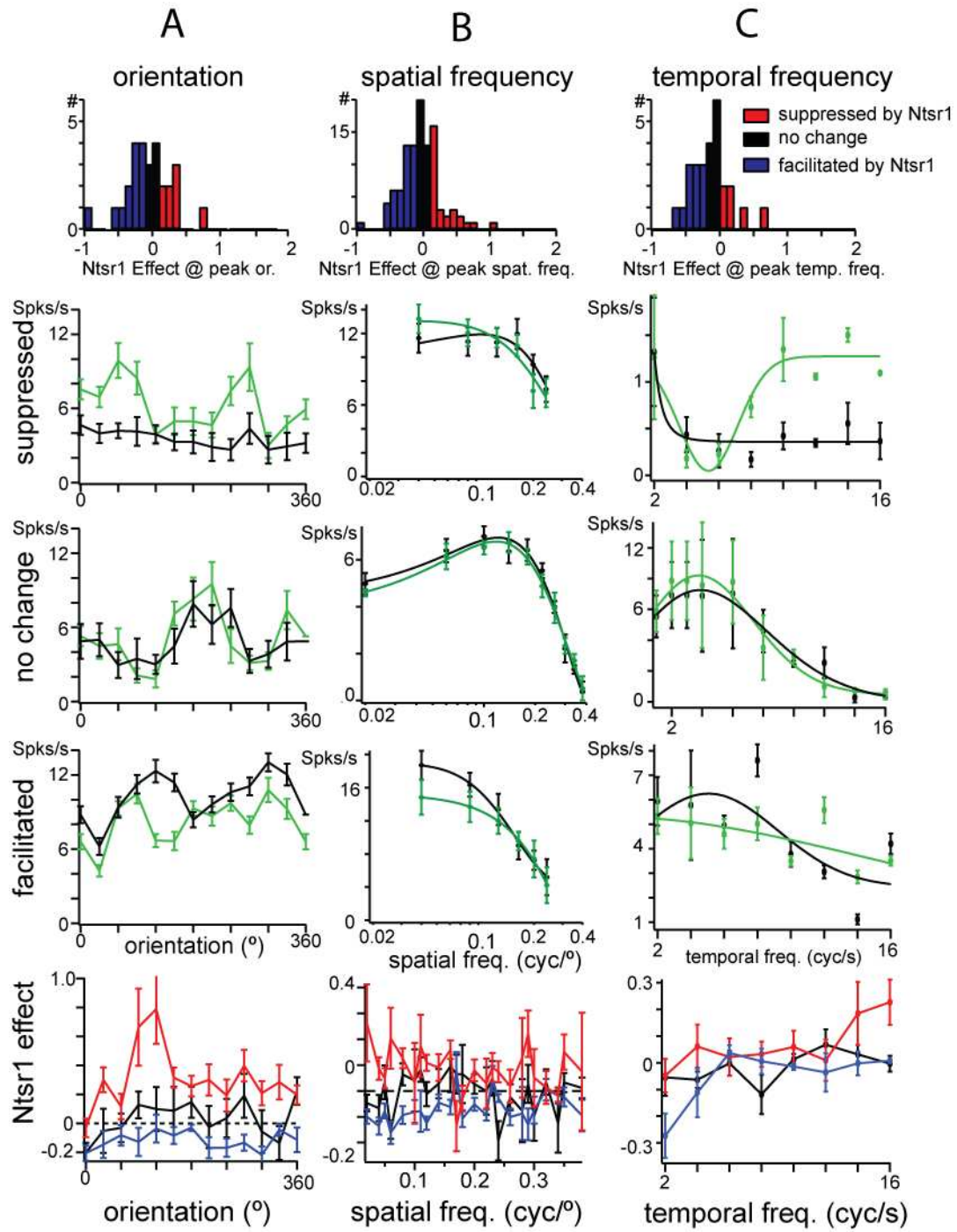
Figure 3.4 Effects of Ntsr1 cells across orientations, spatial frequencies and temporal frequencies.
A, Distribution of the effects of Ntsr1 hyperpolarization of response DC component (top);

examples from each group of effect indicated in *A,* suppressed (top), no change (middle), and

facilitated (bottom); population averages for each group. B, same as *A,* for spatial frequency. C,

same as *A,* for temporal frequency.
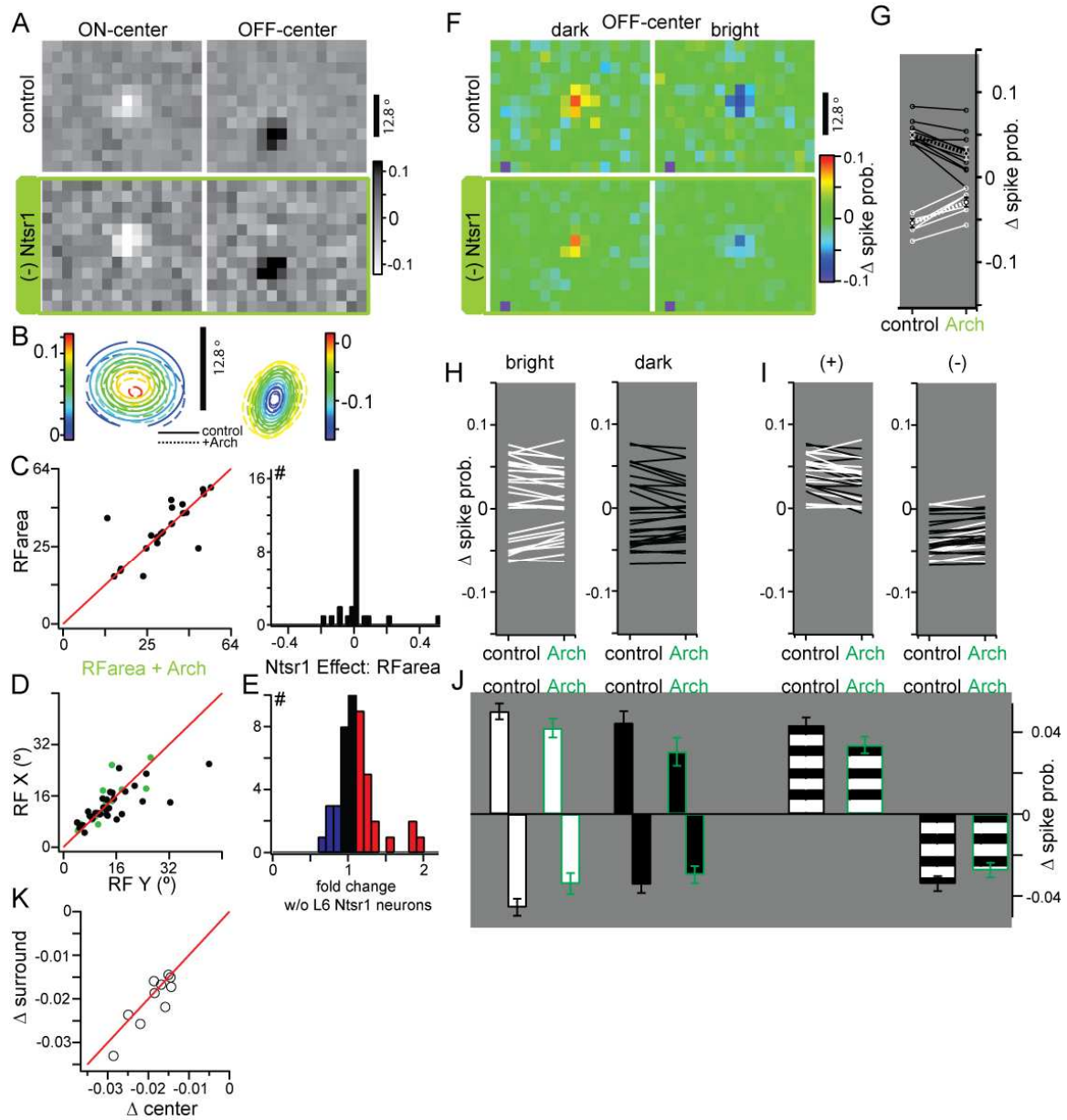
Figure 3.5 Effect of Ntsr1 hyperpolarization on dLGN spatial receptive fields.
A, Spatial receptive fields for an ON-center (left) and OFF-center (right) unit, in control (top) and

+Arch (bottom) conditions. B, 2D Gaussian fits of example cells in *A* for both control (solid

contour lines) and +Arch (dashed contour lines). C, Scatter plot showing the effect of Ntsr1

hyperpolarization on receptive field area calculated from fit parameters (right) and the distribution

of this effect (left). D, Scatter plot of X and Y parameters of in control (black) and +Arch (green)

conditions. E, Distribution of the change in total number of spikes during ternary noise stimulation. F, Bright-only (left) and dark-only (right) receptive fields in control (top) and +Arch (bottom) for an OFF-center cell. G, Pixel-specific changes in non-noise pixels in the dark receptive field (black) and bright receptive field (white). Averages and S.E.M. for each connected by a dashed line. H, Average changes in bright (left) and dark (right) pixels for all cells. I, Average changes in pixels that increase spike probability (left) and decrease spike probability (right). J. Average change in spike probability from plots in H; cells are split by ON-center and OFF-center for solid plots and combined for striped plots. K, Scatter plot of changes in surround versus changes in center strength.
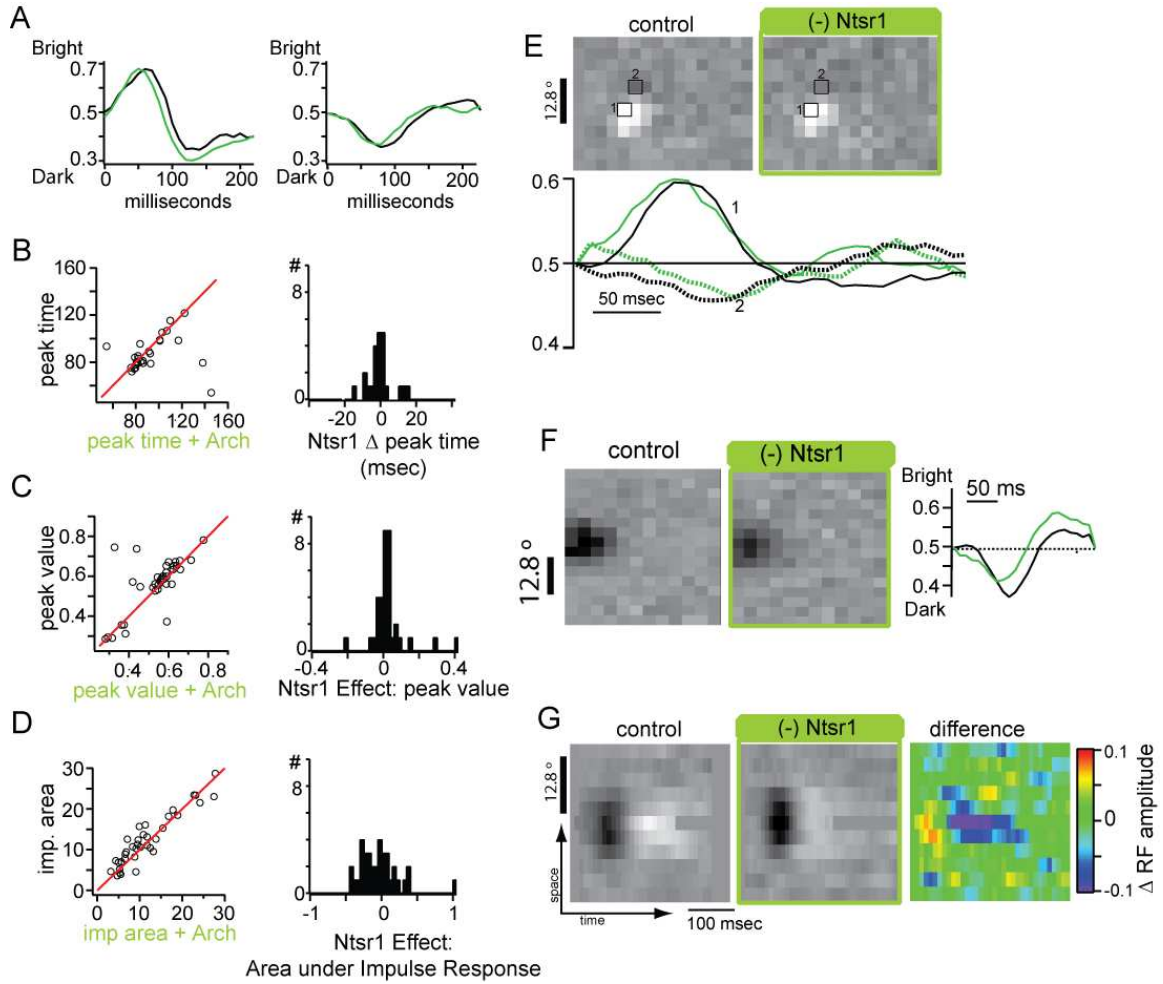
Figure 3.6 Effect of Ntsr1 hyperpolarization on dLGN temporal receptive fields.

A, Example impulse responses for and ON-center (left) and OFF-center (right). B-D, Scatter plots

(left)and corresponding distributions of effects of Ntsr1 hyperpolarization for the time of impulse

response peak (B), the value at that peak (C), and the absolute area under the impulse response

(D). E, Comparison of impulse responses from a center pixel and a surround pixel F,G, Space-

time plot does not reveal any changes in temporal structure for the example cell shown in (F).
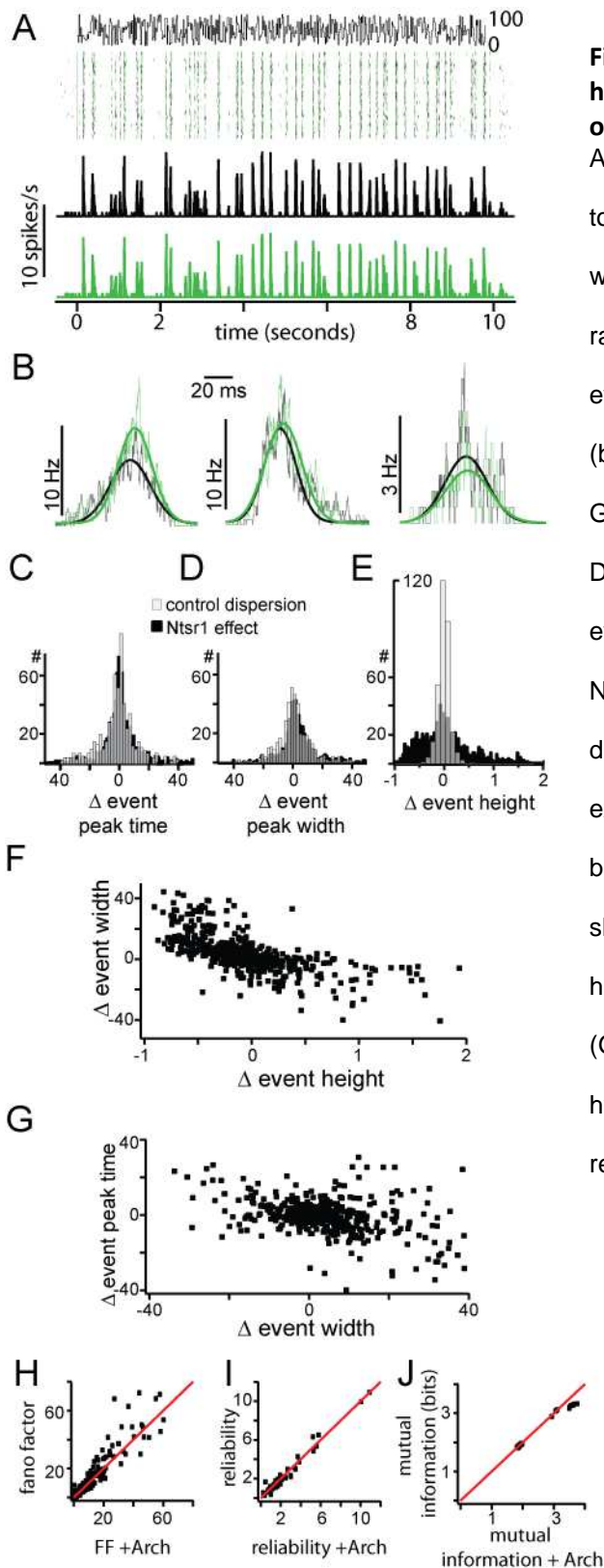
Figure 3.7. Effect of Ntr1 hyperpolarization on temporal precision of response to spatially-uniform flicker. A, Example of a dLGN single unit response to the repeated contrast sequence (top), with control (black) and +Arch (green) raster plots and PSTHs. B. Three example events from the same cell, with control (black) and +Arch (green) overlaid with Gaussian fits to each event. C –E, Distribution of changes in event time (C), event width (D), and event height (E) due to Ntsr1 hyperpolarization (solid bars); difference in peak time, width and height expected from splitting control trials (open bars). F,G, Scatter plot of all events showing changes in event width by event height (F) and event time by event width (G). H-J, Scatter plots of Ntsr1 hyperpolarization effects on fano factor (H), reliability (I), and mutual information (I).
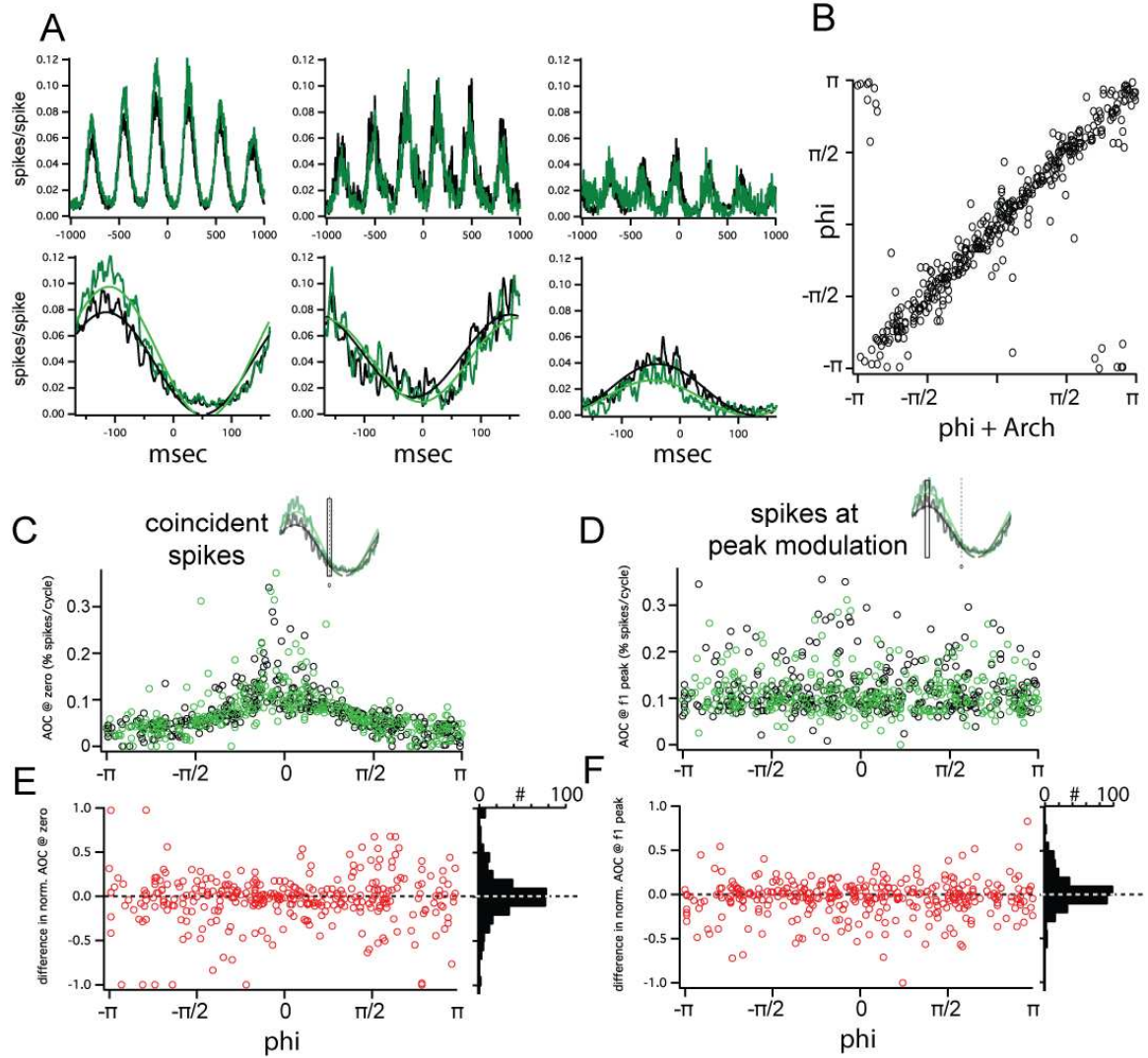
Figure 3.8. Effects of Ntsr1 hyperpolarization of dLGN pairwise coordinated activity.
A. Three example pairs whose modulating correlated activity are increased (left), unchanged (middle), and reduced (right) by Ntsr1 hyperpolarization. B, the phase of the pairwise modulation is unchanged by Ntsr1 hyperpolarization. C, Area under the cross-correlation in the non-linear summation window (+/- 10 msec) as a function of the phase of cross-correlation modulation. D, Area under the cross-correlation at the first peak of the cross-correlation as a function of the phase of modulation. E, difference in area under the curve between control and +Arch conditions in part C. F, difference in area under the curve between control and +Arch conditions in part D.

A

Hz
Cell 1
25
15
5
0   seconds   1

Hz
Cell 2
60
40
20
0   seconds   1

B

0.2 spikes/spikeI

333 msec
1 cycle

radius = 30Hz
——— Cell 1
- - - - Cell 2

C

Δ CCG Area
0.2
0.1
0
-0.1
0   180   360
orientation (º)

D

Δ CCG peak time
300
0
-300
0   180   360
orientation (º)

E

Hz
Cell 1
40
20
0

Hz
Cell 2
6
0

F

200 msec

radius = 40Hz
——— Cell 1
- - - - Cell 2

97
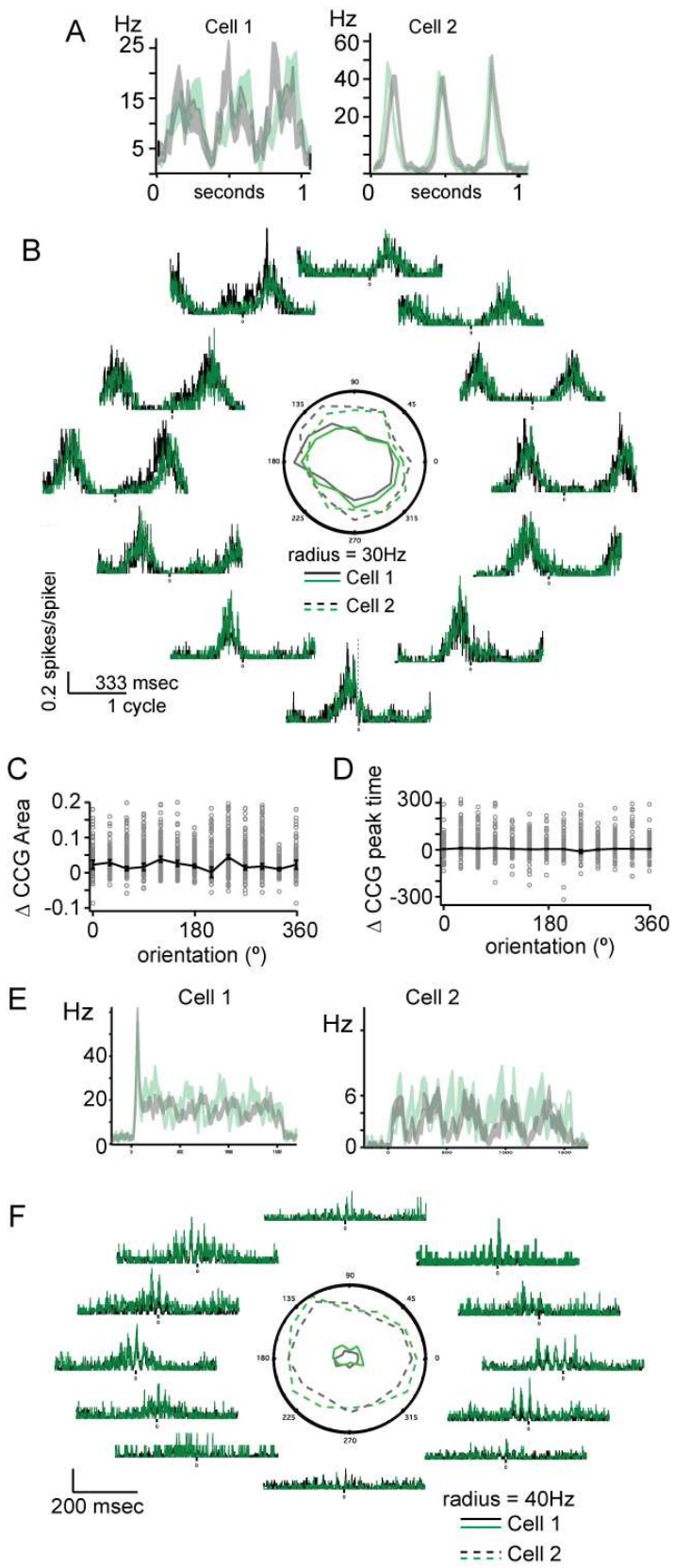
Figure 3.9 No stimulus dependence of Ntsr1 effects on coordinated activity.
 A Drifting grating responses of two simultaneously recorded units. B, Orientation tuning of the

units shown in A (center); cross-correlation of the responses at each orientation showing

procession of modulation peak but no change in peak area or time at any orientation. C,D

consistent change in peak area and time across all orientation for the population of

simultaneously recorded pairs. E Drifting grating responses of two simultaneously recorded units.

F Orientation tuning of the units shown in E (center); cross-correlation of the responses at each

orientation showing no procession of gamma frequency modulation at any orientation.
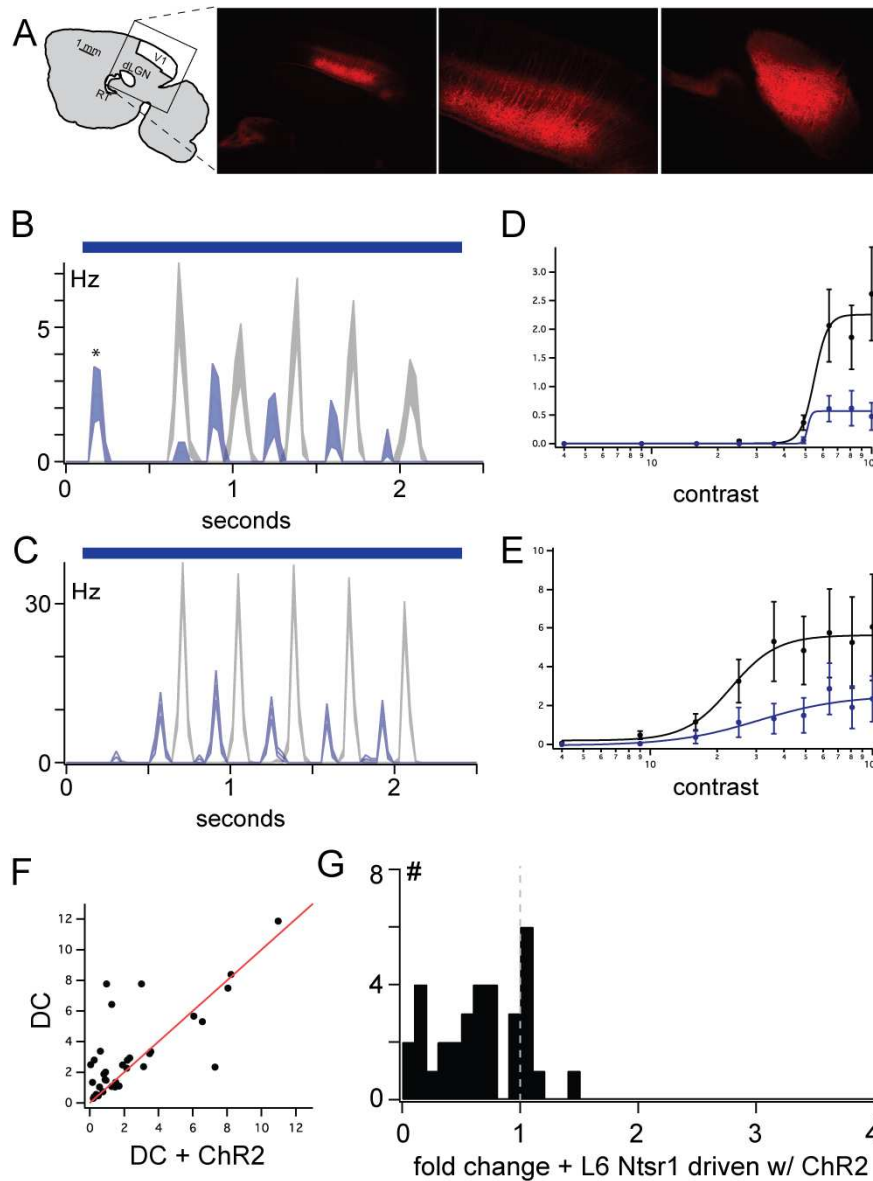
Figure 3.10 Effect of stimulating Ntsr1 cells on dLGN visual responses.
A, expression of ChR2-mCherry in Ntsr1 neurons in layer 6. B,C, Driving Ntsr1 cells causes

decreased visual responses, D,E at all contrasts. F Scatter of the effect of driving Ntsr1 cells on

the DC component of repossess and G the corresponding distribution.
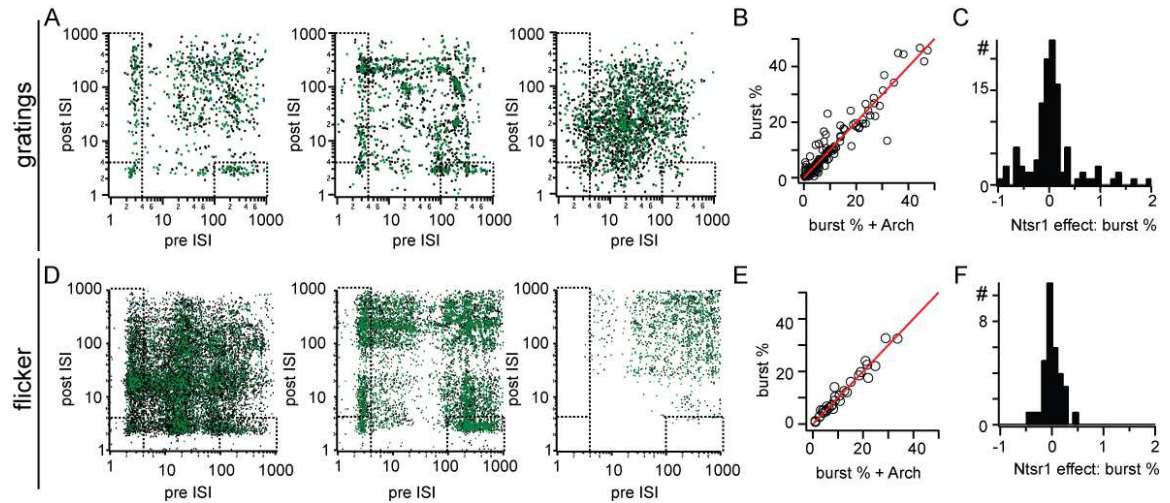
Figure 3.11 No change in dLGN burst statistics due to Ntsr1 hyperpolarization.
A, Composite interspike interval plots for three example cells generated from spike responses to

drifting gratings. Burst spikes fall in the demarcated by dashed lines. B, Scatter plot of percentage

of burst spikes in control and +Arch conditions and the (C) corresponding distribution. D,

Composite interspike interval plots for three example cells generated from spike responses to

spatially-uniform flicker. E, Scatter plot of percentage of burst spikes in control and +Arch

conditions and the (F) corresponding distribution.

CHAPTER 4: EVIDENCE FOR PARALLEL POPULATIONS IN MOUSE DORSAL LATERAL GENICULATE NUCLEUS

Abstract

The mouse visual system is an emerging model for the study of cortical function. To maximize the usefulness of the system, it is important to understand the similarities and differences between the organization of all levels mouse vision and other, better studied systems like macaque and cat. While the characterization of mouse retinal outputs is deep and studies of mouse visual cortex have expanded rapidly, relatively little is known about mouse dorsal lateral geniculate nucleus (dLGN). Here, we present evidence for parallel processing streams in mouse dLGN. We use stimuli that have been previously shown to distinguish parallel streams in other species: optic chiasm stimulation, contrast-reversing stationary gratings, and dense noise for receptive field reconstruction. We find evidence for multiple conduction velocities from optic chiasm stimulation and a subpopulation of mouse dLGN cells show non-linear spatial summation. Our results suggest that parallel processing is maintained in the mouse dLGN, and that despite the lack of lamination, response properties can bear homology to the organization of primate dLGN.

Introduction

Processing of visual information is carried out in parallel streams, from the retina (Wässle, 2004) to the cerebral cortex (Livingstone and Hubel, 1988; Nassi and Callaway, 2009). In cat dorsal lateral geniculate nucleus (dLGN), X and Y pathways are distinguished by the linearity of spatial summation (Shapley and Hochstein, 1984). In primate dLGN, processing is separated into three pathways, including one for depth and motion and one for space and detail: the magnocellular and parvocellular pathways, respectively (Livingstone and Hubel, 1988; Callaway, 1998). Both of these classifications also have an anatomical basis: X and Y cells have separable dendritic morphology and are separated into different layers (Sherman and Spear, 1982). In macaque, the magno and parvoceullular names come from a description of soma size. Magnocellular cells are confined to the two bottom layers while parvocelluar cells are found in the other four dLGN layers.

Evidence for this classification has been found not only in the aforementioned primate and feline systems, but also in ferret, squirrel, and rat (Van Hooser, 2007). However, little physiological evidence for parallel streams in mouse LGN has been found (Grubb and Thompson, 2003; Piscopo et al., 2013), despite evidence for multiple dLGN morphological populations (Krahe et al., 2011) and in the parallel organization of mouse primary visual cortex (Gao et al., 2010). Given the rising prominence of the mouse visual system as a tool for understanding visual processing (Niell and Stryker, 2008; Liu et al., 2009; Niell and Stryker, 2010; Huberman and Niell, 2011; Liu et al., 2011; Niell, 2011; Polack et al., 2013), cortical structure and function (Sohya et al., 2007; Cardin et al., 2009; Sohal et al., 2009; Marshel et al., 2011; Adesnik et al., 2012; Bock et al., 2012; Olsen et al., 2012), and visually-guided behavior (Dombeck et al., 2007; Andermann et al., 2010; Busse et al., 2011; Lee et al., 2012; Carandini and Churchland, 2013; Saleem et al., 2013), it is important to characterize the output of mouse dLGN, if that output is organized into parallel streams when projecting to V1, and how that organization compares to what is known in other species. Towards this end, recent studies have identified direction and

orientation selective cells (Marshel et al., 2012) that may be analogous to koniocellular or W cell pathways and a diversity of response properties (Piscopo et al., 2013) in mouse dLGN

Here, we present evidence for parallel processing streams the mouse dLGN. We recorded the spiking responses of single LGN cells to electrical stimulation of the optic chiasm and to visual stimuli including spatiotemporal noise, drifting sinusoidal gratings, counterphase sinusoidal gratings, and a spatially-uniform flicker sequence. Classification was based on the linearity of spatial summation to a counterphase modulating sinusoidal grating, and distinct classes were observed. We observed approximately 9:1 more X-like than Y-like cells. These classes showed little difference in drifting grating tuning and receptive field parameters, however, we observed parallel populations of spatial and temporal tuning within X-like cells. Most LGN cells observed responded with approximately equal precision and reliability (Kumbhani et al., 2007), with the exception of a subset of slower-responding X-like cells.

Materials and Methods

Animal Preparation and Surgery

All procedures were done within the guidelines of the National Institutes of Health and were approved by the University of Pennsylvania Institutional Animal Care and Use Committee. Adult C57/B6 mice (8– 24 weeks) were anesthetized with a high concentration of isoflurane (5%) and maintained with continuous inhaled isoflurane (0.8–1.2%). The depth of anesthesia was monitored by heart rate (maintained between 300 and 600 beats/min), pupil dilation, pinch reflex, and following the opening of the craniotomy, by the level of synchronous activity in the local field potential (LFP). After placement in a stereotactic apparatus, eye moisture was maintained by application of a transparent lubricant and body temperature was maintained at 37°C by rectal monitoring and a heating pad (FHC Inc., Bowdoin, ME, USA). A 2-by-3 mm craniotomy was opened over dLGN. Following surgery, the entire stereotactic apparatus was rotated 60° to position the contralateral eye in front of the display screen.

Electrophysiology

An array of four to six tetrodes (Thomas Recording GmbH, Giessen, Germany) arranged concentrically was inserted perpendicularly relative to the cortical surface. In both configurations, the tip-to-tip space between neighboring tetrodes was 254 µm. Individual tetrodes were 100 µm in diameter with a central contact at the tip approximately 40 µm below three concentrically arranged contacts around the shaft approximately 20 µm from each other. Signals were preamplified by the tetrode drive and amplified, individually filtered, and acquired at 30 kHz using a Cheetah 32 acquisition system (Neuralynx, Boseman, MT, USA). High-frequency spiking activity was isolated at each contact by filtering between 600 and 6000 Hz. A single channel from each tetrode was duplicated and filtered 0.1–375 Hz to record an LFP. Following a rest period of at least 30 min, each tetrode was lowered through the cortex and hippocampus until audible

modulation of background activity to a test stimulus was apparent. Tetrodes were further lowered until at least one isolatable unit appeared.

Visual Stimuli

All visual stimuli were generated using the ViSaGe stimulus generation hardware (Cambridge Research Systems, Cambridge, UK) and a custom software package utilizing the accompanying MATLAB (Math- works, Natick, MA, USA) toolbox. Stimuli were displayed on a 19-inch cathode ray tube monitor configured to refresh at 100 Hz at 600X800 resolution. This monitor was gamma-corrected using a luminometer and ViSaGe configuration software and placed 30 cm from the eye contralateral to the craniotomy. Full-screen stimuli covered approximately 70° of visual field. After tetrode insertion, the screen was set to a background of 50% luminance. Stimuli consisted of drifting sinusoidal gratings, counterphase reversing gratings, two-dimensional ternary white noise, and a spatially-uniform contrast modulating flicker stimulus. Counterphase gratings were the size of the display (~70º). The spatial phase of counterphase gratings modulated sinusoidally, with a varying spatial frequency and starting phase; the contrast of the grating reversed at 2Hz following a square wave. Ternary white noise and spatially uniform flicker updated at 50Hz. For ternary white noise the contrast each 50x50 pixel square was chosen for each frame independently of the previous frames and other pixels in that frame. Flicker stimuli consisted of a repeated sequence of contrasts; this sequence was generated by choosing randomly from a flat distribution of contrasts.

Electrical Stimulation

Electrical stimuli were delivered through a bipolar stimulating electrode inserted proximal to the optic chiasm through independent burrhole craniotomies made with 500μm of bregma. Each lead

was connected to an stimulus isolation unit controlled by a Master-8 pulse stimulator (A.M.P.I., Jerusalem, Israel). Stimulation was monophasic and the duration was 50µs. Initially large stimulus intensities (2mA) were stepped down in ~0.1 mA increments in order to isolate the sensitivity of components of the dLGN response. a

Spike Clustering and Data Analysis

Spike waveforms from each tetrode were clustered into individual units offline using a mixture of algorithmic and manual sorting (Spike- Sort3D, Neuralynx). Waveforms were initially sorted using KlustaKwik and subsequently manually refined. All clusters with spikes in the 0–1-ms bin of the interspike interval histogram were strictly rejected. To assess the quality of separation of the identified single units, we measured isolation distance and the L-ratio for each cluster ,which indicate the distance of the center of the cluster from the noise and the quality of the moat around the cluster, respectively (Schmitzer-Torbert et al., 2005). Linearity of spatial summation was measured using the frequency components of the response to counterphase gratings (Shapley and Hochstein, 1976). Analyses of drifting gratings and ternary white noise were as performed elsewhere (Denman and Contreras, 2013; Chapter 3).

Results

In order to investigate the possibility of parallel streams in mouse retinogeniculate pathway, we recorded local field potentials (LFPs) and single units from the dorsal lateral geniculate nucleus (dLGN) using an array of independently positionable tetrodes in isoflurane-anesthetized mice (n = 18). We stimulated either the optic chiasm electrically or the retina with a battery of visual stimuli. These recordings yielded 311 single units and 24 multi-unit clusters consisting of a mixture of spikes from several cells. Unless otherwise noted, the analyses described below were all performed on isolated single units.

Electrical stimulation of the optic chiasm.

In cat (Bishop and McLeod, 1954; Bishop et al., 1959) and macaque (Reese and Cowey, 1990) dLGN, retinal ganglion cell afferent fibers have a broad and non-unimodal distribution of conduction velocities. This corresponds to the non-unimodal distribution of retinal axon diameters (Perge et al., 2009). Detailed anatomical characterization of C57/B6 retinal axons suggest a bimodal distribution of axons (Seecharan et al., 2003), but to our knowledge no study of mouse dLGN activity evoked by electrical stimulation of the optic nerve has been published.

To test for the presence of different populations of LGN neurons in the mouse retino-geniculate pathway, we stimulated the optic chiasm electrically and recorded the population field potential in the dLGN. We estimated the distance along the optic tract from the stimulating electrode to the dLGN to be 4.5mm, according to the placement of the stimulating electrode just caudal to bregma (Fig 1A) and the online 3D mouse brain atlas (Allen Institute 3D connection map) and published measurements of the mouse optic nerve (Kurimoto et al., 2010). We also verified the placement of our electrodes into dLGN histologically after each experiment (Fig. 1B) and saw no obvious lamination in mouse V1 (Nissl stain, Fig. 1C). Based on conduction velocities for the two primary populations measured in other species (Gouras, 1969; Sumimoto et al., 1969;

Hale et al.,1979), 20 and 4 m/s, we expected to see electrically evoked responses with latencies of 1.2 and 2.2 ms.. We observed multiple reproducible components in the LFP response to electrical stimulation of the optic chiasm that may indicate the presence of types of inputs with different conduction velocity in mouse. Bipolar field responses showed four overlapping peaks that correspond with those described in cat (Bishop and McLeod, 1954). An early positive-negative peak that corresponds with the arriving volley of fast conducting fibers, followed by the synchronous postsynaptic potential in dLGN neurons, the negative potential r_1. These two peaks can be elicited at much lower intensities than the following two (Fig. 1D, top). The subsequent large and less precise negative field, t_2, corresponds with the arriving volley of lower velocity conducting fibers, and the negative potential r_2 corresponds with the postsynaptic cellular potentials elicited by t_2 (Fig. 1D, bottom). Strength response curves for the different components revealed that the fastest component (t_1) had the lowest threshold, that t_1 correlates with r_1, and t_2 with r_2 (Fig 1E).

Direct comparison of the observed mouse potentials with those from other species (Bishop and McLeod. 1954; Hale et al, 1979) is complicated by two factors: (i) given the small size of structures in mouse compared to cat or monkey, the stimulation of the optic chiasm may have spread to the nearby optic nerve or optic tract and the volleys may arrive from both sides with slightly different delays. (ii) In cats and monkeys the arrangement of horizontal layers and vertical inputs is a key factor in the shape of the LFP response components. In the mouse, the lack of lamination may result in different arrangement of inputs and changes in waveforms compared to those of cat and monkey.

X and Y cells in cat dLGN have statistically different mean response latencies, though the distributions overlap. We therefore thought it important to examine latency of dLGN spike response to optic chiasm. Using 1MΩ tetrodes, we were unable to isolate single units after optic chiasm stimulation because of the large number synchronously active cells generating some signal on each tetrode wire. In lieu of single units, we examined multi-unit activity evoked by optic

chiasm stimulation (Fig. 2). Like population potential activity (Fig 1), we were able to observe several repeatable components of the multi-unit response. We saw large, fast (~900 µsec) negativities corresponding to population spikes beginning at 1.2 at 2.2 and milliseconds after optic chiasm stimulation, consistent with the expected latencies.

Classification of units with the modified null test

The observation of multiple responses components in mouse dLGN is consistent with the presence of parallel populations of relay cells (Krahe et al., 2011). To classify dLGN units we utilized a modified null test (Enroth-Cugell and Robson, 1966; Cleland et al., 1971; Shapley and Hochstein, 1975). We presented stationary gratings modulated in sinusoidally in space and as a square wave in time, at 4 spatial phases, with 30⁰ phase increments, and at 4 spatial frequencies (0.06 cyc/⁰, 0.12 cyc/⁰, 0.18 cyc/⁰, and 0.24 cyc/⁰). A cell was classified as an X-like cell by the presence of at least one spatial phase that elicits no response to the temporal modulation of the grating. The presence of such null-phase indicates that the cell sums inputs linearly over space. The majority of cells had at least one null-phase at one of the tested spatial frequencies (277/311). We call these cells linear. For the example dLGN neuron shown in Fig 3A (cluster isolation shown at right), the largest response was obtained at 0.06 cyc/⁰ and a phase of 90⁰, and this cell had two null-phases 90 degrees away from the maximum, at 0 and 180 degrees.

A subset of cells (34/311) did not display a null position, as the example shown in Fig. 2B. These cells do not perform linear summation of their inputs over space; we called these non-linear cells. At all spatial phases and spatial frequencies non-linear cells responded with an ON-OFF response at twice the temporal frequency of the grating (Fig. 3B). The extracellular waveforms of putative linear and non-linear cells were not significantly different in amplitude of the rising phase, ratio of peak-to-trough, or the slope of the repolarization phase (data not shown).

Linearity of spatial summation.

X cells respond only to one half of the stimulus, so that their response occurs at the fundamental frequency (F1) of the stimulus, with greater modulation of F1 than mean firing rate (DC). Furthermore, the F1 component of X cells responses are modulated systematically as function of stimulus phase. The example linear unit in Fig. 3A showed a sinusoidal modulation of its response F1 as a function of spatial phase (Fig. 4A, filled circles), with only much smaller change in mean firing rate (Fig. 4A, DC, red symbols). In this unit the response had a small F2 component (Fig. 4A, open symbols) also modulated by the spatial phase, but was dominated by F1 modulation.

Y cells respond to both phases of grating reversal, thus leading to a response at twice the frequency of the stimulus (the F2 component) at most spatial frequencies and all spatial phases. Indeed, the non-linear unit illustrated in Fig. 3B showed a response dominated by the F2 component (Fig. 4B), which was larger than both the F1 and DC components and remained constant across spatial phases. The DC component of the response was also constant across spatial phases.

We measured the linearity of spatial summation for all units as the peak of the F2/F1 ratio across all spatial frequencies (Hochstein and Shapley, 1976). We calculated the linearity index (LI) as the mean F2 over maximum F1. An LI above 1 indicates non-linear spatial summation and identifies Y cells in cats; an LI below 1 indicates linear summation and identifies X cells. We therefore classify cells with an L1 less than 1 as linear and greater than 1 as non-inear (Fig. 4C, dotted line indicates value of 1). The linear unit in Fig. 4A had a linearity index of 0.24 (identified as A in the histogram) and the non-linear unit in Fig. 4B had a linearity index of 2.0 (B in the histogram). Our population was dominated by linear cells (277/311); we identify for the first time a population of non-linear cells in mouse dLGN (34/311).

111

Response properties of linear and non-linear cells

In cats and primates, parallel dLGN populations show differences in their contrast sensitivity and their selectivity to spatial and temporal frequency (Livingstone and Hubel, 1988; Tootell et al., 1988). Typically, X and parvocellular cells respond better to higher spatial and lower temporal frequencies, while Y and magnocellular cells prefer higher temporal and lower spatial frequencies. In macaque (Kaplan and Shapley, 1986) these populations are also separable by contrast sensitivity. To assess mouse dLGN, we probed single units with a battery of gratings that varied in spatial frequency, contrast, and temporal frequency (Fig 5). In mouse dLGN, stimulus preferences were not correlated with null test classification. Distributions of peak spatial frequency (Fig. 5A, left), spatial frequency bandwidth (Fig. 5A, right), peak temporal frequency (Fig. 5B, left), temporal frequency bandwidth (Fig. 5A, right), contrast response c_{50} (Fig. 5C, left), and contrast response n (Fig. 5C, right) were not statistically distinguishable ($p > 0.05$, Wilcoxon rank test). In mouse dLGN linear and non-linear summating cells both span a broad range of stimulus preferences.

We did see evidence for parallel spatial and temporal frequency sensitivities in the mouse dLGN population. This is exemplified by the two linear units in Fig. 5D-F (left column). The unit depicted in black had a low-pass selectivity for spatial frequency with peak response to 0.05 cycles/^{o} (Fig. 5A) and high temporal frequency preference with a peak at 5 cycles/s (Fig. 5D). The unit depicted in gray was band-pass for spatial frequency with a higher peak spatial frequency of 0.12 cycles/^{o}, and low pass for temporal frequency with a peak response at 2 cycles/s (Fig. 5E). The black linear unit had higher contrast sensitivity ($c_{50} = 54\%$) relative to the gray unit ($c_{50} = 89\%$; Fig. 5F). While these cells seem to match X-like (the gray cell) and Y-like (the black cell) properties, both had null spatial phases and were classified as linear. Within the linear population, high spatial and temporal frequency preference correlated with narrower tuning width, creating bandwidth and low-pass populations (Fig. 5D,E, right). We see evidence that like V1 (Gao et al,.

2011), mouse dLGN contains parallel linear populations, more homologous to magno- and parvocellular pathways than X and Y.

Receptive field properties

Parallel dLGN populations may differ in the spatial extent of their receptive fields (Xu et al., 2001). We used reverse correlation on spikes elicited by dense ternary noise to obtain the receptive field (RF) of dLGN units (Fig. 6). We fit the reverse correlated RFs with a 2-dimensional Gaussian to measure RF area. The example ON-center and OFF-center units in Fig. 6A and B had RF center areas of 7.8 and $7.6^{\circ 2}$, respectively. The areas of RF centers span from 3.5 to $20.4^{\circ 2}$ with a median of $8.3^{\circ 2}$ (Fig. 6C). The distribution of receptive field areas was unimodal (Fig 6C); populations of null-tested linear and non-linear units were not distinguishable from each other or from non null-tested (unclassified) units (Fig 6D)

The time course of the responses of ON and OFF cells (Fig. 6E) was similar for ON- and OFF-center cells (Fig. 6F,G). We compared the impulse response functions of ON- and OFF-center cells by plotting the peak amplitude versus peak time (Fig. 6F), the distribution of peak times was unimodal with a peak of 83.9 +/- 11.8 ms. Thus, showing that ON and OFF cells show similar response time course.

Precision and reliability.

In cats, Y-cells have slightly higher precision and reliability than X-cells when tested with a stimulus with rapidly changing contrast (Kumbhani et al., 2007). Such differences are in part attributed to the higher temporal resolution of Y-cells in that species. We used a full screen flicker stimulus consisting of spatially homogeneous stimulus whose contrast varies rapidly (50 Hz), drawing from an even distribution of contrasts. Linear units responded robustly to repeated

presentations of the same stimulus sequence (Fig. 7A), giving rise to clear distinguishable events in the accumulated PSTH (Fig. 7A, 1ms bins). These events were at much higher firing rates than the background as seen by the period before time zero in the PSTH. We did observe non-linear units respond to the flicker stimulus.

To estimate precision and reliability we first identified events from the PSTH based on a threshold; each event was fit with a Gaussian. The fits for all the events of the example X and Y-like cells in Fig. 7 are shown at right to show variability in event amplitude and shape (Fig. 7B, left column), and are shown normalized to their peaks in order to illustrate the variability in the width (Fig. 7B, right column). From the Gaussian fits to all events and all cells, we calculated the time, the width and the height of the event peak. We used the width of the events as an estimate of spike precision of the total spikes in the event. The distribution of precision of all events in all cells showed a unimodal distribution with a 7.9 msec median and a mean of 8.8 ± 6.6 ms (Fig 7C).

We measured the reliability of the response as percent of stimulus presentations in which there was at least one spike in the event window (± 30 ms around the peak). Our measure of reliability quantifies the reproducibility of the entire spike train in the response, independent of any variability within each event. The population of dLGN cells was distributed along a range of reliability values from 3% to 97%, with a median of 31.6% and mean of 35.5 ± 23.0% (Fig 7D, bottom).

Discussion

We have used electrical and visual stimulation to look for evidence of parallel processing in mouse dorsal lateral geniculate nucleus. We find evidence for parallel pathways, and that the properties of these pathways may be closer to the organization of primate dLGN than cat dLGN. Like previous reports, we find that mouse dLGN is dominated by the linear spatial summation, though we do observe some non-linear spatial summation.

Retinal basis of mouse dLGN parallel streams

In both primates and cats, parallel processing streams are established in the retina. In the macaque, retinal ganglion cells can distinguished morphologically; the predominant class is the "midget" (or type III or B-type) ganglion cell, which is smaller than the "parasol" (or type II or A-type) ganglion cell (Leventhal et al., 1981; Watanabe and Rodieck, 1989). These cells are also distinguished by their response properties: midget cells tend to have sustained responses to flashed spots, whereas parasol cells display transient responses (de Monasterio and Gouras, 1975). In cats, X and Y type retinal ganglion cells are distinguished by morphology, and by the linearity of spatial summation (Enroth-Cugell and Robson, 1966) and the transience of responses (Cleland et al., 1971). Like primate and cat retinae, mouse retina contains > 20 retinal ganglion cell types (Sun et al., 2002; Völgyi et al., 2009). Morphometric analyses of soma size and dendritic field shape suggest that these types include homologs of A and B type primate retinal ganglion cells and X and Y type cat cell ganglion cells. Recordings from mouse retina validate this morphological evidence: sustained and transient ganglion cells have been observed in the mouse retina (Balkema and Pinto, 1982). In addition, non-linear spatial summation is observed in a subset of mouse retinal ganglion cells (Stone and Pinto, 1993). It is therefore reasonable to hypothesize the continuation of parallel streams into mouse dLGN. Indeed, the percentage of X-

like ganglion cells reported by Stone and Pinto (1993; 87%) agrees with our observations of linear summating cells in mouse dLGN (89%).

Homology of mouse dLGN to other classification systems

We saw several homologies between mouse and cat dLGN. Multiple component field responses were first observed following optic chiasm stimulation in the cat (Bishop and McLeod, 1954; Bishop et al., 1959). Similar to these results, we observed compound responses in the field potential in mouse dLGN. While we were unable to measure spike latencies from isolated single units, we did see multiple compound high-frequency spikes with distinct latencies. Further, in cat retina (Enroth-Cugell and Robson, 1966) and dLGN (Shapley and Hochstein, 1975) cells have been classified by linearity of spatial summation. We were able to classify 11% of mouse dLGN units as non-linear, or Y-like. This frequency of non-linear cells in the mouse dLGN (and retina) is smaller than the frequency of Y cells measured in cats (48%, (Sireteanu and Hoffmann, 1979).

Both of these factors, conduction velocity and linearity of spatial summation, can also distinguish streams in the macaque retinogeniculate pathway. In macaque a 25% subset of magnocellular cells are non-linear (Kaplan and Shapley, 1982), making the total percentage of non-linear cells ~8%, a number closer to the observed frequency in mouse. Like the percentage of linear cells we observe in mouse dLGN, and the number of B-type ganglion cells in mouse, the percentage of midget cells in the macaque retina is ~90% (Dacey 1994). Macaque dLGN cells are more often described in terms of the transience of response, contrast sensitivity and spatiotemporal selectivity. In mouse dLGN, we see a range of spatiotemporal selectivities, though these do not distinguish linear and non-linear cells. Instead, linear cells showed a mix of spatiotemporal profiles, rather like magnocellular and parvocellular populations that are linear in spatial summation (Kaplan and Shapley, 1982) but classifiable by spatial frequency preference

and contrast sensitivity (Kaplan and Shapley, 1986; Livingstone and Hubel, 1988; Tootell et al., 1988).

W-like and koniocelluar-like response in mouse dLGN

 So far, we have discussed homologies of mouse dLGN units with X/Y and magnocellular/parvocellular pathways. In both cat and macaque a third, somewhat catch-all, class of geniculate cells contains a diversity of response properties including orientation selective responses (Levay Ferster 1977; Hendry and Reid 2000). Here, we see some evidence for orientation biased responses in mouse dLGN, but more complete and convincing descriptions of orientation selective responses in mouse dLGN have been published elsewhere (Huberman et al., 2009; Krahe et al., 2011; Piscopo et al., 2013; Scholl et al., 2013). Though mouse does seem to contain a third pathway, how much of the mixed koniocellular and W streams is recapitulated in mouse dLGN is far from resolved by this or any other mouse studies.

Major differences from primate magnocellular and parvocellular designations

        While the organization of mouse dLGN contains several homologies to the macaque system, it must also be noted that there are also several major differences. The most obvious difference is the gross laminar organization: while macaque dLGN has six layers and interlaminar zones, mouse dLGN is not layered. There is some organization in mouse V1, with W-like dendritic morphologies in a dorsal shell and X-like morphologies in a core (Krahe et al., 2011), but this pales in comparison to the organization of both car and macaque dLGN.

        We saw little difference in receptive field size between linear and non-linear cells in mouse dLGN, whereas Y and magnocellular cells tend toward larger receptive fields than X and parvocellular cells, respectively. Several factors may contribute to our inability to see differences

in receptive field size. We combine cells from across retinotopic positions could be a factor. I addition, the large spatial scale of the mouse system could limit our ability to fully stimulate very large receptive fields because of the limits of our stimulus monitor. To resolve this, measurement of eye position for display position and very large displays corrected for distortions may be required.

Figures
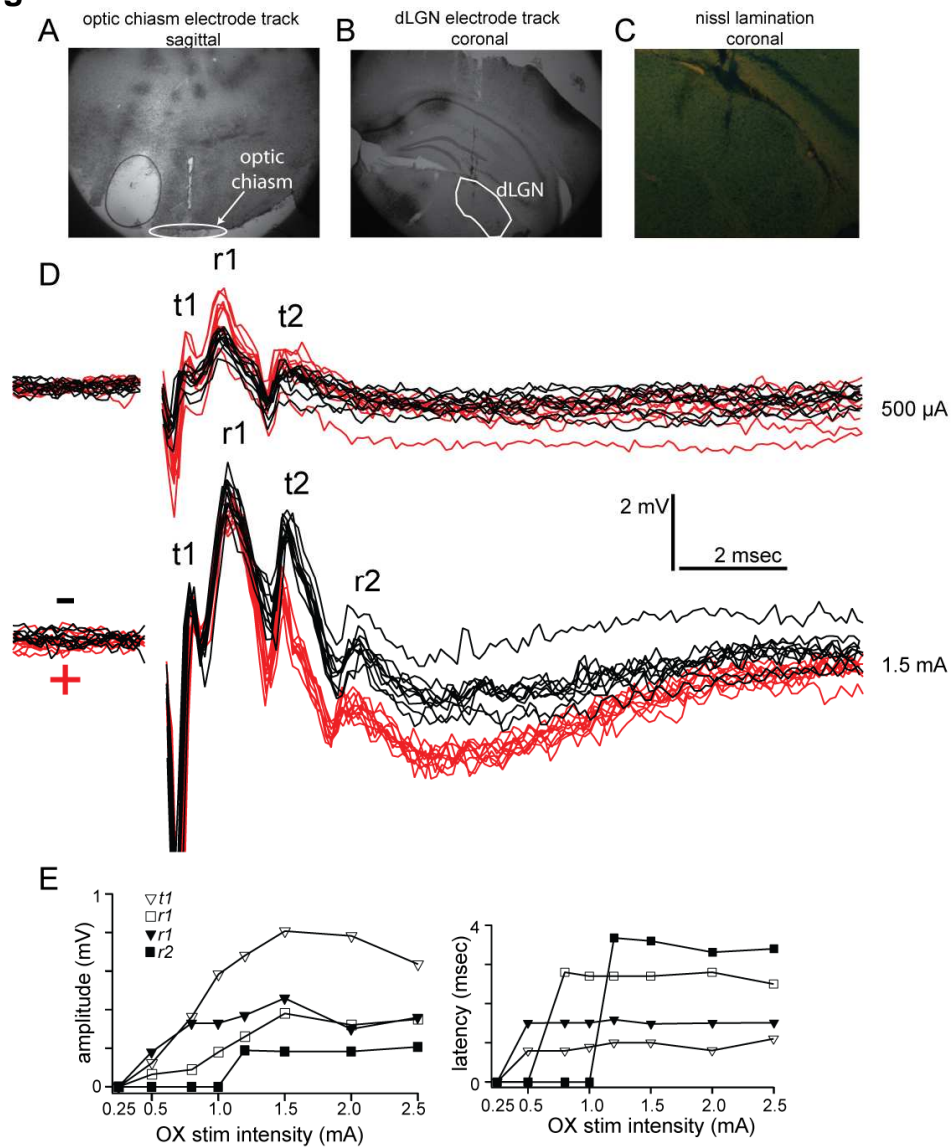
Figure 4.1 Optic chiasm stimulation generates compound field responses in mouse dLGN. A, Electrode track showing positioning of stimulating electrodes at optic chiasm fibers. B, Electrode tracks showing multiple tetrode placement into dLGN. C, Nissl stain of dLGN showing lack of obvious lamination. D, Local field activity in mouse dLGN following dLGN stimulation, at two stimulus intensities: 500μA (top) and 1.5 mA (bottom). E, Measurement of response component latencies and amplitudes. *t1,* open triangles, *t2,* open squares, *r1,* solid triangles, *r2,* solid squares.
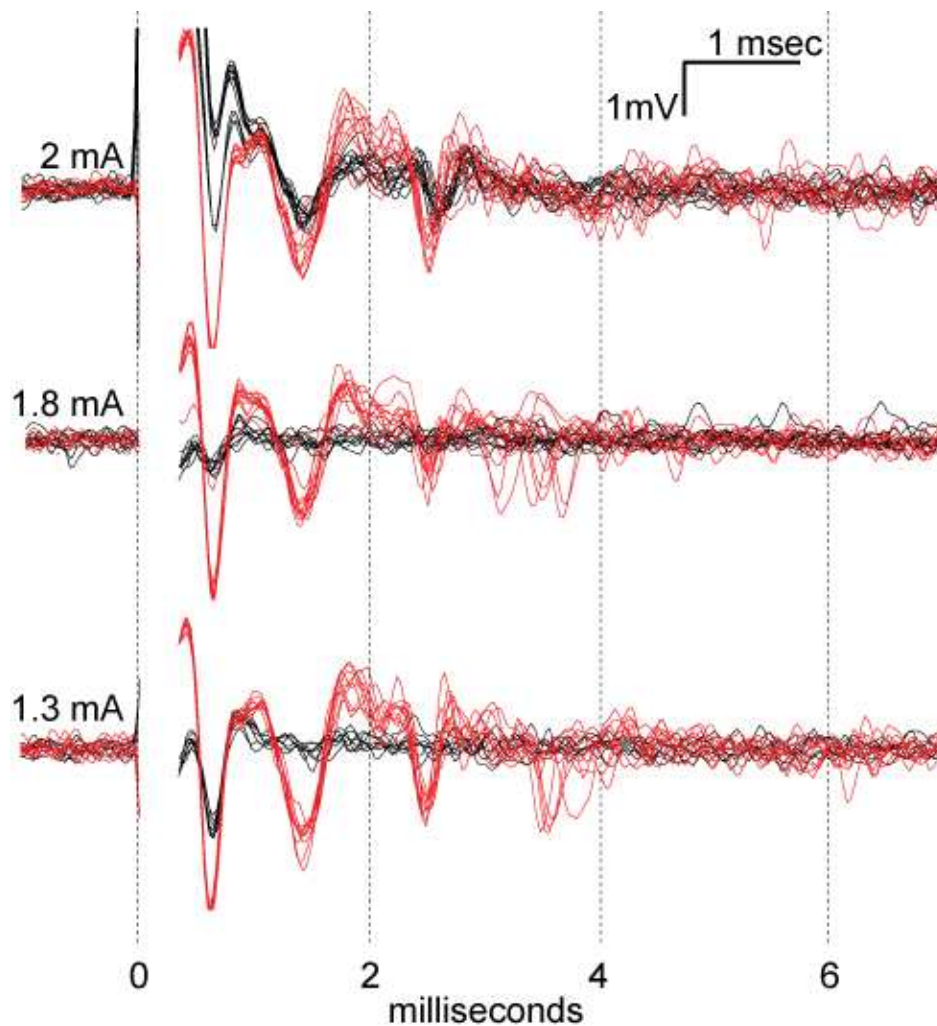
Figure 4.2 Spike activity in mouse dLGN following optic chiasm stimulation.
The high frequency (600 – 6000 Hz) activity is elicited by electrical stimulation of the optic chiasm

at three stimulus intensities, 1.3 mA (bottom), 1.8 mA (middle), and 2 mA (top), for both polarities

of the bipolar stimulating electrode (red and black) Individual trials (8-10 each) are overlaid.

Compound population spikes do not increase in amplitude with increasing intensity (red) and are

elicited at only at 2mA for negative polarity (black).

A

spatial
frequency
(cyc/º)

	0º	90º	180º	270º

Hz

0.06

0.12

0.18

time (msec)

B

	0º	90º	180º	270º

Hz

0.06

0.12

0.18

time (msec)

121
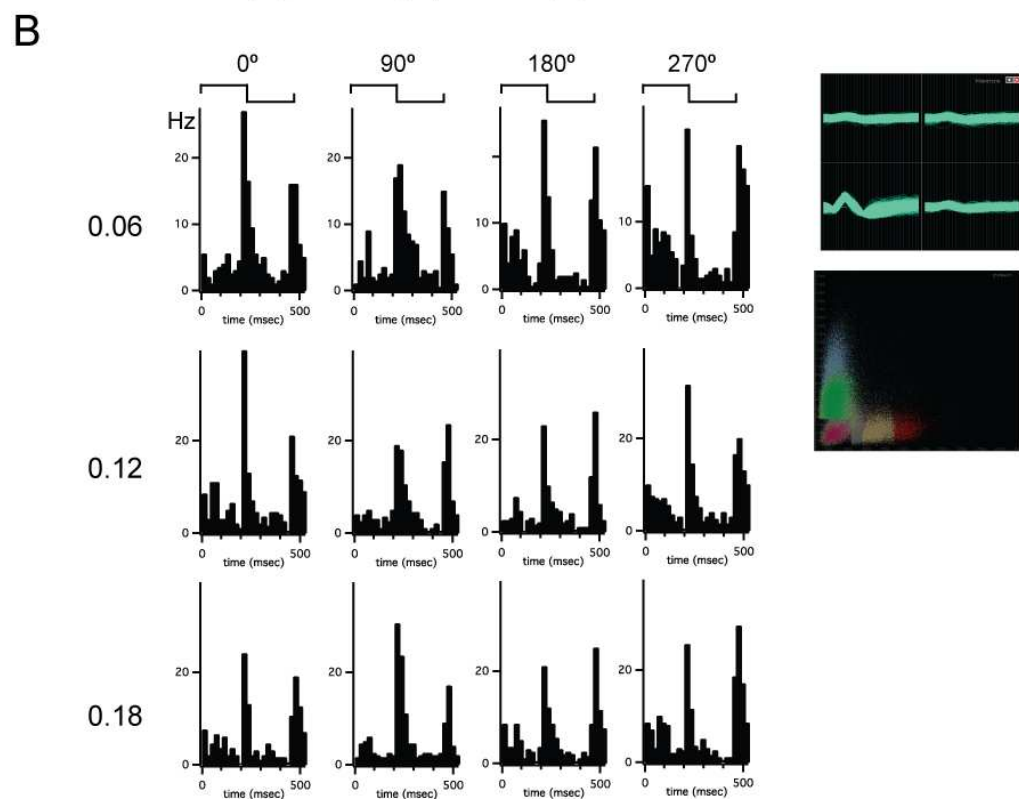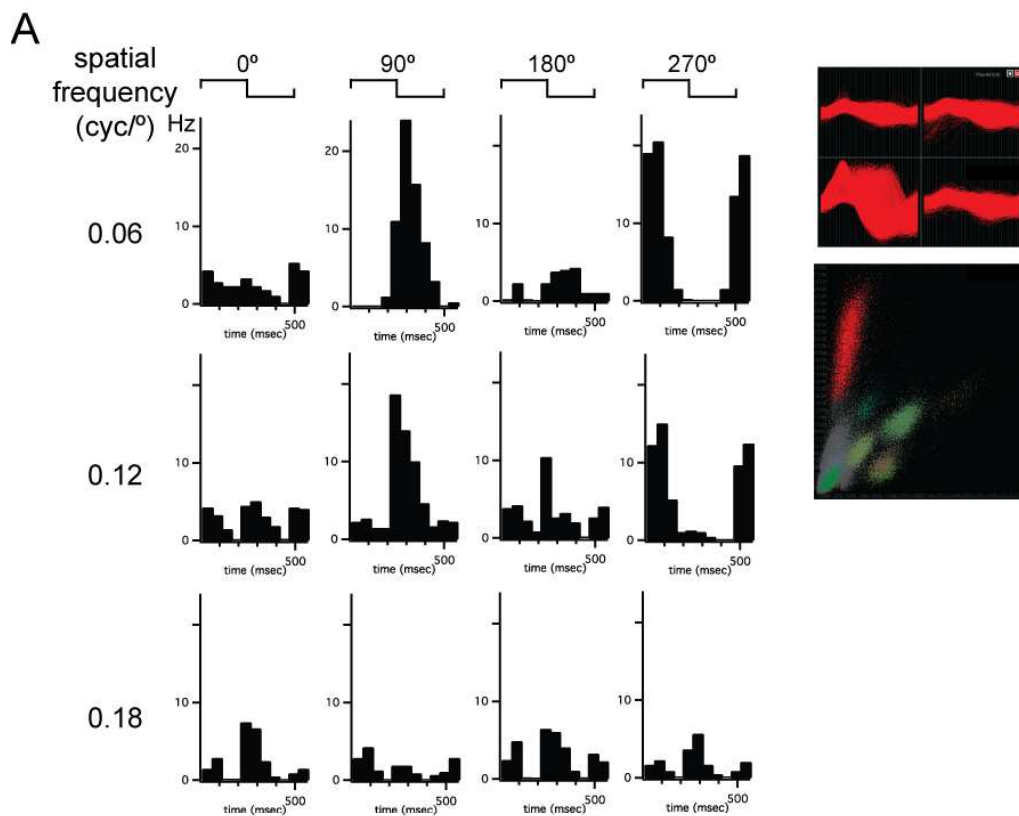
Figure 4.3 Examples of linear and non-linear spatial summation in mouse dLGN.
A, an example of a more common, linear summating unit. Cyclograms from peristimulus time

histograms of responses to four spatial phases separated by 90⁰ are shown in each row; rows

show responses at different spatial frequencies indicated at left. Spike waveform on each wire

shown at right along with a projection in cluster space showing cluster isolation. B, an example of

a unit showing non-linear spatial summation.
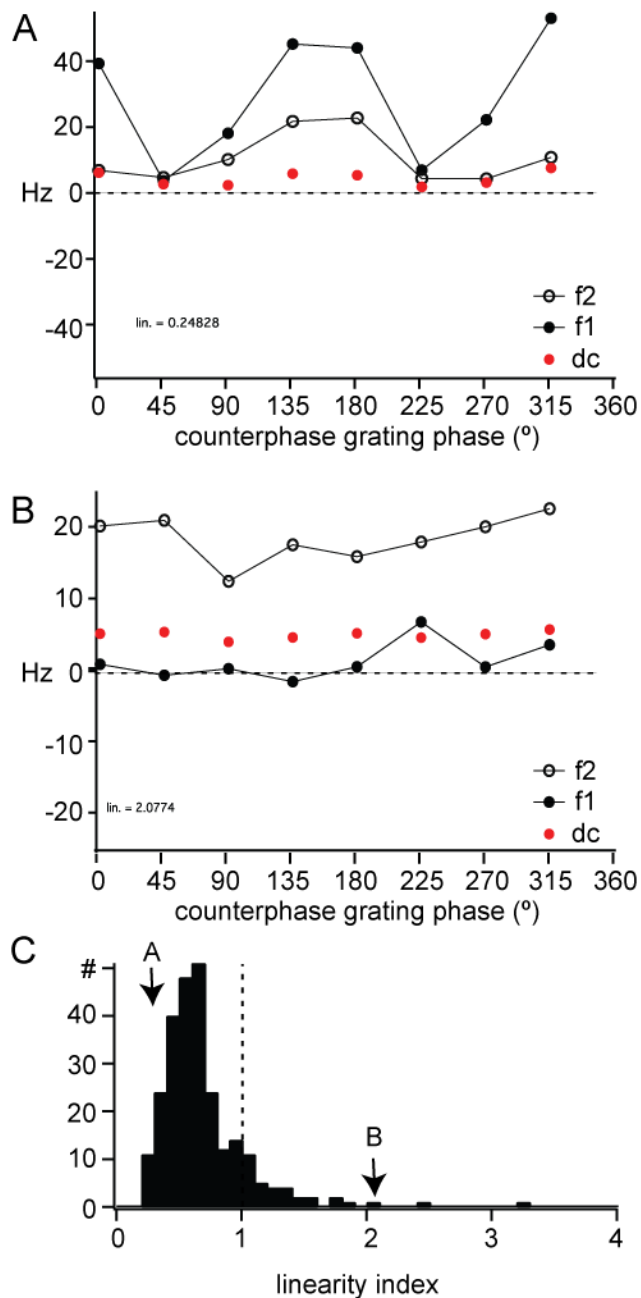
Figure 4.4 Linearity of spatial summation in mouse dLGN.
A,B., The DC, F1, and F2 components of the response to counterphase gratings across all spatial

phases for the example cells shown in Figure 3. C, The distribution of linearity index across our

population of dLGN single units, with the examples in parts A and B indicated with arrows. A

linearity index above 1 indicated non-linear spatial summation.
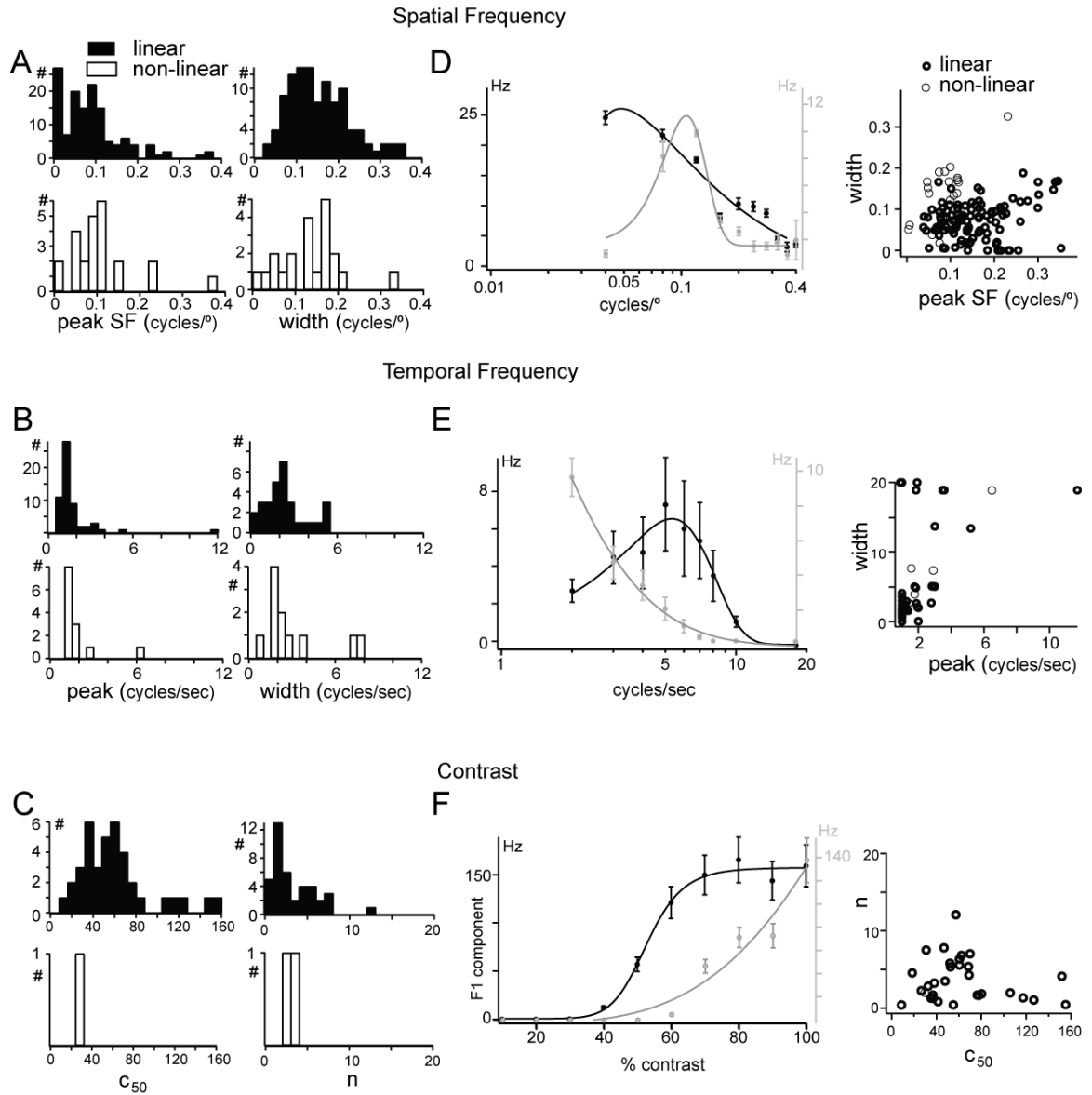
Figure 4.5 Tuning characteristics of linear and non-linear units in mouse dLGN.
A, Distributions of peak spatial frequency (left) and width of spatial frequency tuning (right) for

cells classified as linear (solid bars) and non-linear (open bars) using the modified null test,

measured from fits to spatial frequency tuning plots. B, Distributions of peak temporal frequency

(left) and width of temporal frequency tuning (right) for cells classified as linear (solid bars) and

non-linear (open bars) using the modified null test, measured from fits to temporal frequency

tuning plots. C, Distributions c50 (left) and n parameters (right) of contrast response functions for

cells classified as linear (solid bars) and non-linear (open bars) using the modified null test. D-F,

Examples of opposing spatial frequency tuning (top), temporal frequency (middle), and contrast

sensitivity (bottom) between two linear cells (black and gray traces).
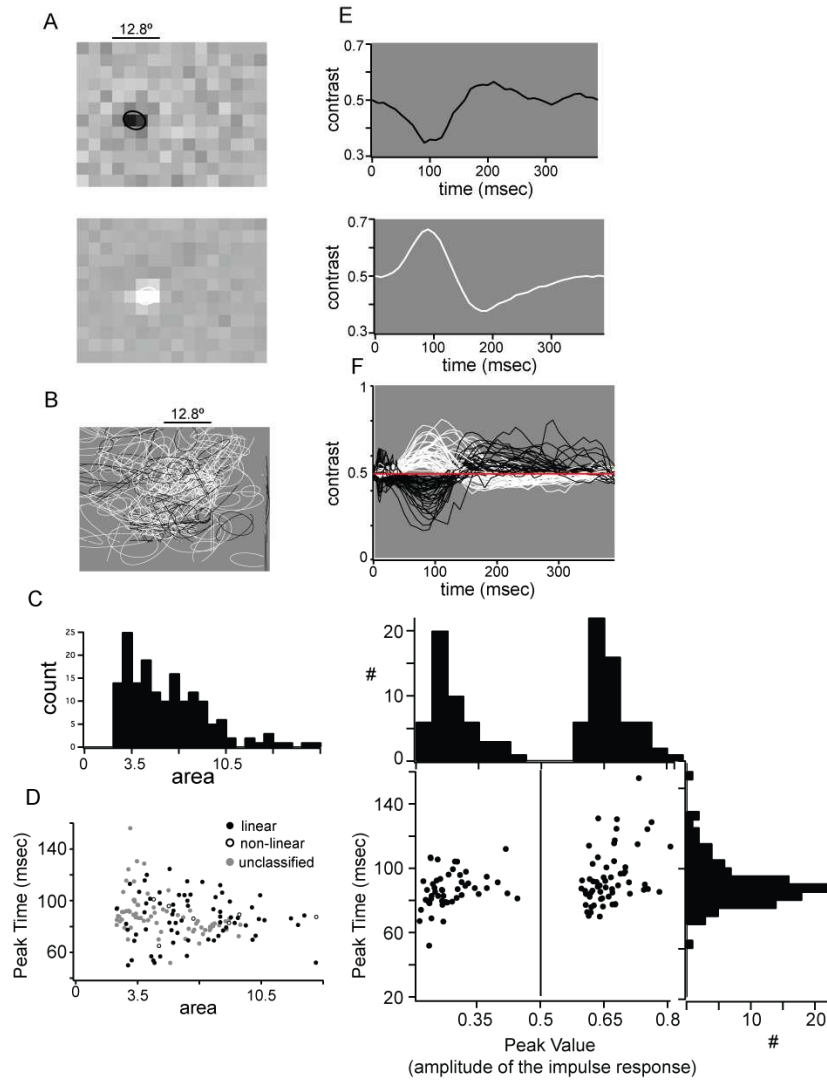
Figure 4.6 Receptive field properties of single units in mouse dLGN.

A, Example spatial receptive fields from an OFF-center (top) and OFF-center (bottom) cell. B, All spatial receptive fields from our population. For each cell the 0.5 level contour from a two-dimensional Gaussian fit is shown. C, distribution of receptive field areas in mouse dLGN, calculated from two-dimensional Gaussian fit parameter. D, No difference in linear, non-linear, and unclassified receptive field areas. E, Impulse response function from the center of the example receptive fields shown in part A. F, All impulse responses from our population. G, Bimodal distribution of impulse response absolute maxima, but unimodal distribution of maximum time.
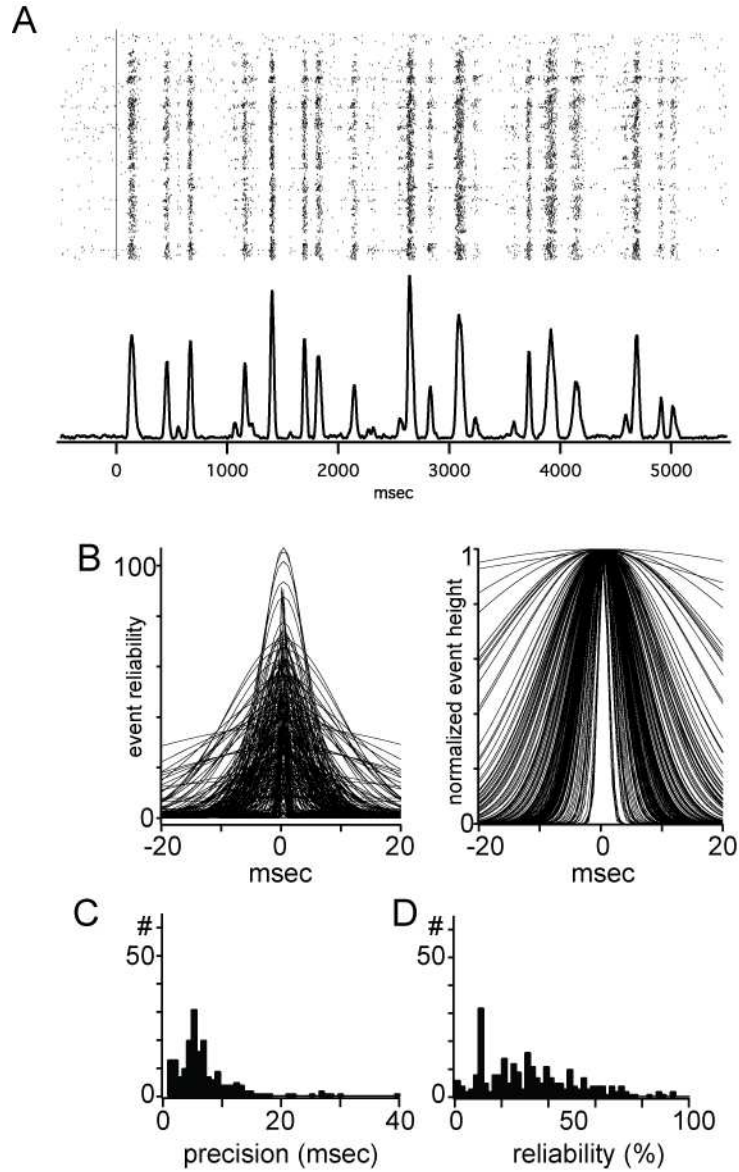
Figure 4.7 Reliability and temporal precision of mouse dLGN single units.
A, Example response of a mouse dLGN cell to spatially uniform flicker. B, All response of mouse

dLGN to flicker; each identified event has been fit with a Gaussian, aligned, and overlaid here

(left) and normalized to the maximum of each event to show the temporal precision of each event

(right). C, distribution of width of the Gaussian fit to each event. D, distribution of event reliability.

CHAPTER 5: CONCLUSIONS AND FUTURE DIRECTIONS

In this thesis, we have investigated two populations of V1 output neurons, layer 2/3 cortico-cortical neurons and layer 6 corticogeniculate neurons in the mouse early visual system. We find several aspects of the early mouse visual system are organized in a similar fashion to other species. First, dorsal lateral geniculate nucleus contains parallel, overlapping populations as classified by physiological responses, despite an absence of obvious layer structure in the thalamus. Second, the correlation structure is organized by distance and orientation preference, despite differences in somatic organization. Utilizing transgenic tools to specifically manipulate layer 6 corticogeniculate cells, we find that these cells are capable of regulating general dLGN responsiveness to visual stimuli. In the course of these studies, we have also found evidence for parallel processing streams in mouse dLGN.

Mouse as a model system

The current boom in interest in mouse vision (Huberman and Niell, 2011; Niell, 2011; Baker, 2013) is not without its detractors (Movshon, 2013). Critics point to a lack of spatial resolution, differences in rodent eye movements (Wallace et al., 2013) and major differences in the organization of response properties. Some of these differences in organization are: the homogeneity of dLGN responses (Grubb and Thompson, 2003), lack of V1 lamination, and a lack of orientation pinwheels in V1 (Ohki and Reid, 2007). Our data do not directly address lamination in mouse V1, though we do observe changes in response features through the depth of cortex, with complex cells superficial to simple cells (Chapter 2). Our data indicate that some of these apparent differences in organization actually hide striking similarities in organization. First, we

observe distinct response groups in mouse dLGN: multiple inputs from optic chiasm stimulation, a subset of relay cells with non-linear spatial summation, and a diversity of spatial and temporal selectivity (Chapter 5). Second, although neighboring cells lack a somatic organization in orientation preference, function connectivity and noise correlation both follow orientation selectivity. This indicates a specificity of connection that respects both space (which is organized in a map) and orientation (which is not organized in a map).

Why do orientation pinwheels, or functional maps more generally, exist? Mouse V1 has comparable single cell orientation sharpness, functional connectivity, and noise correlation in the absence of an orientation map. Functional maps have been proposed to exist in order to reduce wiring cost, given the amount of neurite 'wire' required to generate the observed properties (Koulakov and Chklovskii, 2001; Chklovskii et al., 2002). Due to the size of mouse V1, this wiring may be energetically reasonable even in the absence of the cost-reducing orientation. The developmental mechanism by which such connectivity might be established are not fully described, but great advancements have been made describing molecular mechanisms of synaptic specificity (Clandinin and Feldheim, 2009; Josten and Huberman, 2010).

Our analyses further support the usefulness of mouse as a system for understanding visual neuroscience. Despite the homologies, questions remain about the usefulness of mouse vision. One of these questions is the behavioral relevance of visual processing in mice. Integrating physiology with behavior is an active area of expansion in mouse visual physiology (Andermann et al., 2010; Carandini and Churchland, 2013; Saleem et al., 2013). New insights into V1 have already resulted from awake, behaving mouse preparations. For example, firing rate in V1 is modulated by locomotion (Niell and Stryker, 2010) this locomotion can modulate response gain and may be a result of locomotive regulation of neuromoduation (Polack et al., 2013).

Parallel processing in mouse dLGN

Prior investigations of mouse dLGN have yielded mixed conclusions about the homology of mouse with other mammalian dLGN (Grubb, 2003; Krahe et al., 2011; Marshel et al., 2011; Piscopo et al., 2013; Scholl et al., 2013). We have shown evidence that mouse dLGN contains multiple parallel populations of relay cells. It remains an open question if parallel populations exist in mouse dLGN, and whether they bear greater homology to the X/Y/W cell classification of the cat visual system or the magno-/parvo-/konio-cellular system of non-human primates.

Initial anatomical investigations revealed little in the way of distinctions between cells or areas of mouse dLGN, with no obvious layers or interlaminar zones in mouse dLGN as in cats or primates. More recently, Krahe et al (2013) reconstructed the morphology of a large number of single mouse dLGN cells and found striking similarity in dendritic morphology to the cell types of primates (Saini and Garey, 1981; Nassi and Callaway, 2009) and cats (Friedlander et al., 1981). These authors also saw some bias in the localization of these morphological types, suggesting an organization of mouse dLGN into functional domains: a koniocellular-like dorsal shell, an X-like core, and Y-like morphology the most prevalent the three morphologies. These anatomical data support parallel processing in the mouse and a homology between mice and X/Y/W cells.

Does morphological type correspond to physiological cell type in mouse dLGN, as they do in cats and primates? The few studies of the physiological response properties of mouse dLGN found little evidence for multiple populations of dLGN cells. These studies found mostly linear responses analogous to an X-like or parvocellular-like population, using drifting gratings (Piscopo et al., 2013) or the classical counterphase gratings (Grubb and Thompson, 2003). We find that evidence for multiple conduction velocities in the inputs to mouse V1 and ~10% of single units in mouse dLGN display non-linear spatial summation. Contrast response and spatial and temporal tuning profiles in dLGN measured here support the existence of parallel population in V1 (Gao et al., 2010). The percentage of non-linear cells we observed in mouse dLGN (~10%) is closer to that seen in primates (~12.5%, Kaplan and Shapley, 1982) than cats (~30%, Cleland et

al., 1971). Unlike cat X and Y ganglion cells (Peichl and Wässle, 1979), the distribution of mouse dLGN receptive field size was not bimodal.

Our results suggest mouse dLGN is more homologous to magno/parvo pathways in primates than X/Y pathways in cats. Other recent evidence point towards a functional analog of the koniocellular pathway in mouse dLGN (Huberman et al., 2009; Kay et al., 2011; Krahe et al., 2011; Marshel et al., 2011; Rivlin-Etzion et al., 2011; Piscopo et al., 2013; Scholl et al., 2013). Retinal direction-selective cells project to mouse dLGN (Huberman et al., 2009), targeting a shell area that matches the localization of koniocellular-like morphologies, where direction selective dLGN responses are observed (Marshel et al., 2012; Piscopo et al., 2013). A critical future direction in the classification of mouse dLGN cells is measurement single cell spike latencies to optic chiasm stimulation, a parameters that has been used for classification in both cats and primates (Cleland et al., 1971; Hoffmann et al., 1972; Dreher et al., 1976). Due to the small distance between the optic chiasm and LGN, we had little success in measuring single cell latencies in the mouse. In the future, guided placement of the stimulating electrode, minimal stimulation intensity, and juxtacellular and other single cell recording approaches may facilitate this important measurement.

Corticotgeniculate feedback.

The early mouse visual system also recapitulates corticothalamic organization in other species. Axonal projections arising from V1 layer 6 extend back to dLGN, leaving a collateral in the reticular nucleus and targeting both relay cells and interneurons. These layer 6 cells have two morphologies, each with a layer 4 axon and dendrite. One of these cell types also includes an apical dendrite that extends to layer 1, and an axon that includes a projection to the lateral posterior area of the thalamus. The transgenic mouse line GN220 Ntsr1-Cre specifically labels these CT neurons, making it a useful system for investigating the function of this projection.

We found a mix of effects of Ntsr1 neurons on thalamic responses. When driving this population using ChR2, we always saw a decrease in dLGN spikes, consistent with previous reports in mouse (Olsen et al., 2012), cats (Ahlsen et al., 1985; de Labra et al., 2007), and primates (Hull, 1968). Unexpectedly, removing the activity of this population by hyperpolarization with Arch did not always lead to an increase in spike count: some cells showed an increase, some a decrease, some no change (Chapter 4). This is consistent with several cat studies (Kalil and Chase, 1970; Molotchnikoff et al., 1977; Marrocco et al., 1996). Despite the fact that some groups have argued consistently facilitative (Przybyszewski et al., 2000; Rivadulla et al., 2002) or suppressive (Baker and Malpeli, 1977; Andolina et al., 2007; Olsen et al., 2012) effects of CT axons on dLGN, we show that this pathway is capable of bidirectional modulation of dLGN responsiveness. This modulation is general: it is not spatiotemporally specific. It has been previously argued that the sign of effect is spatially specific (Tsumoto et al., 1978; Andolina et al., 2013). To reconcile these results, future experiments will need to isolate the effects of Ntsr1 cells that are spatially misaligned with their dLGN targets, either through stimuli customized for a single dLGN unit, or through paired recordings of dLGN with isolated Ntsr1 units.

Through what mechanisms do Ntsr1 neuron axons exert their effects on thalamic relay cells? Because of the T-current and thalamic bursting, increases in spike count could result from either depolarization or hyperpolarization. Several approaches could more conclusively address the mechanisms of CG axon effects on relay cells. It is important to know the effect of corticogeniculate axons on other, connected, cells (i.e. interneurons and reticular cells); their activity might shed some insight into the mechanism of corticogenicualte action on relay cells. In addition, recording relay cell membrane potential would be direct measurement of synaptic effects, possibly revealing a mechanism of action. Investigating the membrane potential changes due to Ntsr1-CG cell activity is an active project in the lab (M.M. Taylor & D. Contreras)

One factor that could contribute to the variability of the observed results is the sensitivity of layer 6 cells to brain state (Livingstone and Hubel, 1981; Sherman and Guillery, 1996). Layer 6

is more sensitive to some anesthetics that other cortical cells (Angel and LeBeau, 1992), an effect also observed in our system. It is therefore critical that future studies of layer 6 be performed in awake animals if possible. Beyond anesthesia, other brain states, like states of vigilance or attention, can affect the thalamogeniculate system (Briggs et al., 2013) . Understanding the role of layer 6 in shaping thalamic and V1 responses during may require active behavior context, an approach that may be facilitated by the high throughput behavior in rodents (Meier et al., 2011; Scott et al., 2013).

Synchrony: chance or code?

Near simultaneous activity can engage non-linear readout mechanisms in target neurons. In V1, layer 4 stellate cells are sensitive to the relative timing of thalamic inputs, with up to 40% non-linearity (Cardin et al., 2010a). With two independent, Poisson-like, neurons some activity within the non-linear window will happen by chance. What we observe in V1 is synchrony occurring beyond these levels of chance, more frequency than might be otherwise expected. This type of synchrony can result from input that links a pair of cells, a direct relationship between the cells, or from network mechanisms that produce this kind of synchrony (Aertsen and Gerstein, 1985; Ostojic et al., 2009). However it arises, pairwise synchrony can be regulated independently of firing rate (Person and Raman, 2012; Briggs et al., 2013). This, at minimum, implies that this type of synchrony is not an epiphenomena but a biologically relevant process.

Is synchrony actually used to read out encoded variables in neural systems? The answer to this question is far from obvious. The typical approach to addressing this question involves quantifying the total stimulus information, with and without correlations, either by removing correlations (Dan et al., 1996) or by disregarding them in the readout scheme (Michel and Jacobs, 2006; Pouget et al., 2009; Quian Quiroga and Panzeri, 2009; Eyherabide and Samengo, 2013). Most studies find minimal value for correlations of any timescale (Nirenberg et al., 2003),

133

though some present additional value in synchrony (Dan et al., 1996, Samonds and Bonds, 2003).

These approaches use neural decoders, which are not implementations of neural mechanisms of readout, but rather tools for assessing information content. A description of the neural mechanisms of readout must take into the biophysical properties of synapses, membranes, and spike generation, all of which contain non-linearites that will affect readout of input. On the presynaptic side, synaptic depression is a non-linearity that could affect readout. Postsynaptic specializations can create non-linearities (Yuste, 2013), an idea that dates to Ramon Y Cajal. Dendrites can be linear (Rall, 1962), but also contain active membrane conductances which create complex non-linearities (Major et al., 2013). The presence of a spike threshold rectifies and imposes a high-pass filter (Priebe and Ferster, 2012). Because it is difficult, to impossible, to simultaneously monitor the constellation of inputs to a given cell, and that cell's output, the neural mechanisms of readout are not known. The advent of retrosynaptic viral techniques for tracing neural circuits *in vivo* (Wall et al., 2010; Beier and Cepko, 2012; Osakada and Callaway, 2013) may soon provide a method for addressing these questions.

Noise correlations: epiphenomenon, contaminant, or feature?

Noise correlations are shared variability in spike count independent of changes in spike count due to a stimulus (Cohen and Kohn, 2011). When using a decoder that assumes independence, this type of correlation can degrade the quality of decoding (Nirenberg and Victor, 2007); they also constrain the number of neurons over which it is useful to pool signals for noise removal (Zohary et al., 1994). Even small amounts of pairwise noise correlation imply much greater correlation within a network (Schneidman et al., 2006). This then implies that information loss can actually grow with increasing numbers of neurons (Klam et al., 2008, Oizumi et al., 2010). We found significant, non-zero noise correlation in mouse V1, as in other species, and found that the structure of these noise correlations matched that of other species.

Given the negative implication of noise correlation, why might noise correlation, and its structure, be preserved in systems from mice to primates? It is possible that these correlations are an unavoidable, or at least tolerable, consequence of the number and interconnectivity of neurons using an independent visual encoding and transformation regime. Alternatively, one could speculate that noise correlations are not necessarily detrimental to decoding. In fact, Romo et al (2003) demonstrate conditions in the somatosensory system in which noise correlations can be beneficial. Beneficial noise correlations might also occur in the visual system, at least in the retina (Cafaro and Rieke, 2010). Previous estimates of the effect of correlation on decoding assume independent encoding elements (Nirenberg and Latham, 2003; Eyherabide and Samengo, 2013), but neural systems from the retina to prefrontal cortex violate this assumption of independence (see Cohen and Kohn, 2011). It is possible to construct decoding mechanism that takes dependencies between the encoding elements into account. This type of decoding would require precise wiring, which the results of our functional connectivity measurement, as well as other measures in mouse V1 (Ko et al., 2012), suggest is realistic in the visual system. This type of decoding also opens the door to other forms of noise reduction beyond pooling and normalization, such as estimation of noise terms using correlations (Pouget et al., 2008). Like synchronous activity, the role of noise correlations during neural readout and computation will require measurement of specified input populations in conjunction with the output at their target (Wall et al., 2010; Beier and Cepko, 2012; Osakada and Callaway, 2013).

REFERENCES

Abbott LF, **Dayan P**. The effect of correlated variability on the accuracy of a population code. *Neural Comput* 11: 91–101, 1999.

Acuna-Goycolea C, **Brenowitz SD**, **Regehr WG**. Active Dendritic Conductances Dynamically Regulate GABA Release from Thalamic Interneurons. *Neuron* 57: 420–431, 2008.

Adesnik H, **Bruns W**, **Taniguchi H**, **Huang ZJ**, **Scanziani M**. A neural circuit for spatial summation in visual cortex. *Nature* 490: 226–231, 2012.

Aertsen AMHJ, **Gerstein GL**. Evaluation of neuronal connectivity: Sensitivity of cross-correlation. *Brain Research* 340: 341–354, 1985.

Ahlsén G, **Lindström S**, **Lo F-S**. Interaction between inhibitory pathways to principal cells in the lateral geniculate nucleus of the cat. *Experimental Brain Research* 58: 134–143, 1985.

Alonso JM, **Usrey WM**, **Reid RC**. Precisely correlated firing in cells of the lateral geniculate nucleus. *Nature* 383: 815–819, 1996.

Alonso JM, **Martinez LM**. Functional connectivity between simple cells and complex cells in cat striate cortex. *Nature Neuroscience* 1: 395–403, 1998.

Alvarez JA, **Emory E**. Executive Function and the Frontal Lobes: A Meta-Analytic Review. *Neuropsychol Rev* 16: 17–42, 2006.

Andermann ML, Kerlin AM, Reid RC. Chronic cellular imaging of mouse visual cortex during operant behavior and passive viewing. *Front. Cell. Neurosci.*, 4:3, 2010.

Andolina IM, **Jones HE**, **Sillito AM**. Effects of cortical feedback on the spatial properties of relay cells in the lateral geniculate nucleus. *J Neurophysiol* 109: 889–899, 2013.

Andolina IM, **Jones HE**, **Wang W**, **Sillito AM**. Corticothalamic feedback enhances stimulus response precision in the visual system. *PNAS.* 104: 1685–1690, 2007.

Angel A, **LeBeau F**. A comparison of the effects of propofol with other anaesthetic agents on the centripetal transmission of sensory information. *General Pharmacology: The Vascular System* 23: 945–963, 1992.

Atallah BV, **Bruns W**, **Carandini M**, **Scanziani M**. Parvalbumin-Expressing Interneurons Linearly Transform Cortical Responses to Visual Stimuli. *Neuron* 73: 159–170, 2012.

Atasoy D, **Aponte Y**, **Su HH**, **Sternson SM**. A FLEX Switch Targets Channelrhodopsin-2 to Multiple Cell Types for Imaging and Long-Range Circuit Mapping. *Journal of Neuroscience* 28: 7025–7030, 2008.

Averbeck BB. Effects of Noise Correlations on Information Encoding and Decoding. *J Neurophysiol.* 95:3633–3644, 2006

Averbeck BB, Latham PE, Pouget A. Neural correlations, population coding and computation. *Nature Reviews Neuroscience.* 7:358–366, 2006

Badea A, **Ali-Sharief AA**, **Johnson GA**. Morphometric analysis of the C57BL/6J mouse brain. *NeuroImage* 37: 683–693, 2007.

Bair W, Zohary E, Newsome WT. Correlated firing in macaque visual area MT: time scales and relationship to behavior. *Journal of Neuroscience.* 21:1676–1697, 2001.

Baker FH, **Malpeli JG**. Effects of cryogenic blockade of visual cortex on the responses of lateral geniculate neurons in the monkey. *Experimental Brain Research* 29:433-444, 1977

Baker M. Neuroscience: Through the eyes of a mouse. *Nature* 502: 156–158, 2013.

Balkema GW Jr, Pinto LH. Electrophysiology of retinal ganglion cells in the mouse: a study of a normally pigmented mouse and a congenic hypopigmentation mutant, pearl *J Neurophysiol* 48(4):968-80, 1982.

Bartfeld E, **Grinvald A**. Relationships between orientation-preference pinwheels, cytochrome oxidase blobs, and ocular-dominance columns in primate striate cortex. *PNAS* 89: 11905–11909, 1992.

Beier K, **Cepko C**. Viral Tracing of Genetically Defined Neural Circuitry. *JoVE* : e4253–e4253, 2012.

Bernstein JG, **Boyden ES**. Optogenetic tools for analyzing the neural circuits of behavior. *Trends in Cognitive Sciences* 15: 592–600, 2011.

Bishop PO, **McLeod JG**. Nature of potentials associated with synaptic transmission in lateral geniculate of cat. *J Neurophysiol.* 17(4):387-414, 1954.

Bishop PO, **Burke W**, **Davis R**. Activation of Single Lateral Geniculate Cells by Stimulation of Either Optic Nerve. *Science* 130: 506–507, 1959.

Blitz DM, **Regehr WG**. Timing and Specificity of Feed-Forward Inhibition within the LGN. *Neuron* 45: 917–928, 2005.

Blitz DM, Regehr WG. Retinogeniculate Synaptic Properties Controlling Spike Number and Timing in Relay Neurons. *J Neurophysiol* 90: 2438–2450, 2003.

Bock DD, **Lee W-CA**, **Kerlin AM**, **Andermann ML**, **Hood G**, **Wetzel AW**, **Yurgenson S**, **Soucy ER**, **Kim HS**, **Reid RC**. Network anatomy and in vivo physiology of visual cortical neurons. *Nature* 471: 177–182, 2012.

Bohte SM. The evidence for neural information processing with precise spike-times: A survey. *Natural Computing* 3: 195–206, 2004.

Bonin V, **Histed MH**, **Yurgenson S**, **Reid RC**. Local diversity and fine-scale organization of receptive fields in mouse visual cortex. *Journal of Neuroscience* 31: 18506–18521, 2011.

Bosking WH, Zhang Y, Schofield B, Fitzpatrick D. Orientation selectivity and the arrangement of horizontal connections in tree shrew striate cortex. *The Journal of Neuroscience.* 17:2112–2127, 1997

Bourassa J, Deschenes M. Corticothalamic projections from the primary visual cortex in rats: a single fiber study using biocytin as an anterograde tracer. *Neuroscience*, 66(2):253-63, 1995.

Briggs F, Usrey WM. Emerging views of corticothalamic function. *Current Opinion in Neurobiology* 18: 403–407, 2008

Briggs F, **Usrey WM**. Parallel Processing in the Corticogeniculate Pathway of the Macaque Monkey. *Neuron* 62: 135–146, 2009.

Briggs F. Organizing principles of cortical layer 6. *Front. Neural Circuits* 4:3, 2010.

Briggs F, **Mangun GR**, **Usrey WM**. Attention enhances synaptic efficacy and the signal-to-noise ratio in neural circuits. *Nature* 499(7459):476-80, 2013.

Bringuier V, Chavane F, Glaeser L, Frégnac Y. Horizontal propagation of visual activity in the synaptic integration field of area 17 neurons. *Science.* 283:695–699, 1999

Brown VJ, **Bowman EM**. Rodent models of prefrontal cortical function. *Trends in Neurosciences* 25: 340–343, 2002.

Bruno RM, Sakmann B. Cortex Is Driven by Weak but Synchronously Active Thalamocortical Synapses. *Science.* 312:1622–1627, 2006.

Busse L, **Ayaz A**, **Dhruv NT**, **Katzner S**, **Saleem AB**, **Schölvinck ML**, **Zaharia AD**, **Carandini M**. The detection of visual contrast in the behaving mouse. *Journal of Neuroscience* 31: 11351–11361, 2011.

Buzsáki G, **Anastassiou CA**, **Koch C**. The origin of extracellular fields and currents — EEG, ECoG, LFP and spikes. *Nat Rev. Neurosci.* 13(6): 407-420, 2012.

Cafaro J, **Rieke F**. Noise correlations improve response fidelity and stimulus encoding. *Nature* 468(7326):964-7, 2010.

Callaway EM. Local circuits in primary visual cortex of the macaque monkey. *Annu. Rev. Neurosci.* 21: 47–74, 1998.

Carandini M, **Churchland AK**. Probing perceptual decisions in rodents. *Nature Neuroscience* 16: 824–831, 2013.

Carandini M, **Heeger DJ, Movshon JA**. Linearity and normalization in simple cells of the macaque primary visual cortex. *Journal of Neuroscience* 17(21):8621-44, 1997

Carandini M, **Heeger DJ**. Normalization as a canonical neural computation. *Nat Rev Neurosci* 13(1):51-62, 2011

Cardin JA, **Carlén M**, **Meletis K**, **Knoblich U**, **Zhang F**, **Deisseroth K**, **Tsai L-H**, **Moore CI**. Driving fast-spiking cells induces gamma rhythm and controls sensory responses. *Nature* 459:663-7, 2009.

Cardin JA, **Kumbhani RD**, **Contreras D**, **Palmer LA**. Cellular Mechanisms of Temporal Sensitivity in Visual Cortex Neurons. *Journal of Neuroscience* 30: 3652–3662, 2010a.

Cardin JA, **Carlen M**, **Meletis K**, **Knoblich U**, **Zhang F**, **Deisseroth K**, **Tsai L-H**, **Moore CI**. Targeted optogenetic stimulation and recording of neurons in vivo using cell-type-specificexpression of Channelrhodopsin-2. *Nature Protocols* 5: 247–254, 2010b.

Cardin JA. Dissecting local circuits in vivo: Integrated optogenetic and electrophysiology

approaches for exploring inhibitory regulation of cortical activity. *Journal of Physiology-Paris* 106: 104–111, 2012.

Ch'Ng YH, Reid RC. Cellular imaging of visual cortex reveals the spatial and functional organization of spontaneous activity. *Front Integr Neurosci.* 4:1–9, 2010

Chen C, **Regehr WG**. Developmental remodeling of the retinogeniculate synapse. *Neuron*, 28(3):955-66, 2000.

Chen C, **Regehr WG**. Presynaptic modulation of the retinogeniculate synapse. *Journal of Neuroscience* 23: 3130–3135, 2003.

Chia TH, Levene MJ. Microprisms for in vivo multilayer cortical imaging. *J Neurophysiol.* 102(2):1310-4, 2009.

Chklovskii DB, **Schikorski T**, **Stevens CF**. Wiring Optimization in Cortical Circuits. *Neuron* 34: 341–347, 2002.

Chouinard PA. The primary motor and premotor areas of the human cerebral cortex. *Neuroscientist* 12: 143–152, 2006.

Chow BY, **Han X**, **Dobry AS**, **Qian X**, **Chuong AS**, **Li M**, **Henninger MA**, **Belfort GM**, **Lin Y**, **Monahan PE**, **Boyden ES**. High-performance genetically targetable optical neural silencing by light-driven proton pumps. *Nature* 463: 98–102, 2010.

Clandinin TR, **Feldheim DA**. Making a visual map: mechanisms and molecules. *Current Opinion in Neurobiology* 19: 174–180, 2009.

Cleland BG, **Dubin MW**, **Levick WR**. Sustained and transient neurones in the cat's retina and lateral geniculate nucleus. *J Physiol* 217: 473–496, 1971.

Cohen MR, **Kohn A**. Measuring and interpreting neuronal correlations. *Nature Neuroscience* 14: 811–819, 2011.

Cohen MR, **Maunsell JHR**. Attention improves performance primarily by reducing interneuronal correlations. *Nature Neuroscience* 12: 1594–1600, 2009.

Contreras D, Steriade M. Spindle oscillation in cats: the role of corticothalamic feedback in a thalamically generated rhythm. *J Physiol.* 490 (1):159-79, 1996.

Crunelli V, **Kelly JS**, **Leresche N**. On the excitatory post-synaptic potential evoked by stimulation of the optic tract in the rat lateral geniculate nucleus. *J Physiol* 384:603-18, 1987.

Dacey D. Physiology, morphology and spatial densities of identified ganglion cell types in primate retina. *Ciba Foundation Symposium* 184:12-28, 1994

Dan Y, **Alonso JM**, **Usrey WM**, **Reid RC**. Coding of visual information by precisely correlated spikes in the lateral geniculate nucleus. *Nature Neuroscience* 1: 501–507, 1998.

de Labra C, **Rivadulla C**, **Grieve K**, **Marino J**. Changes in visual responses in the feline dLGN: selective thalamic suppression induced by transcranial magnetic stimulation of V1. *Cerebral Cortex* 17(6):1376-85, 2007.

de Monasterio FM, Gouras P. Functional properties of ganglion cells of the rhesus monkey retina *J Physiol* 251(1):167-95, 1975.

Deneve S, **Latham PE**, **Pouget A**. Reading population codes: a neural implementation of ideal observers. *Nature Neuroscience* 2: 740–745, 1999.

Denman DJ, Contreras D. The Structure of Pairwise Correlation in Mouse Primary Visual Cortex Reveals Functional Organization in the Absence of an Orientation Map. *Cerebral Cortex* Epub ahead of print, May 19 2013

Diester I, **Kaufman MT**, **Mogri M**, **Pashaie R**, **Goo W**, **Yizhar O**, **Ramakrishnan C**, **Deisseroth K**, **Shenoy KV**. An optogenetic toolbox designed for primates. *Nature Neuroscience* 14: 387–397, 2011.

Dombeck DA, **Khabbaz AN**, **Collman F**, **Adelman TL**, **Tank DW**. Imaging Large-Scale Neural Activity with Cellular Resolution in Awake, Mobile Mice. *Neuron* 56: 43–57, 2007.

Douglas RJ, **Martin KAC**. Mapping the Matrix: The Ways of Neocortex. *Neuron* 56: 226–238, 2007.

Drager UC. Receptive fields of single cells and topography in mouse visual cortex *Journal of Comparative Neurology* 160(3):269-90.1974

Drager UC, **Hubel DH**. Physiology of visual cells in mouse superior colliculus and correlation with somatosensory and auditory input. *Nature* 253: 203–204, 1975.

Dreher B, **Fukada Y**, **Rodieck RW**. Identification, classification and anatomical segregation of cells with X-like and Y-like properties in the lateral geniculate nucleus of old-world primates. *J Physiol* 258: 433–452, 1976.

Drescher U, **Bonhoeffer F**, **Müller BK**. The Eph family in retinal axon guidance. *Current Opinion in Neurobiology* 7: 75–80, 1997.

Dunlop SA, **Lund RD**, **Beazley LD**. Segregation of optic input in a three-eyed mammal. *Exp. Neurol.* 137: 294–298, 1996.

Ecker AS, **Berens P**, **Keliris GA**, **Bethge M**, **Logothetis NK**, **Tolias AS**. Decorrelated Neuronal Firing in Cortical Microcircuits. *Science* 327: 584–587, 2010.

Einevoll GT, **Kayser C**, **Logothetis NK**, **Panzeri S**. Modelling and analysis of local field potentials for studying the function of cortical circuits. *Nat Rev Neurosci* 14: 770–785, 2013.

Enroth-Cugell C, **Robson JG**. The contrast sensitivity of retinal ganglion cells of the cat. *J Physiol* 87(3):517-52, 1966.

Erişir A, **Van Horn SC**, **Sherman SM**. Relative numbers of cortical and brainstem inputs to the lateral geniculate nucleus. *PNAS.* 94: 1517–1520, 1997.

Eyherabide HG, **Samengo I**. When and Why Noise Correlations Are Important in Neural Decoding. *Journal of Neuroscience* 33: 17921–17936, 2013.

Fenno L, **Yizhar O**, **Deisseroth K**. The Development and Application of Optogenetics. *Annual Rev. Neurosci.* 34: 389–412, 2011.

Friedlander MJ, **Lin CS**, **Stanford LR, Sherman SM**. Morphology of functionally identified neurons in lateral geniculate nucleus of the cat. *J Neurophysiol* 46(1):80-129, 1981

Funke K, Nelle E, Li B, Worgotter F. Corticofugal feedback improves the timing of retino-geniculate signal transmission. *Neuroreport.* 7(13):2130-4, 1996.

Gao E, **DeAngelis GC**, **Burkhalter A**. Parallel Input Channels to Mouse Primary Visual Cortex. *Journal of Neuroscience* 30: 5912–5926, 2010.

Gawne TJ, **Richmond BJ**. Interactive effects among several stimulus parameters on the responses of striate cortical complex cells. *J Neurophysiol* 66(2):379-89, 1991

Gawne TJ, **Richmond BJ**. How independent are the messages carried by adjacent inferior temporal cortical neurons? *Journal of Neuroscience* 13(7):2758-71, 1993.

Gerits A, **Farivar R**, **Rosen BR**, **Wald LL**, **Boyden ES**, **Vanduffel W**. Optogenetically Induced Behavioral and Functional Network Changes in Primates. *Current Biology* 22: 1722–1726, 2012.

Gerstein GL, **Perkel DH**, **Dayhoff JE**. Cooperative firing activity in simultaneously recorded populations of neurons: detection and measurement. *Journal of Neuroscience* 5: 881–889, 1985.

Gilbert CD, Wiesel TN. Columnar specificity of intrinsic horizontal and corticocortical connections in cat visual cortex. *The Journal of Neuroscience.* 9:2432-2442, 1989

Glickfeld LL, **Andermann ML**, **Bonin V**, **Reid RC**. Cortico-cortical projections in mouse visual cortex are functionally target specific. *Nature Neuroscience* 16: 219–226, 2013.

Goard M, Dan Y. Basal forebrain activation enhances cortical coding of natural scenes *Nature Neuroscience* 12(11):1444-9, 2009

Gong S, **Doughty M**, **Harbaugh CR**, **Cummins A**, **Hatten ME**, **Heintz N**, **Gerfen CR**. Targeting Cre Recombinase to Specific Neuron Populations with Bacterial Artificial Chromosome Constructs. *Journal of Neuroscience* 27: 9817–9823, 2007.

Gong S, **Zheng C**, **Doughty ML**, **Losos K**, **Didkovsky N**, **Schambra UB**, **Nowak NJ**, **Joyner A**, **Leblanc G**, **Hatten ME**, **Heintz N**. A gene expression atlas of the central nervous system based on bacterial artificial chromosomes. *Nature* 425: 917–925, 2003.

Gouras P. Antidromic responses of orthodromically identified ganglion cells in monkey retina. *J Physiol* 204(2):407-19, 1969.

Gradinaru V, **Mogri M**, **Thompson KR**, **Henderson JM**, **Deisseroth K**. Optical deconstruction of parkinsonian neural circuitry. *Science* 324: 354–359, 2009.

Gross, C. Brai, VIsion, and Memory: Tales in the HIstory of Neuroscience. A Bradford Book, MIT Press, Boston, MA, 1999

Grubb MS, Thompson ID. Quantitative Characterization of Visual Response Properties in the Mouse Dorsal Lateral Geniculate Nucleus. *J Neurophysiol* 90: 3594–3607, 2003.

Grubb MS, Thompson ID. Visual Response Properties in the Dorsal Lateral Geniculate Nucleus of Mice Lacking the beta2 Subunit of the Nicotinic Acetylcholine Receptor. *Journal of Neuroscience* 24: 8459–8469, 2004.

Guido W, Weyand T. Burst responses in thalamic relay cells of the awake behaving cat. *J Neurophysiol* 74(4):1782-6, 1995.

Gulyas B, Lagae L, Eysel U, Orban GA. Corticofugal feedback influences the responses of geniculate neurons to moving stimuli. *Experimental Brain Research* 79(2):441-6, 1990

Haider B, Krause MR, Duque A, Yu Y, Touryan J, Mazer JA, McCormick DA. Synaptic and Network Mechanisms of Sparse and Reliable Visual Cortical Activity during Nonclassical Receptive Field Stimulation. *Neuron.* 65:107–121, 2010

Hale PT, Sefton AJ, Dreher B. A correlation of receptive field properties with conduction velocity of cells in the rat's retino-geniculo-cortical pathway *Experimental Brain Research* 35(3):425-42, 1979.

Hawken MJ, Shapley RM, Grosof DH. Temporal-frequency selectivity in monkey visual cortex *Visual Neuroscience* 13(3):477-92, 1996.

Hansel D, **van Vreeswijk C**. The Mechanism of Orientation Selectivity in Primary Visual Cortex without a Functional Map. *Journal of Neuroscience* 32: 4049–4064, 2012.

Harris KD. Neural signatures of cell assembly organization. *Nature Reviews Neuroscience.* 6:399–407, 2005.

Heekeren HR, **Marrett S**, **Ungerleider LG**. The neural systems that mediate human perceptual decision making. *Nat Rev Neurosci* 9: 467–479, 2008.

Hendry SH, Reid RC. The koniocellular pathway in primate vision. *Annual Rev Neurosci.* 23:127-53, 2000.

Herculano-Houzel S, **Collins CE**, **Wong P**, **Kaas JH**, **Lent R**. The basic nonuniformity of the cerebral cortex. *PNAS* 105: 12593–12598, 2008.

Herculano-Houzel S, **Watson C**, **Paxinos G**. Distribution of neurons in functional areas of the mouse cerebral cortex reveals quantitatively different cortical zones. *Front. Neuroanat.* 7: 35, 2013.

Hirsch JA, **Martinez LM**. Laminar processing in the visual cortical column. *Current Opinion in Neurobiology* 16: 377–384, 2006.

Hochstein S, Shapley RM. Linear and nonlinear spatial subunits in Y cat retinal ganglion cells *J Phsyiol.* 262(2):265-84, 1976.

Hofer SB, **Ko H**, **Pichler B**, **Vogelstein J**, **Ros H**, **Zeng H**, **Lein E**, **Lesica NA**, **Mrsic-Flogel TD**. Differential connectivity and response dynamics of excitatory and inhibitory neurons in visual cortex. *Nature Neuroscience* 14: 1045–1052, 2011.

Hoffmann KP, **Stone J**, **Sherman SM**. Relay of receptive-field properties in dorsal lateral geniculate nucleus of the cat. *J Neurophysiol.* 35(4):518-31, 1972.

Horwitz GD, **Chichilnisky EJ**, **Albright TD**. Cone Inputs to Simple and Complex Cells in V1 of Awake Macaque. *J Neurophysiol* 97: 3070–3081, 2007.

Horwitz GD, **Hass CA**. Nonlinear analysis of macaque V1 color tuning reveals cardinal directions for cortical color processing. *Nature Neuroscience* 15: 913–919, 2012.

Hubel DH, **Wiesel TN**. Receptive fields of single neurones in the cat's striate cortex. *J Physiol.*, 148:574-91, 1959

Hubel DH, **Wiesel TN**. Receptive fields, binocular interaction and functional architecture in the cat's visual cortex. *J Physiol* 160: 106–154, 1962.

Hubel DH, **Wiesel TN**. Receptive fields and functional architecture of monkey striate cortex. *J Physiol* 195: 215–243, 1968.

Huberman AD, **Niell CM**. What can mice tell us about how vision works? *Trends in Neurosciences* 34: 464–473, 2011.

Huberman AD, **Wei W**, **Elstrott J**, **Stafford BK**, **Feller MB**, **Barres BA**. Genetic identification of an On-Off direction-selective retinal ganglion cell subtype reveals a layer-specific subcortical map of posterior motion. *Neuron* 62: 327–334, 2009.

Hull EM. Corticofugal influence in the macaque lateral geniculate nucleus. *Vision Research* 8: 1285–1298, 1968.

Jazayeri M, **Lindbloom-Brown Z**, **Horwitz GD**. Saccadic eye movements evoked by optogenetic activation of primate V1. *Nature Publishing Group* 15: 1368–1370, 2012.

Jia H, **Rochefort NL**, **Chen X**, **Konnerth A**. Dendritic organization of sensory input to cortical neurons in vivo. *Nature* 464: 1307–1312, 2010.

Jin L, **Han Z**, **Platisa J**, **Wooltorton JRA**, **Cohen LB**, **Pieribone VA**. Single Action Potentials and Subthreshold Electrical Events Imaged in Neurons with a Fluorescent Protein Voltage Probe. *Neuron* 75: 779–785, 2012.

Johnson KO. Sensory discrimination: decision process. *Journal of Neurophysiology.* 43(6):1771-92,1980

Jones E. The Thalamus, Volume 2. Cambridge University Press, Cambridge, UK, 2007

Josten NJ, **Huberman AD**. Milestones and mechanisms for generating specific synaptic connections between the eyes and the brain. *Curr. Top. Dev. Biol.* 93: 229–259, 2010.

Jurgens CWD, **Bell KA**, **McQuiston AR**, **Guido W**. Optogenetic stimulation of the corticothalamic pathway affects relay cells and GABAergic neurons differently in the mouse visual thalamus. *PLoS ONE* 7: e45717, 2012.

Kalil RE, **Chase R**. Corticofugal influence on activity of lateral geniculate neurons in the cat. *J Neurophysiol* 33: 459–474, 1970.

Kalatsky VA, Stryker MP. New paradigm for optical imaging: temporally encoded maps of intrinsic signal. Neuron. 38:529–545, 2003.

Kaplan E, **Shapley RM**. X and Y cells in the lateral geniculate nucleus of macaque monkeys. *J Physiol.* 330:125-43, 1982

Kaplan E, **Shapley RM**. The primate retina contains two types of ganglion cells, with high and low contrast sensitivity. *PNAS* 83: 2755–2757, 1986.

Kay JN, **la Huerta De I**, **Kim I-J**, **Zhang Y**, **Yamagata M**, **Chu MW**, **Meister M**, **Sanes JR**. Retinal Ganglion Cells with Distinct Directional Preferences Differ in Molecular Identity, Structure, and Central Projections. *Journal of Neuroscience* 31: 7753–7762, 2011.

Kayama Y, **Shosaku A**, **Doty RW**. Cryogenic blockade of the visual cortico-thalamic projection in the rat. *Experimental Brain Research* 54: 157–165, 1984.

Kerlin AM, **Andermann ML**, **Berezovskii VK**, **Reid RC**. Broadly Tuned Response Properties of Diverse Inhibitory Neuron Subtypes in Mouse Visual Cortex. *Neuron* 67: 858–871, 2010.

Kimberg DY, **Farah MJ**. A unified account of cognitive impairments following frontal lobe damage: The role of working memory in complex, organized behavior. *Journal of Experimental Psychology: General* 122: 411–428, 1993.

Klam F, Zemel RS, Pouget A. Population coding with motion energy filters: the impact of correlations. *Neural Computation* 20(1):146-75, 2008.

Ko H, **Hofer SB**, **Pichler B**, **Buchanan KA**, **Sjöström PJ**, **Mrsic-Flogel TD**. Functional specificity of local synaptic connections in neocortical networks. *Nature* 473: 87–91, 2012.

Kohn A, **Smith MA** Stimulus Dependence of Neuronal Correlation in Primary Visual Cortex of the Macaque. *Journal of Neuroscience* 25: 3661–3673, 2005.

Koulakov AA, **Chklovskii DB**. Orientation Preference Patterns in Mammalian Visual Cortex. *Neuron* 29: 519–527, 2001.

Krahe TE, **El-Danaf RN**, **Dilger EK**, **Henderson SC**, **Guido W**. Morphologically Distinct Classes of Relay Cells Exhibit Regional Preferences in the Dorsal Lateral Geniculate Nucleus of the Mouse. *Journal of Neuroscience* 31: 17437–17448, 2011.

Kravitz AV, **Freeze BS**, **Parker PRL**, **Kay K**, **Thwin MT**, **Deisseroth K**, **Kreitzer AC**. Regulation of parkinsonian motor behaviours by optogenetic control of basal ganglia circuitry. *Nature* 466: 622–626, 2010.

Kriegs JO, **Churakov G**, **Kiefmann M**, **Jordan U**, **Brosius J**, **Schmitz J**. Retroposed Elements as Archives for the Evolutionary History of Placental Mammals. *Plos Biol* 4: e91, 2006.

Kruger J, **Aiple F**. Multimicroelectrode investigation of monkey striate cortex: spike train correlations in the infragranular layers. *J Neurophysiol.* 60(2):798-828, 1988

Kumbhani RD, **Nolt MJ**, **Palmer LA**. Precision, reliability, and information-theoretic analysis of visual thalamocortical neurons. *J Neurophysiol* 98: 2647–2663, 2007.

Kurimoto T, **Yin Y**, **Omura K**, **Gilbert H-Y**, **Kim D**, **Cen L-P**, **Moko L**, **Kügler S**, **Benowitz LI**. Long-distance axon regeneration in the mature optic nerve: contributions of oncomodulin, cAMP, and pten gene deletion. *Journal of Neuroscience* 30: 15654–15663, 2010.

la Rocha de J, **Doiron B**, **Shea-Brown E**, **Josić K**, **Reyes A**. Correlation between neural spike trains increases with firing rate. *Nature* 448: 802–806, 2007.

Law C-T, Gold JI. Reinforcement learning can account for associative and perceptual learning on a visual-decision task. *Nature Neuroscience* 12: 655 - 663, 2009.

Lee S-H, **Kwan AC**, **Zhang S**, **Phoumthipphavong V**, **Flannery JG**, **Masmanidis SC**, **Taniguchi H**, **Huang ZJ**, **Zhang F**, **Boyden ES**, **Deisseroth K**, **Dan Y**. Activation of specific interneurons improves V1 feature selectivity and visual perception. *Nature* 488: 379–383, 2012.

LeVay S, Ferster D. Relay cell classes in the lateral geniculate nucleus of the cat and the effects of visual deprivation. *J Comp Neurol* 172(4):563-84, 1977.

Leventhal AG, **Rodieck RW**, **Dreher B**. Retinal ganglion cell classes in the Old World monkey: morphology and central projections. *Science* 213(4512):1139-42, 1981.

Li L, Ebner FF. Cortical modulation of spatial and angular tuning maps in the rat thalamus *Journal of Neuroscience* 27(1):167-79, 2007.

Liu B-H, **Li P**, **Sun YJ**, **Li Y-T**, **Zhang LI**, **Tao HW**. Intervening inhibition underlies simple-cell receptive field structure in visual cortex. *Nature Neuroscience* 13: 89–96, 2009.

Liu B-H, **Li Y-T**, **Ma W-P**, **Pan C-J**, **Zhang LI**, **Tao HW**. Broad Inhibition Sharpens Orientation Selectivity by Expanding Input Dynamic Range in Mouse Simple Cells. *Neuron* 71: 542–554, 2011.

Livingstone M, Hubel D. Effects of sleep and arousal on the processing of visual information in the cat. *Nature* 291(5816):554-61, 1981.

Livingstone M, **Hubel D**. Segregation of form, color, movement, and depth: anatomy, physiology, and perception. *Science* 240: 740–749, 1988.

Long MA, **Jin DZ**, **Fee MS**. Support for a synaptic chain model of neuronal sequence generation. *Nature* 468: 394–399, 2011.

Madisen L, Zwingman TA, Sunkin SM, Oh SW, Zariwala HA, Gu H, Ng LL, Palmiter RD, Hawrylycz MJ, Jones AR, Lein ES, Zeng H. A robust and high-throughput Cre reporting and characterization system for the whole mouse brain. *Nature Neuroscience* 13: 133–140, 2009.

Madisen L, **Mao T**, **Koch H**, **Zhuo J-M**, **Berenyi A**, **Fujisawa S**, **Hsu Y-WA**, **Garcia AJ**, **Gu X**, **Zanella S**, **Kidney J**, **Gu H**, **Mao Y**, **Hooks BM**, **Boyden ES**, **Buzsáki G**, **Ramirez JM**, **Jones AR**, **Svoboda K**, **Han X**, **Turner EE**, **Zeng H**. A toolbox of Cre-dependent optogenetic transgenic mice for light-induced activation and silencing. *Nature Neuroscience* 15: 793–802, 2012.

Major G, **Larkum ME**, **Schiller J**. Active Properties of Neocortical Pyramidal Neuron Dendrites. *Annual Rev Neurosci.* 36: 1–24, 2013.

Malach R, Amir Y, Harel M, Grinvald A. Relationship between intrinsic connections and functional architecture revealed by optical imaging and in vivo targeted biocytin injections in primate striate cortex. *Proceedings of the National Academy of Sciences.* 90:10469–10473, 1993

Marrocco RT, **McClurkin JW, Young RA**. Modulation of lateral geniculate nucleus cell responsiveness by visual activation of the corticogeniculate pathway. *Journal of Neuroscience* 2(2):256-63, 1982

Marrocco RT, **McClurkin JW**. Evidence for spatial structure in the cortical input to the monkey lateral geniculate nucleus. *Experimental Brain Research* 59(1):50-6, 1985.

Marrocco RT, McClurkin JW, Alkire MT. The influence of the visual cortex on the spatiotemporal response properties of lateral geniculate nucleus cells. *Brain Research* 737(1-2):110-8, 1996

Marshel JH, **Garrett ME**, **Nauhaus I**, **Callaway EM**. Functional Specialization of Seven Mouse Visual Cortical Areas. *Neuron* 72: 1040–1054, 2011.

Marshel JH, **Kaye AP**, **Nauhaus I**, **Callaway EM**. Anterior-Posterior Direction Opponency in the Superficial Mouse Lateral Geniculate Nucleus. *Neuron* 76: 713–720, 2012.

Martinez LM, **Wang Q**, **Reid RC**, **Pillai C**, **Alonso J-M**, **Sommer FT**, **Hirsch JA**. Receptive field structure varies with layer in the primary visual cortex. *Nature Neuroscience* 8: 372–379, 2005.

Masland RH. The Neuronal Organization of the Retina. *Neuron* 76: 266–280, 2012.

Hansel D, van Vreeswijk, C. The mechanism of orientation selectivity in primary visual cortex without a functional map. *Journal of Neuroscience.* 32(12):4049-64, 2012.

Harrison MT, Geman S. A Rate and History-Preserving Resampling Algorithm for Neural Spike Trains. *Neural Comput* 21: 1244–1258, 2009.

McClurkin JW, **Gawne TJ**, **Richmond BJ**, **Optican LM**, **Robinson DL**. Lateral geniculate neurons in behaving primates. I. Responses to two-dimensional stimuli. *J Neurophysiol* 66: 777–793, 1991.

McCormick DA, **Pape HC**. Properties of a hyperpolarization-activated cation current and its role in rhythmic oscillation in thalamic relay neurones. *J Physiol.* 431:291-318, 1990

McCormick DA, **Krosigk von M**. Corticothalamic activation modulates thalamic firing through glutamate "metabotropic" receptors. *PNAS* 89: 2774–2778, 1992.

McCormick DA, Contreras D. On the cellular and network bases of epileptic seizures *Annual Rev. Physiol.* 63:815-46, 2001.

McGuire BA, Hornung JP, GIlbert CD, Wiesel TN Patterns of synaptic input to layer 4 of cat striate cortex. *Journal of Neuroscience* 4(12):3021-33, 1984

McLaughlin D, Shapley R, Shelley M. Large-scale modeling of the primary visual cortex: influence of cortical architecture upon neuronal response. *Journal of Physiology-Paris.* 97:237–252, 2003

McClurkin JW, Optican LM, Richmond BJ. Cortical feedback increases visual information transmitted by monkey parvocellular lateral geniculate nucleus neurons.*Visual Neuroscience* 11(3):601-17, 1994

Meier P, **Flister E**, **Reinagel P**. Collinear features impair visual detection by rats. *Journal of Vision* 11: 22–22, 2011.

Michel MM, Jacobs RA. The costs of ignoring high-order correlations in populations of model neurons. *Neural Computation* 18(3):660-82, 2006.

Molotchnikoff S, Lachapelle P. Corticofugal influence on evoked activity of lateral geniculate neurons in the rabbit. *Experimental Brain Research* 29(3-4):527-30, 1977

Molotchnikoff S, **Delaunais D**, **Casanova C**. Modulations of the lateral geniculate nucleus cell responses by a second discrete conditioning stimulus: implications of the superior colliculus in rabbits. *Experimental Brain Research* 62: 321–328, 1986.

Mountcastle VB. The columnar organization of the neocortex. *Brain.* 120 (4):701-22,1997

Movshon, JA, 2013. "Functional models and functional organisms for systems neuroscience". Talk, Cosyne, March 3, 2013, Salt Lake City, UT.

Murphy PC, Sillito AM. Corticofugal feedback influences the generation of length tuning in the visual pathway. *Nature* 329(6141):727-9, 1987

Murphy PC, Sillito AM. The modulation of the retinal relay to the cortex in the dorsal lateral geniculate nucleus. *Eye,* 2 Suppl:S221-32, 1988

Murphy PC, Duckett SG, Sillito AM Feedback connections to the lateral geniculate nucleus and cortical response properties. *Science* 286(5444):1552-4, 1999.

Nassi JJ, **Callaway EM**. Parallel processing strategies of the primate visual system. *Nat Rev Neurosci* 10: 360–372, 2009.

Nathanson JL, **Yanagawa Y**, **Obata K**, **Callaway EM**. Preferential labeling of inhibitory and excitatory cortical neurons by endogenous tropism of adeno-associated virus and lentivirus vectors. *Neuroscience* 161: 441–450, 2009.

Nettleton JS, Spain WJ. Linear to supralinear summation of AMPA-mediated EPSPs in neocortical pyramidal neurons. J Neurophysiol. 83:3310–3322, 2000.

Niell CM, **Stryker MP**. Highly Selective Receptive Fields in Mouse Visual Cortex. *Journal of Neuroscience* 28: 7520–7536, 2008.

Niell CM, **Stryker MP**. Modulation of Visual Responsesby Behavioral State in Mouse Visual Cortex. *Neuron* 65: 472–479, 2010.

Niell CM. Exploring the Next Frontier of Mouse Vision. *Neuron* 72: 889–892, 2011.

Nirenberg S, Carcieri SM, Jacobs AL, Latham PE. Retinal ganglion cells act largely as independent encoders. *Nature.* 411:698–701, 2001.

Nirenberg S, **Latham PE**. Decoding neuronal spike trains: how important are correlations? *PNAS.* 100: 7348–7353, 2003.

Nirenberg SH, **Victor JD**. Analyzing the activity of large populations of neurons: how tractable is the problem? *Current Opinion in Neurobiology* 17: 397–400, 2007.

Ohki K, **Chung S**, **Ch'ng YH**, **Kara P**, **Reid RC**. Functional imaging with cellular resolution reveals precise micro-architecture in visual cortex. *Nature* 433: 597–603, 2005.

Ohki K, **Chung S**, **Kara P**, **Hübener M**, **Bonhoeffer T**, **Reid RC**. Highly ordered arrangement of single neurons in orientation pinwheels. *Nature* 442: 925–928, 2006.

Ohki K, **Reid RC**. Specificity and randomness in the visual cortex. *Current Opinion in Neurobiology* 17: 401–407, 2007.

Oizumi M, Ishii T, Ishibashi, K, Hosoua Y, Okada M. Mismatched decoding in the brain. *Journal of Neuroscience* 30(13):4815-26, 2010.

Olsen SR, **Bortone DS**, **Adesnik H**, **Scanziani M**. Gain control by layer six in cortical circuits of vision. *Nature* 4 83(7387):47-52, 2012

Olshausen BA, **Field DJ**. How Close Are We to Understanding V1? *Neural Comput.* 17: 1665–1699, 2006.

Osakada F, **Callaway EM**. Design and generation of recombinant rabies virus vectors. *Nature Protocols* 8: 1583–1601, 2013.

Ostojic S, **Brunel N**, **Hakim V**. How Connectivity, Background Activity, and Synaptic Properties Shape the Cross-Correlation between Spike Trains. *Journal of Neuroscience* 29: 10234–10253, 2009.

Panzeri S, Schultz S, Treves A, Rolls E. Correlations and the encoding of information in the nervous system. *Proceedings of the Royal Society B: Biological Sciences.* 266:1001, 1999

Panzeri S, **Pola G**, **Petersen RS**. Coding of Sensory Signals by Neuronal Populations: The Role of Correlated Activity. *The Neuroscientist* 9: 175–180, 2003.

Pasik P, Pasik T. translation of Texture of the Nervous System of Man and Vertebrates by Santiago Ramon y Cajal; Springer-Verlan, Austria, 2002

Peichl L, **Wässle H**. Size, scatter and coverage of ganglion cell receptive field centres in the cat retina. *J Physiol* 291:117–141, 1979.

Penfield W and Jasper H. Epilepsy and the Functional Anatomy of the Human Brain. Little, Brown & Company, Boston MA, 1954

Perge JA, **Koch K**, **Miller R**, **Sterling P**. How the optic nerve allocates space, energy capacity, and information. *Journal of Neuroscience* 29(24):7917-28, 2009.

Perkel DH, **Gerstein GL**, **Moore GP**. Neuronal spike trains and stochastic point processes II: Simultaneous spike trains. *Biophysical Journal* 7: 419–440, 1967a.

Perkel DH, **Gerstein GL**, **Moore GP**. Neuronal spike trains and stochastic point processes I: The single spike train. *Biophysical Journal* 7: 391–418, 1967b.

Person AL, **Raman IM**. Synchrony and neural coding in cerebellar circuits. *Front. Neural Circuits* 6: 97, 2012.

Pillow JW, Shlens J, Paninski L, Sher A, Litke AM, Chichilnisky EJ, Simoncelli EP. Spatio-temporal correlations and visual signalling in a complete neuronal population. *Nature*. 454:995–999, 2008.

Piscopo DM, **El-Danaf RN**, **Huberman AD**, **Niell CM**. Diverse visual features encoded in mouse lateral geniculate nucleus. *Journal of Neuroscience* 33: 4642–4656, 2013.

Polack P-O, **Friedman J**, **Golshani P**. Cellular mechanisms of brain state-dependent gain modulation in visual cortex. *Nature Neuroscience* 16: 1331–1339, 2013.

Pouget A, **Deneve S**, **Latham PE**. Reading population codes: a neural implementation of ideal

observers. *Nature Neuroscience* 2: 740–745, 1999.

Pouget A, Dayan P, Zemel RS. Inference and computation with population codes. *Annu Rev Neurosci.* 26:381–410, 2003

Priebe NJ, **Ferster D**. Mechanisms of neuronal computation in mammalian visual cortex. *Neuron* 75: 194–208, 2012.

Prusky GT, **Douglas RM**. Characterization of mouse cortical spatial vision. *Vision Research* 44: 3411–3418, 2004.

Prusky GT, **West PWR**, **Douglas RM**. Behavioral assessment of visual acuity in mice and rats. *Vision Research* 40: 2201–2209, 2000.

Przybyszewski AW, Gaska JP, Foote W, Pollen DA. Striate cortex increases contrast gain of macaque LGN neurons. *Vis. Neurosci.* 17(4):485-94, 2000

Quian Quiroga R, Panzeri S. Extracting information from neuronal populations: information theory and decoding approaches. *Nature Reviews Neuroscience* 10(3):173-85, 2009.

Rall W. Theory of Physiological Properties of Dendrites. *Annals of the New York Academy of Sciences* 96: 1071–1092, 1962.

Ramon y Cajal, S. Handbook of general Anatomical pathology. 1st edition, 1890

Ratliff F, **Hartline HK**. The Responses of Limulus optic nerve fibers to patters of illumination on the receptor mosaic. *J Gen Physiol* 42: 1241–1255, 1959.

Reese BE, **Cowey A**. Fibre organization of the monkey's optic tract: I. Segregation of functionally distinct optic axons. *J. Comp. Neurol.* 295: 385–400, 1990.

Reich DS, Mechler F, Victor JD. Independent and redundant information in nearby cortical neurons. *Science* 294: 2566–2568, 2001.

Reid RC, **Alonso J-M**. Specificity of monosynaptic connections from thalamus to visual cortex. *Nature* 378: 281–284, 1995.

Reinagel P, Reid RC. Precise firing events are conserved across neurons. *Journal of Neuroscience* 22(16):6837-41, 2002

Richard D, Gioanni Y, Kitsikis A, Buser P. A study of geniculate unit activity during cryogenic blockade of the primary visual cortex in the cat. *Experimental Brain Research* 22(3):235-42, 1975

Rivadulla C, **Martinez LM**, **Varela C**, **Cudeiro J**. Completing the Corticofugal Loop: A Visual Role for the Corticogeniculate Type 1 Metabotropic Glutamate Receptor. *Journal of Neuroscience* 22: 2956–2962, 2002.

Rivlin-Etzion M, **Zhou K**, **Wei W**, **Elstrott J**, **Nguyen PL**, **Ben A Barres**, **Huberman AD**, **Feller MB**. Transgenic Mice Reveal Unexpected Diversity of On-Off Direction-Selective Retinal Ganglion Cell Subtypes and Brain Structures Involved in Motion Processing. *Journal of Neuroscience* 31: 8760–8769, 2011.

Romo R, **Hernández A**, **Zainos A**, **Salinas E**. Correlated Neuronal Discharges that Increase Coding Efficiency during Perceptual Discrimination. *Neuron* 38: 649–657, 2003.

Roy SA, Alloway KD. Coincidence detection or temporal integration? What the neurons in somatosensory cortex are doing. *Journal of Neuroscience.* 21:2462–2473, 2001

Saalmann YB, Kastner S. Gain control in the visual thalamus during perception and cognition *Current Opinion in Neurobiology* 9(4):408-14, 2009.

Saini KD, **Garey PLJ**. Morphology of neurons in the lateral geniculate nucleus of the monkey. *Experimental Brain Research* 42: 235–248, 1981.

Saleem AB, **Ayaz A**, **Jeffery KJ**, **Harris KD**, **Carandini M**. Integration of visual motion and locomotion in mouse visual cortex. *Nature Neuroscience* 16(12):1864-9, 2013

Samonds JM, Allison JD, Brown HA, Bonds, AB. Cooperative synchronized assemblies enhance orientation discrimination. *PNAS.* 101:6722–6727, 2004.

Samonds JM, Allison JD, Brown HA, Bond AB. Cooperation between area 17 neuron pairs enhances fine discrimination of orientation. *Journal of Neuroscience.* 23:2416–2425, 2003.

Scharfman HE, **Lu SM**, **Guido W**, **Adams PR**, **Sherman SM**. N-methyl-D-aspartate receptors contribute to excitatory postsynaptic potentials of cat lateral geniculate neurons recorded in thalamic slices. *PNAS* 87: 4548–4552, 1990.

Schmitzer-Torbert N, **Jackson J**, **Henze D**, **Harris K**, **Redish AD**. Quantitative measures of cluster quality for use in extracellular recordings. *Neuroscience* 131: 1–11, 2005.

Schneidman E, **Berry MJ**, **Segev R**, **Bialek W**. Weak pairwise correlations imply strongly correlated network states in a neural population. *Nature* 440: 1007–1012, 2006.

Schnitzer MJ, **Meister M**. Multineuronal firing patterns in the signal from eye to brain. *Neuron.* 37(3):499-511, 2003

Scholl B, **Tan AYY**, **Corey J**, **Priebe NJ**. Emergence of Orientation Selectivity in the Mammalian Visual Pathway. *Journal of Neuroscience* 33: 10616–10624, 2013.

Scott BB, **Brody CD**, **Tank DW**. Cellular resolution functional imaging in behaving rats using voluntary head restraint. *Neuron* 80: 371–384, 2013.

Seecharan DJ, **Kulkarni AL**, **Lu L**. Genetic control of interconnected neuronal populations in the mouse primary visual system. *The Journal of Neuroscience* 23(35):11178-88, 2003.

Seriès P, Latham PE, Pouget A. Tuning curve sharpening for orientation selectivity: coding efficiency and the impact of correlations. *Nature Neuroscience.* 7:1129–1135, 2004

Shapley R, **Hochstein S**. Visual spatial summation in two classes of geniculate cells. *Nature* 256: 411–413, 1975.

Sherman SM, **Guillery RW**. Functional organization of thalamocortical relays. *J Neurophysiol* 76: 1367–1395, 1996.

Sherman SM, **Spear PD**. Organization of visual pathways in normal and visually deprived cats. *Physiological Reviews.* 62(2):738-855, 1982

Shlens J, Fleld GD, Gauthier JL, Grivich, MI, Petrusca D, Sher A, Lltke, AM, Chichilnisky, EJ. The Structure of Multi-Neuron Firing Patterns in Primate Retina. *Journal of Neuroscience* 26:

8254–8266, 2006.

Siegert S, **Cabuy E**, **Scherf BG**, **Kohler H**, **Panda S**, **Le Y-Z**, **Fehling HJ**, **Gaidatzis D**, **Stadler MB**, **Roska B**. Transcriptional code and disease map for adult retinal cell types. *Nature Neuroscience* 15: 487–495, 2012.

Sillito AM, **Jones HE**, **Gerstein GL**, **West DC**. Feature-linked synchronization of thalamic relay cell firing induced by feedback from the visual cortex. *Nature* 369: 479–482, 1994.

Sillito AM, **Jones HE**. Corticothalamic interactions in the transfer of visual information. *Philosophical Transactions of the Royal Society B: Biological Sciences* 357: 1739–1752, 2002.

SInger W. Consciousness and the binding problem. *Annals of the NY Acad. of Sciences* 929:123-46, 2001

Sireteanu R, **Hoffmann DKP**. Relative frequency and visual resolution of X- and Y-cells in the LGN of normal and monocularly deprived cats: Interlaminar differences. *Experimental Brain Research* 34: 591–603, 1979.

Smith MA, **Kohn A**. Spatial and Temporal Scales of Neuronal Correlation in Primary Visual Cortex. *Journal of Neuroscience* 28: 12591–12603, 2008.

Sohal VS, **Zhang F**, **Yizhar O**, **Deisseroth K**. Parvalbumin neurons and gamma rhythms enhance cortical circuit performance. *Nature* 459(7247):698-702, 2009)

Sohya K, **Kameyama K**, **Yanagawa Y**, **Obata K**, **Tsumoto T**. GABAergic Neurons Are Less Selective to Stimulus Orientation than Excitatory Neurons in Layer II/III of Visual Cortex, as Revealed by In Vivo Functional Ca2+ Imaging in Transgenic Mice. *Journal of Neuroscience* 27: 2145–2149, 2007.

Stanley GB, **Jin J**, **Wang Y**, **Desbordes G**, **Wang Q**, **Black MJ**, **Alonso JM**. Visual Orientation and Directional Selectivity through Thalamic Synchrony. *Journal of Neuroscience* 32: 9073–9088, 2012.

Steriade M, Timofeev I. Neuronal plasticity in thalamocortical networks during sleep and waking oscillations. *Neuron* 37(4):563-76, 2003.

Stirman JN, **Crane MM**, **Husson SJ**, **Gottschalk A**, **Lu H**. A multispectral optical illumination system with precise spatiotemporal control for the manipulation of optogenetic reagents. *Nature Protocols* 7: 207–220, 2012.

Stone C, Pinto LH. Response properties of ganglion cells in the isolated mouse retina *Visual Neuroscience* 10(1):31-9, 1993.

Sumimoto I, Ide K, Iwama, K, Arikuni T. Conduction velocity of optic nerve fibers innervating the lateral geniculate body and superior colliculus of the rat. *Experimental Neurology* 25(3):378-392.

Sun W, **Li N**, **He S**. Large   scale morphological survey of mouse retinal ganglion cells. *Journal of Comparative Neurology* 451: 115–126, 2002.

Swindale NV. Orientation tuning curves: empirical description and estimation of parameters. *Biol. Cybern.* 78: 45–56, 1998.

Temereanca S, Simons DJ. Functional topography of corticothalamic feedback enhances thalamic spatial response tuning in the somatosensory whisker/barrel system. *Neuron* 41(4):639-51, 2004.

Thomson AM, Lamy C. Functional maps of neocortical local circuitry. *Front. Neurosci.* 1: 19–42, 2007.

Thomson AM. Neocortical layer 6, a review. *Front. Neuroanat.* 4, 2010.

Tolhurst DJ, **Movshon JA**, **Dean AF**. The statistical reliability of signals in single neurons in cat and monkey visual cortex. *Vision Research* 23: 775-785, 1983.

Tootell RB, **Hamilton SL**, **Switkes E**. Functional anatomy of macaque striate cortex. IV. Contrast and magno- parvo streams. *Journal of Neuroscience* 8: 1594–1609, 1988.

Tombol T. Layer VI cells. In Cerebral Cortex, Vol. 1, Peters A., Jones E. G., editors. , eds. Plenum Press, New York, NY, pp. 479–519, 1984.

Ts'o DY, **Gilbert CD**, **Wiesel TN**. Relationships between horizontal interactions and functional architecture in cat striate cortex as revealed by cross-correlation analysis. *The Journal of Neuroscience.* 6(4):1160-70, 1986.

Tsumoto T, **Creutzfeldt OD**, **Legéndy CR**. Functional organization of the corticofugal system from visual cortex to lateral geniculate nucleus in the cat. *Experimental Brain Research* 32: 345–364, 1978.

Tucker TR, Katz LC. Spatiotemporal Patterns of Excitation and Inhibition Evoked by the Horizontal Network in Layer 2/3 of Ferret Visual Cortex. *J Neurophysiol.* 89:488-500, 2003

Van Hooser SD, Heimel JA, Chung S, Nelson SB. Lack of Patchy Horizontal Connectivity in Primary Visual Cortex of a Mammal without Orientation Maps. *Journal of Neuroscience.* 26:7680–7692, 2006

Van Hooser SD. Similarity and Diversity in Visual Cortex: Is There a Unifying Theory of Cortical Computation? *The Neuroscientist* 13: 639–656, 2007.

Vastola EF. Steady-state effects of visual cortex on geniculate cells. *Vision Research* 7: 599, 1967.

Vinje WE, Gallant JL. Sparse coding and decorrelation in primary visual cortex during natural vision. *Science.* 287:1273–1276, 2000.

Völgyi B, **Chheda S**, **Bloomfield SA**. Tracer coupling patterns of the ganglion cell subtypes in the mouse retina. *Journal of Comparative Neurology* 512: 664–687, 2009.

Wall NR, **Wickersham IR**, **Cetin A**, **La Parra De M**, **Callaway EM**. Monosynaptic circuit tracing in vivo through Cre-dependent targeting and complementation of modified rabies virus. *PNAS* 107: 21848–21853, 2010.

Wallace DJ, **Greenberg DS**, **Sawinski J**, **Rulla S**, **Notaro G**, **Kerr JND**. Rats maintain an overhead binocular field at the expense of constant fusion. *Nature* 498: 65–69, 2013.

Wang HP, **Spencer D**, **Fellous JM**, **Sejnowski TJ**. Synchrony of Thalamocortical Inputs Maximizes Cortical Reliability. *Science* 328: 106–109, 2010.

Watanabe M, **Rodieck RW**. Parasol and midget ganglion cells of the primate retina. *J. Comp. Neurol.* 289: 434–454, 1989.

Wässle H. Parallel processing in the mammalian retina. *Nat Rev Neurosci* 5: 747–757, 2004.

Widen L, Ajmone Marsan C. Effects of corticipetal and corticifugal impulses upon single elements of the dorsolateral geniculate nucleus. *Exp Neurol.* 2:468-502, 1960

Wijesinghe R, **Solomon SG**, **Camp AJ**. Noise normalizes firing output of mouse lateral geniculate nucleus neurons. *PLoS ONE* 8: e57961, 2013.

Worgotter F, Nelle E, LI B, Funke K. The influence of corticofugal feedback on the temporal structure of visual responses of cat thalamic relay cells. *J Physiol*. 509(3):797-815, 1998

Xu X, **Ichida JM**, **Allison JD**, **Boyd JD**, **Bonds AB**, **Casagrande VA**. A comparison of koniocellular, magnocellular and parvocellular receptive field properties in the lateral geniculate nucleus of the owl monkey (Aotus trivirgatus). *J Physiol* 531: 203–218, 2001.

Yoshimura Y, Danttzker JL, Callaway EM. Excitatory cortical neurons form fine-scale functional networks. *Nature* 433(7028):868-73, 2005

Yoshimura Y, **Callaway EM**. Fine-scale specificity of cortical networks depends on inhibitory cell type and connectivity. *Nature Neuroscience* 8: 1552–1559, 2005.

Yuste R. Electrical Compartmentalization in Dendritic Spines. *Annual Rev Neurosci.* 429–449, 2013.

Zariwala HA, Madisen L, Ahrens KF, Bernard A, Lein ES, Jones AR, Zeng H. Visual Tuning Properties of Genetically Identified Layer 2/3 Neuronal Types in the Primary Visual Cortex of Cre-Transgenic Mice. *Front. Syst. Neurosci.* 4: 162, 2010.

Zarrinpar A, Callaway EM. Local Connections to Specific Types of Layer 6 Neurons in the Rat Visual Cortex. *J Neurophysiol* 95: 1751–1761, 2006.

Zhang ZW, Deschenes M. Intracortical axonal projections of lamina VI cells of the primary somatosensory cortex in the rat: a single-cell labeling study. *Journal of Neuroscience* 17(16):6365-79, 1997.

Zhao Y, **Araki S**, **Wu J**, **Teramoto T**, **Chang Y-F**, **Nakano M**, **Abdelfattah AS**, **Fujiwara M**, **Ishihara T**, **Nagai T**, **Campbell RE**. An expanded palette of genetically encoded Ca²☐ indicators. *Science* 333: 1888–1891, 2011.

Zohary E, **Shadlen MN**, **Newsome WT**. Correlated neuronal discharge rate and its implications for psychophysical performance. *Nature* 370: 140–143, 1994.